# THERMAL CONDUCTIVITY ENHANCMENT OF SOLID EICOSANE-BASED SILVER NANOSTRUCTURE-ENHANCED PHASE CHANGE MATERIALS FOR THERMAL ENERGY STORAGE

by

Rabih M. Al Ghossein

A thesis submitted to the Graduate Faculty of
Auburn University
in partial fulfillment of the
requirements for the Degree of
Master of Science in Mechanical Engineering

Auburn, Alabama
August 1, 2015

Keywords: Eicosane, Latent Heat, Phase Change Materials, Silver Nanoparticles, Thermal
Conductivity Measurement, Transient Plane Source Method

Approved by

Jay M. Khodadadi, Chair, Alumni Professor, Department of Mechanical Engineering
Roy W. Knight, Assistant Professor, Department of Mechanical Engineering
Minseo Park, Professor, Department of Physics

Abstract

In this thesis, thermal conductivity of eicosane-based PCM was enhanced by suspending highly-conductive silver nanoparticles resulting in the formation of nanoparticle-enhanced PCM (NePCM). Eicosane ($C_{20}H_{42}$) was selected as the base PCM, while Silver (Ag) was chosen as the additive. Three batches of solid eicosane-silver samples with distinct mass fractions (0, 1, 2, 3.5, 5, 6.5, 8 and 10 wt%) of nanoparticles were obtained under three different solidification routes: ice-water bath, room temperature and oven solidification. The transient plane source technique (TPS) was used to measure thermal conductivity at different temperatures starting at 10 °C and ending close to the melting point of each sample. Results showed an increase in the value of thermal conductivity as the temperature increased, and when close to melting point, a sharp rise in thermal conductivity was observed. Also, the oven solidification route samples exhibited the highest values while the ice-water samples showed the least increase. Furthermore, after a 2 wt% loading of Ag nanoparticles, a non-monotonic relationship was obtained between thermal conductivity and the weight fraction of Ag nanoparticles, regardless of the method of solidification. In addition to thermal conductivity measurement, the latent heat of fusion of the sample was investigated, utilizing differential scanning calorimetry (DSC). Results showed a decrease in the latent heat and the melting point of the NePCM as the additives loading increased due to the decrease in the number of molecules of eicosane in the samples.

## Acknowledgments

I would like to thank my major advisor, Dr. Jay M. Khodadadi, for his support, his guidance and astute knowledge on NePCM for the last two years leading to this day. I would also like to thank former and current research members of the Fluid Mechanics Research Laboratory (FMRL), Rouzbeh Rastgar, Dr. Yousef El-Hasadi and Yi Zeng, for their valuable aids when needed, and for creating a family-like environment in the office and the laboratory. I am also gratefully thankful to my family for their long-standing support, patience and encouragement during the past two years.

Thanks are also due to Dr. German (Jimmy) Mills of the Department of Chemistry at Auburn University and his PhD student, Sharif Hossain, for supervising the preparation of the NePCM samples, for guiding and helping to perform the DSC measurements and for granting access to their laboratory facilities during the research period.

I also acknowledge the Alabama Experimental Program to Stimulate Competitive Research (EPSCoR) for their support of an ACHE Graduate Research Scholars Program (GRSP) fellowship during the 2014-2015 academic year. In addition to that, I acknowledge the Department of Mechanical Engineering and the Samuel Ginn College of Engineering at Auburn University for support of my College of Engineering Graduate Fellowship during the 2013-2014 academic year.

The material in this thesis is based upon work supported by the US Department of Energy under Award Number DE-SC0002470. This report was prepared as an account of work sponsored by an agency of the United States Government. Neither the United States Government

nor any agency thereof, nor any of their employees, makes any warranty, express or implied, or assumes any legal liability or responsibility for the accuracy, completeness, or usefulness of any information, apparatus, product, or process disclosed, or represents that its use would not infringe privately owned rights. References herein to any specific commercial product, processor service by trade name, trademark, manufacturer, or otherwise do not necessarily constitute or imply its endorsement, recommendation, or favoring by the United States Government or any agency thereof. The views and opinions of authors expressed herein do not necessarily state or reflect those of the United States Government or any agency thereof.

Table of Contents

List of Tables

List of Figures

List of Abbreviations

AAO         anodic aluminum oxide

AFM         atomic force microscopy

Ag NP       silver nanoparticles

Ag NW       silver nanowires

AgOOR       silver neodecanoate

AIBN        azobisisobutyronitrile

AS          absorption spectroscopy

CA          capric acid

CB          carbon black

CNT         carbon nanotubes

CNTA        carbon nanotubes array

CNTS        carbon nanotubes sponge

COMPASS     condensed-phase optimized molecular potential for atom simulation studies

CPV         cone-and-plate viscometer

CVD         chemical vapor deposition

DAS         data acquisition software

DLS         dynamic light scattering

DSC         differential scanning calorimetry

ESEM        environmental scanning electron microscopy

FESEM       field-emission scanning electron microscopy

| | |
|---|---|
| F-MWNT | functionalized multi-walled nanotubes |
| FSPCM | form-stable phase change materials |
| FTIR | Fourier transform infrared spectroscopy |
| GA | graphene aerogel |
| GF | graphite flakes |
| GN | graphite nanosheets |
| GNF | graphite nanofibers |
| GnP | graphene nanoplatelets |
| HDPE | high density polyethylene |
| HFM | heat flow meter |
| HyTES | hybrid nanocomposite-based thermal energy storage |
| HNT | halloysite nanotube |
| HyNPCM | hybrid nanocomposite phase change materials |
| LA | lauric acid |
| LFA | laser flash analyzer |
| LHS | latent heat storage |
| MWCNT | multi-walled carbon nanotubes |
| NAD | nitrogen adsorption-desorption measurement |
| NEMD | non-equilibrium molecular dynamics simulation |
| NePCM | nanostructure-enhanced phase change materials |
| NF | nanofluid |
| NG | nanographite |
| NP | nanoparticles |

| | |
|---|---|
| OA | octadecanoic |
| O-GN | oriented graphite nanosheets |
| O-MWNT | oxidized multi-walled nanotubes |
| OS | oleoyl sarcosine |
| PA | palmitic acid |
| PCM | phase change materials |
| PEG | polyethylene glycol |
| PMMA | polymethyl methacrylate |
| PPM | parts-per-million |
| PPS | poly (p-phenylene sulfide) |
| PW | paraffin wax |
| R-GN | randomly distributed graphite nanosheets |
| SA | stearic acid |
| SDBS | sodium dodecyl benzene sulfonate |
| SDS | sodium dodecyl sulfate |
| SEM | scanning electron microscopy |
| SG | sulfonated graphene |
| SHS | sensible heat storage |
| SNOE PCM | silver nano-based organic ester phase change materials |
| SSAA | specific surface area analyzer |
| SS-PCM | shape-stabilized phase change materials |
| SWCNT | single-walled carbon nanotubes |
| TC | thermocouple |

| | |
|---|---|
| TCE | thermal conductivity enhancement |
| TD | tetradecanol |
| TEM | transmission electron microscopy |
| TGA | thermal gravimetric analysis |
| THW | transient hot wire method |
| TPS | transient plane source method |
| UV-vis | ultra violet-visible spectroscopy |
| XPS | X-ray photon spectroscopy |
| XRD | X-ray diffraction |

## List of Symbols

| Symbol | Quantity | SI Unit |
|--------|----------|---------|
| $C_p$ | Specific Heat of Capacity | kJ/kgK |
| $k$ | Thermal Conductivity | W/mK |
| $K_f$ | Molal Freezing-point-depression Constant | kgK/mol |
| $m$ | Molality | dimensionless |
| $n$ | Number of Moles | moles |
| $r$ | Radius of Sensor | mm |
| $R$ | Ideal Gas Constant | J/molK |
| $R_s$ | Electrical Resistance | Ω |
| $R_{th}$ | Thermal Resistance | mK/W |
| $T$ | Temperature | ºC, or K |
| **Greek Symbols** | | |
| $\alpha$ | Thermal Diffusivity | $m^2/s$ |
| $\Delta H$ | Latent Heat of Fusion | kJ/kg |

| | | |
|---|---|---|
| $\emptyset_{vol}$ | Volume Fraction | dimensionless |
| $\emptyset_{wt}$ | Mass Fraction | dimensionless |
| $\rho$ | Density | kg/m$^3$ |
| $\sigma$ | Electrical Conductivity | S/m |
| $\beta$ | Coefficient of Thermal Expansion | 1/K |

**Subscripts**

| | |
|---|---|
| $c$ | Continuous Phase |
| $d$ | Discrete Phase |
| $eff$ | Effective |
| $f$ | Freezing |
| $m$ | Melting |
| $vol$ | Volume |
| $wt$ | Weight |

**Superscripts**

| | |
|---|---|
| $o$ | Pure Sample |

Chapter 1 Introduction

## 1.1 <u>Background and Objectives</u>

Due to the ongoing growth of economies and greater industrial productivity, more ways to produce energy are needed in order to meet the ever-increasing demand. Fossil fuels have long been the primary source of energy, but due to the hazardous consequences on the environment and the ever-increasing and unstable price of fossil fuels, greater emphasis has been focused on a wider utilization of renewable sources of energy. According to the U.S. Energy Information Administration (2015), the amount of energy consumed in the U.S. in 2014 was about 98.3 quadrillion ($10^{15}$) Btu (British thermal unit), of which only 10% originated from renewable energy sources (Figure 1.1). However, resurgence of investments in renewable sources of energy has seen an increase of 17% to $270 billion in 2014, due to the international effort of many regions and countries, led by China (which accounted for investments worth $83.3 billion). In second place comes the U.S., with $38.3 billion, an increase of 7% from the previous year, then Japan, India and Brazil (Frankfurt School – United Nations Environment Programme Collaborating Centre for Climate & Sustainable Energy Finance, 2015). Solar, wave and wind energies are the most common forms of renewable sources of energy, and are known to be clean and sustainable. However, availability of these energy sources is deemed unreliable on many

occasions. In effect, the major bottleneck associated with greater implementation of renewable sources of energy has been the issue of its availability during the peak demand periods.

Among the different forms of energy, thermal energy is widely encountered as solar irradiance, geothermal energy, waste heat and thermally stratified layers in oceans (Fan and Khodadadi, 2011). Waste heat from fuel combustion processes could be captured, but its availability is unpredictable and would entail a change of the industry infrastructures. As for the solar irradiance, it is dependent on the latitude and the local incident solar radiation, whereas low-grade geothermal resources could be utilized to deliver energy needs at temperatures below 120 $^{o}$C (Fox et al., 2011). In order to address this imbalance of demand and supply, effective technologies such as thermal energy storage (TES) play a major role in storing thermal energy for use at a future time (Rathod and Banerjee, 2013). Subsequently, stored thermal energy can be used for providing thermal comfort in work environment, promoting energy conservation and improving operational life of electronics among others (Khodadadi et al., 2013). Thermal energy can be stored primarily as sensible heat storage (SHS) or latent heat storage (LHS) and chemically using chemical heat storage (CHS) methods. SHS utilizes the specific heat capacity of the storage material to increase the temperature of the substance during *charging*, whereas LHS relies on absorption of heat at a constant temperature during phase change. Both systems require insulation in order to reduce heat losses to the ambient air (Gur et al., 2012). The thermo-chemical storage systems are based on the energy captivated/emitted during a breaking/reforming of molecular bonds in a reversible chemical reaction change. LHS and CHS systems are categorized as *thermophysical* modes, while CHS is referred to as the *thermochemical* mode of thermal energy storage. An important factor in deciding on the best storage method resides in the energy densities of the thermophysical and thermochemical

approaches, as illustrated in Figure 1.2. Thermophysical storage possess high volumetric energy density but low gravimetric energy density, while thermochemical systems can afford light weights because of their one-gas phase component, but they require a large volume due to the lack of mechanical compression (Gur et al., 2012). Regardless of the mode of thermal energy storage, in order to extract the absorbed energy in the storage material, a reverse process must take place (*discharging*).

In this thesis, focus is placed on the storage of thermal energy as latent heat which takes place by changing the phase of the material at a nearly constant temperature. Such energy storage materials are called Phase Change Materials (PCM) that includes both organic and inorganic substances. In choosing the best candidate for latent heat storage, several steps and criteria need to be considered for the development of a TES system. An overview of the different stages in the design of a *low-temperature* (0-120 $^{o}$C) TES is presented in Figure 1.3, which was reproduced from Abhat (1983). In his study, Abhat (1983) advised on the use of latent heat storage methods among the different energy storage techniques, and the use of paraffins, as phase change materials, for low-temperature range systems. The following thermophysical properties such as high latent heat of fusion, low melting temperature, no supercooling during phase change, and good stability when subjected to multiple cycles of charging and discharging make paraffin wax very desirable for many applications. Among a variety of PCM (fatty acids, salt hydrates, alcohols, etc…), as discussed by Pielichowska and Pielichowski (2014), paraffin waxes have been the most commonly-used organic PCM and its areas of application include, and not limited to: paper industry, household chemicals (polishes, creams, candles, etc.), cosmetics (perfumes, beauty masks, protective creams, etc.), food industry and agriculture (cheese-coating, poultry processing, fruit preservation, etc.) (Freund et al., 1982). However, paraffin waxes, with a

chemical formula of $C_nH_{2n+2}$, possess one unwelcomed property: a low thermal conductivity, thus limiting the rates at which energy can be added to and extracted from the material. As a consequence, attempts to increase this thermophysical property have been the major focus of many researchers over the years by insertion of fixed, non-moving structures such as metal fins and foams (Fan, 2011) or by the suspension of various types of highly conductive nanostructures (Nabil and Khodadadi, 2013). Colloidal suspensions of nanoparticles can also be used to improve the thermophysical properties of the PCM, such as supercooling, specific heat, etc. Focusing on improving thermal conductivity of PCM through dispersion of nanostructures, this novel approach only started a few years ago. Back in 2007, Khodadadi and Hosseinizadeh (2007) reported results of a computational model showing the improvement of the functionality of the PCM through dispersion of nanoparticles. The model nanoparticle-enhanced phase change materials (NePCM) exhibited reduction in its freezing period in comparison to the base material. Since then, many researchers have followed in their footsteps, and an abundance of journal papers were published on NePCM and their applicability for thermal management, waste heat recovery, etc. In this thesis, a review of some of those papers is discussed with great attention to the type of nanoparticles used (metallic, carbon-based, metal oxide…) and the observed thermal conductivity enhancement.

In this project, the objectives were the preparation of the NePCM samples with colloidal suspensions of metallic silver (Ag) nanoparticles (0, 1, 2, 3.5, 5, 6.5, 8 and 10 wt%) in eicosane ($C_{20}H_{42}$) following three different solidification schemes: ice-water bath, room temperature and oven solidification approaches. Also, determination of the composites' thermal properties such as thermal conductivity, latent heat and melting point using the transient plane source technique and differential scanning calorimetry was of interest. And finally, the dependence of thermal

conductivity of the NePCM on the loading of Ag nanoparticles, the samples' temperature and the specific method of freezing were all investigated and discussed.

## 1.2 <u>Outline of the Thesis</u>

This thesis consists of four chapters as follows: introduction, literature review, experimental studies of eicosane/silver nanoparticle colloids, and conclusions. As discussed above, the motivation and goals behind the present study were discussed in Chapter 1. Chapter 2 offers a chronologic literature survey of 30 review papers, published in the period of mid-2011 to the year 2013, on the subject of NePCM with focus on thermal conductivity enhancement of phase change materials for thermal energy storage. In Chapter 3, the preparation and characterization of the solid Ag/Eicosane samples is discussed. Then, a set of experimental tests were conducted on the NePCM samples for a different range of temperature in order to evaluate its thermal properties such as thermal conductivity. Finally, in Chapter 4, a summary of the findings and recommendations for future studies is outlined.

## U.S. energy consumption by energy source, 2014

Total = 98.3 quadrillion Btu

Total = 9.6 quadrillion Btu

- Petroleum 35%
- Natural gas 28%
- Coal 18%
- Nuclear electric power 8%
- Renewable energy 10%

- Solar 4%
- Geothermal 2%
- Wind 18%
- Biomass waste 5%
- Biofuels 22%
- Wood 23%
- Hydroelectric 26%

Biomass 50%
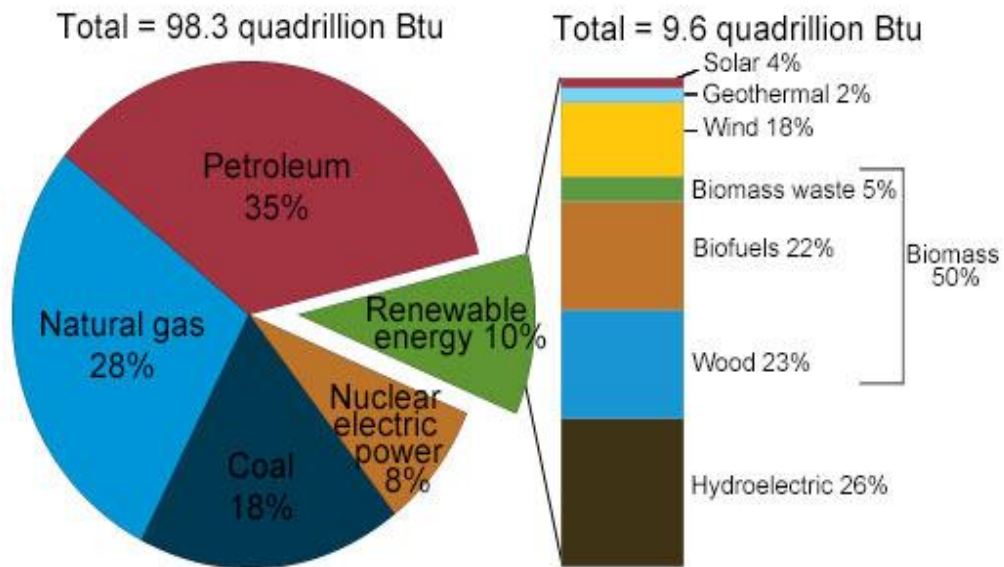
Note: Sum of components may not equal 100% as a result of independent rounding.

Source: U.S. Energy Information Administration, *Monthly Energy Review*, Table 1.3 and 10.1 (March 2015), preliminary data

eia

Figure 1.1    A diagram illustrating the United States energy consumption by energy source for the year 2014 (U.S. Energy Information Administration, 2015); A quadrillion is equal to $10^{15}$.
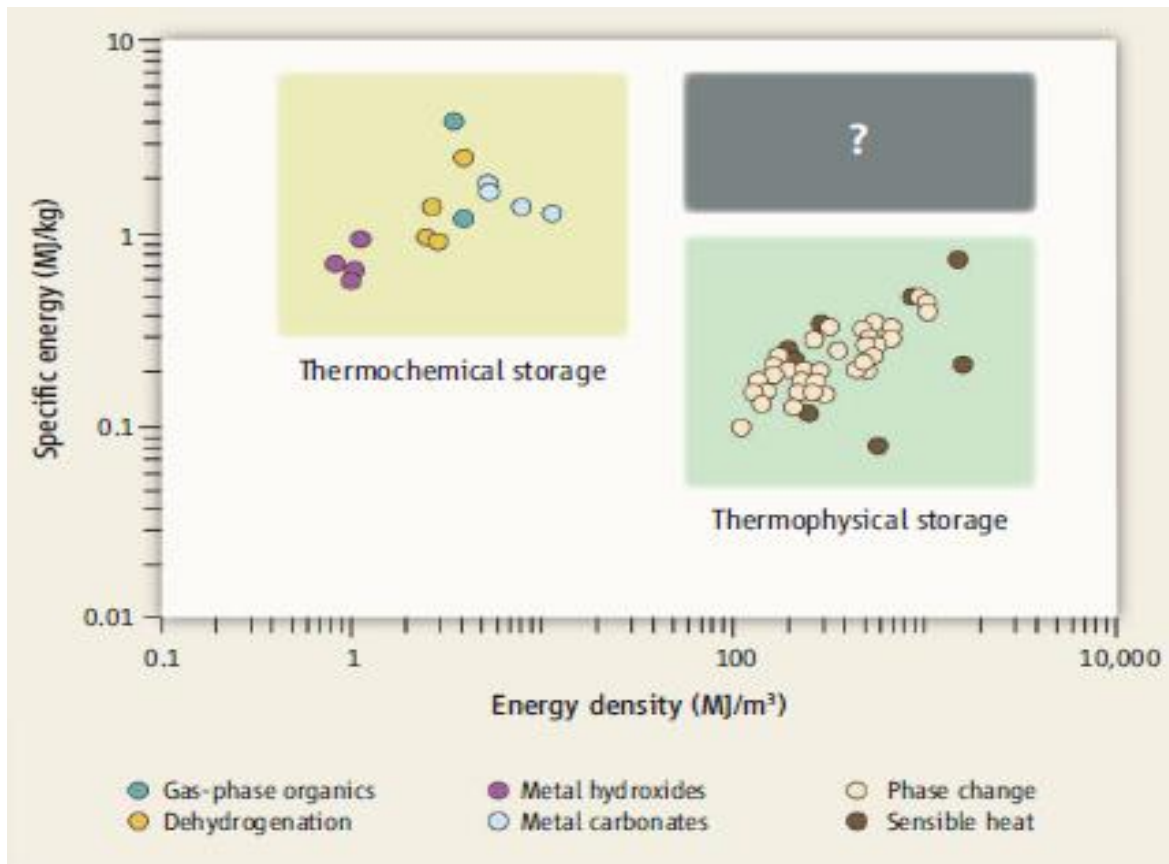
Figure 1.2　　　Volumetric and gravimetric energy densities for thermophysical and thermochemical storage systems (Gur et al., 2012)
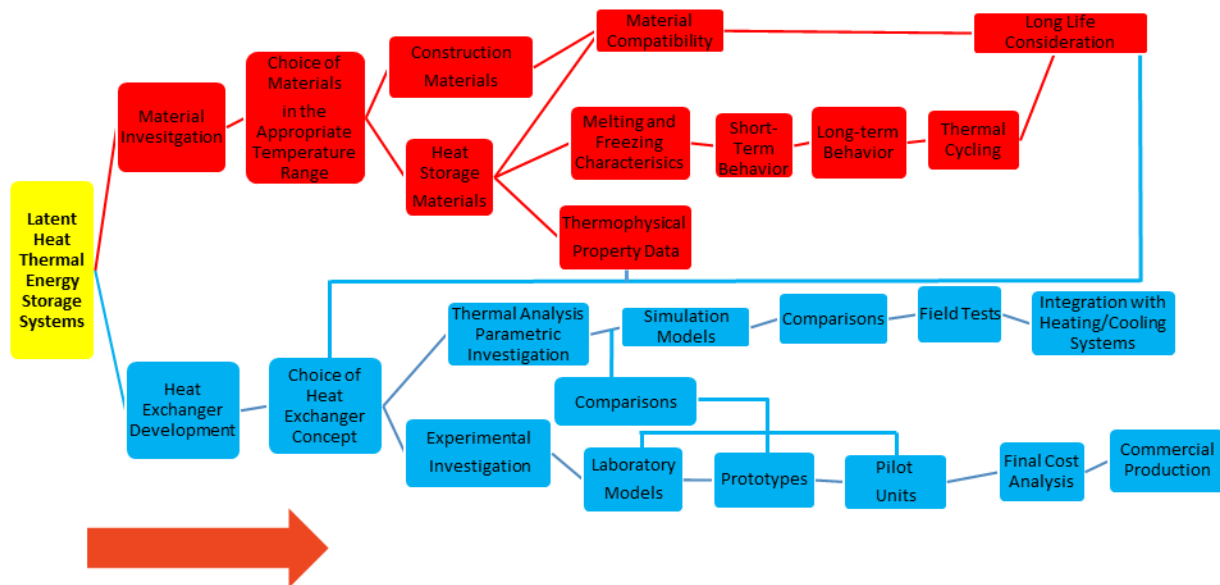
Figure 1.3    A diagram of progressive steps to follow in the development of a low-temperature

(0 – 120 $^{\circ}$C) latent heat storage unit (reproduced from Abhat, 1983)

Chapter 2 Literature Review

This chapter is devoted to reviewing chronologically the relevant NePCM journal papers published from the year 2011 to the year 2013. The 20+ papers reviewed in this chapter were generally concerned with investigations of the thermal properties, thermal behavior and heat transfer of phase change materials (PCM) suspended with nanostructures for thermal energy storage. Special attention was placed on review of studies that focused on the enhancement of thermal conductivity of the composites and its dependence on temperature, phase (liquid or solid), loading of nanoparticles, etc.

## 2.1 Introduction

Prior to 2007, researchers' methodology on improving thermal conductivity in phase change materials was based upon the inclusion of fixed, stationary highly-conductive inserts/structures into PCM such as metallic fins, wool, brush and honeycomb. Copper, carbon fiber and aluminum were some of the materials used as thermal conductivity enhancers. A review of the work associated with the use of fixed structures was presented by Fan and Khodadadi (2011).

Starting in 2007, a transition from stationary inserts to colloidal nanostructures was initiated with publication of many studies on suspending nano-additives in phase change materials. In that year, Khodadadi and Hosseinizadeh (2007) prepared a computational model reporting the improvement of the functionality of the PCM through dispersion of nanoparticles. The model nanoparticle-enhanced phase change materials (NePCM) exhibited enhancement of the freezing process due to improved thermal conductivity of the NePCM in comparison to the base material. This work served as the foundation to this novel form of thermal conductivity enhancement, and since then, more than 130 papers have been published about the preparation and characterization of the various combinations of base PCM and nano-structured additives. Figure 2.1 illustrates the number of papers published on pure phase change materials and the rise of published studies on nano-structured/phase change materials since 2007.

Paraffins have served as the most widely-used choice for the base PCM. As for the nanostructure thermal conductivity promoters, the choices were numerous such as carbon-based nanostructures (nanofibers, nanoplates, nanotubes and graphene flakes), metallic (Ti, Al, and Cu) and metal oxide ($Al_2O_3$, CuO, and $ZrO_2$) nanoparticles, and metallic nanowires (Ag and Cu). Most studies focused on the dependence of thermal conductivity on the particles' loading and different temperature ranges in both liquid and/or solid phases. Furthermore, some studies expanded their research to investigate other thermophysical properties of the NePCM such as the melting point, latent heat of fusion, viscosity, specific heat, supercooling, etc. Among all aforementioned types of nanofillers and up to this day, carbon-based nanostructures proved to generate the highest enhancement of thermal conductivity. A review of the work associated with this novel form of promoting thermal conductivity was presented by Khodadadi, Fan and Babaei (2013) focusing on the papers published in the period from 2007 to mid-2011, with attention to

thermal conductivity enhancement and the different forms of nano-additives. Also, in a recent thesis, Nabil (2013) reviewed an additional 27 journal papers concentrating on thermal conductivity improvement as a function of loadings of additives and types of nano-enhancers.

The present work is a continuation of review studies on NePCM from the period of mid-2011 to present day and taking into consideration also the papers that were missed by Khodadadi et al. (2013) and Nabil (2013). Tables 2.1 and 2.2 present a summary of the published papers starting with the previously-missed papers and moving chronologically according to the *date of submission* for publication. To elaborate on each table, properties of both the phase change materials and the nanostructure additives, dimensions of the nanofillers and their loadings are provided in Table 2.1. Summaries of the preparation methods of the NePCM composites, their characterization in relation to the instruments and measurements used in determining the thermal conductivity and other thermal properties, and finally any stability issues mentioned by the authors are given in Table 2.2.

## 2.2 Review of the Recent Journal Papers on NePCM

As mentioned above, an extension to the NePCM journal papers reviewed in Khodadadi et al. (2013) and Nabil (2013) are documented and discussed *chronologically* in this chapter. All figures, except for Figure 2.1, in this manuscript are extracted from the reviewed papers.

Possessing high latent heat of fusion, phase change materials provide an ideal choice for their use in cyclic operations. However, their low thermal conductivity hinders its effectiveness

11

in larger containers and therefore led Sanusi, Fleischer and Weinstein (2010) to examine the thermal behavior of PCM with the addition of carbon nanofibers during solidification. Blended paraffin, with a melting temperature range of 54-58 ℃ and a mass range of 100 g to 2.8 kg, was chosen as the base PCM, while graphite nanofibers (GNF) with a diameter range of 2-100 nm were selected as the thermal conductivity enhancers. Four module designs (2 cubes and 2 rectangles) of different dimensions were fabricated to investigate the effects of the aspect-ratio and volume of the container on the thermal response of the system. The batch was prepared by blending GNF and PCM using a SONICS VC505 Ultrasonic Processor up to 4 wt% GNF, after which manual mixing is required to achieve the 10 wt% GNF/PCM. The experimental setup is shown in Figure 2.2. Temperatures were recorded at all 5 thermocouple locations, as well as at the heater base and within the cold plate. Results showed that the base PCM melted much quicker than the GNF/PCM blend due to low thermal conductivity which creates higher thermal resistance. Also, the GNF/PCM exhibits a lower peak temperature (120 ℃) than the base paraffin (140 ℃). As for the effect of the aspect-ratio of the test modules, data showed that the GNF/PCM blend had a much shorter solidification time than that of the base PCM in cubic containers.

Mei et al. (2011) prepared samples of various weight ratios (50:50, 55:45, 60:40, 65:35 and 100:0) of capric acid (CA) phase change material into halloysite nanotube (HNT) to from a stable phase change material composite. A 5 wt% loading of graphite was added to the CA/HNT resulting in a CA/HNT/G (60:35:5 wt%) composite in order to compare its thermal behavior to that of the CA/HNT composites. CA and graphite were purchased from Chemical Reagent Co., Ltd., Tianjin, China and Grenada Development Carbon Materials Co., Ltd., Nanjing, China, respectively, while HNT clay from Henan Province, China that was milled, sieved and over-

dried at 373 K for 24 hours was used. After preparing the CA/HNT and CA/HNT/G composites, Fourier transform infrared (FTIR) spectroscopy proved the existence of only a physical interaction between the materials, and the samples were found to be stable for 50 melting/freezing cycles with no presence of liquid leaking and no surface deformation as illustrated in Figure 2.3. To investigate the thermal properties and thermal conductivity of the composites, Differential Scanning Calorimetry (DSC) and a thermal property analyzer (TC 300, Xiatech Electronic Technology Co., Ltd.) which is an extended application of the Transient Hot Wire (THW) method were adopted by the authors, respectively. Results showed that the melting temperature and the latent heat of the CA/HNT composites differed slightly from that of the CA/HNT/G composite in both freezing and melting cycles. However, thermal conductivity was greatly enhanced with the addition of the 5 wt% graphite; the thermal conductivity of the CA/HNT composite was measured at 0.479 W/mK in the solid state compared to that of the CA/HNT/G composite, an increase of 58%. Furthermore, the cooling and melting times of the graphite composite (250 and 130 s) were shorter than that of the graphite-free composite (700 and 350 s) that correspond to a thermal storage and release rate improvement of 180% and 170%, respectively.

Chintakrinda et al. (2011) investigated the thermal behavior and energy storage of paraffin-based PCM through the use of three types of thermal conductivity enhancements (TCE). Due to its relatively high phase change temperature of 54 °C and its compatibility with a variety of enhancers, an organic paraffin wax, IGI 1230A, purchased from the International Group Inc. was selected as the base PCM. The three material enhancers were the following: (a) 10 wt% graphite nanofibers (GNF) with a diameter range of 50-100 nm and fiber lengths of approximately 100 μm, (b) 40 PPI (pores per inch) 8-10% relative density Duocel 6061 T6

aluminum foam matrix purchased from ERG Aerospace, and (c) an open pore graphite foam matrix (POCO-HTC). The aluminum foam matrix has an effective thermal conductivity of 5 W/mK, much lower than the 245 W/mK value of the graphite foam matrix, but still greater than the thermal conductivity of bulk paraffin. Also, GNF possesses a very high thermal conductivity, thus explaining the choices of all three thermal conductivity enhancers. The cubic test modules, tightly sealed to contain the PCM in the liquid phase, were fabricated from four aluminum plate sidewalls with side length of 5.08 cm and a volume of 131 cm$^3$. After preheating the foam module to 40 °C to stop solidification of the paraffin upon contact, the PCM was poured into the hot foam at a slow rate. Filling the aluminum foam was easier than that of the graphene foam due to its larger pore size; therefore, great care was taken into filling the graphene foam. Then, the modules were solidified and mounted to a heated base. Five type-T thermocouples were located at different locations to measure the transient heating of the test modules and to compare the thermal response of the PCM composites due to the addition of the different thermal conductivity enhancement agents. Comparison of the three configurations was performed in both solid and liquid phases for a range of power loads of 50 to 500 W. Results showed that for a slow heating rate (50 W), the GNF/PCM provided the greatest extension of the transient heat-up time and the lowest base temperature after a time duration of 30 min. After another 30 min, the PCM/graphite module exhibited the lowest base temperature. Also, both modules at that time instant (60 min) showed no melting of the PCM. On the other hand, more than half of the PCM/aluminum foam was melted and conduction was dominating. As for the base paraffin, less than half of the mass had melted with the Rayleigh-Bernard convection currents being dominant in the melting region, and a superheated liquid layer at the base consistently present. Upon increasing the power, all four test modules experienced melting. The GNF/PCM specimen took the longest time to

completely liquefy (36 min) and exhibited better temperature stratification from source to sink compared to the rest of the modules, but had the lowest thermal control of the heated base among all modules. As for the foams, the PCM/graphite was the quickest to melt (5 min), 3 minutes less than melting time of the PCM/aluminum. In addition to that, the PCM/graphite foam was the only system to reach the steady-state condition, and provided the lowest base temperature and heating rate among all modules. The heat sink characteristics of the foams were improved while maintaining the rapid melting of the PCM, without occurrence of a major delay to reach the steady-state condition.

Ehid and Fleischer (2012) developed samples of various weight ratios (100/0, 90/10, 80/20, 70/30, 60/40, 50/50 and 0/100) of paraffin (type IGI-1230A, supplied by the International Group Inc.) to high-density polyethylene (HDPE, bought from Sigma-Aldrich) in order to assess the thermal and structural properties of the shape-stabilized phase change materials (SS-PCM). Due to the direct dependence of the energy storage capacity of a phase change material on the amount of paraffin, it is best to have as little polymer additive as possible. Therefore, the experimental study was done to detect the effects of different concentrations of the polymer and to determine at what point the material becomes shape-stabilized. To prepare the sample, the paraffin was melted over a hot plate, followed by an even distribution of liquid HDPE. The mixture was stirred for 30-60 min at 180-200 $^{o}$C using a magnetic stirrer, then poured into a mold for solidification. One criterion of shape stabilization is the elimination of the ullage formation during solidification, and results showed that for a loading of 40 wt% HDPE or more, no volume contraction took place during phase change. However, with rapid cooling rates, the samples reverted to the formation of ullage. A second criteria of shape stabilization is the preservation of the physical structure of the samples; impact testing performed at ambient level

showed an increase in hardness as the weight percentage of HDPE increased. However, at an elevated temperature, the materials showed no strength with the highest hardness, 48, exhibited by the 50/50 sample, 37% and 50% less than the 100% paraffin and the 50/50 sample at ambient temperature, respectively. Differential Scanning Calorimetry (DSC) tests showed a decrease in the latent heat as the HDPE portion was increased, while the melting temperature of the samples was unaffected due to insignificant chemical interaction between paraffin and HDPE. However, the polymer's phase change temperature does decrease as the amount of the polymer is increased. In an effort to quantify the thermal cycles of the SS-PCM, the heating and cooling curves were investigated across a cubical aluminum module with inner dimensions of 5.08 × 5.08 × 5.08 cm$^3$ or 10.16 ×10.16 × 10.16 cm$^3$ and walls 32 mm thick for different power settings. For the same applied power of 100 W, results showed that for a 90/10 sample the hot PCM is rising along the left heated wall of the module, moving across the module, and upon cooling down it sinks along the right cooled side of the module, indicating that natural convection is present in the module. In effect, the liquid paraffin, being below the melting point of the HDPE, is mixing within the solid HDPE matrix through convection. As a result, the 90/10 sample is not shape-stabilized. Same results were reported for the 80/20 sample, with a small temperature difference still being observed (Figure 2.4). However, for a material with 30% HDPE, no temperature gradient existed, and the sample was considered to be shape-stabilized (Figure 2.5). As for the increase in applied power (50 to 500 W), higher maximum temperatures, shorter heating and longer cooling cycles occurred for all samples. For this study, samples with HDPE above 25-30% showed to be the optimal samples due to their structural strength, elimination of volume contraction during solidification and good circulation of paraffin above melting temperature.

Ehid et al. (2012) tested the extent of graphite nanofiber (GNF) settling during the phase change process of a shape stabilized phase change material (SS-PCM) by preparing a sample of 5 wt% of GNF in paraffin. The paraffin, having a melting temperature of 54 $^o$C, was a type IGA-1230A purchased the International Group Inc., whereas the GNF were developed in-house and its dimensions ranged from 2 to 1000 nm in diameter and up to 100 μm in length. High-density polyethylene (HDPE), acquired from Sigma-Aldrich, was used as the shape stabilizer agent for the SS-PCM. In preparation of the SS-PCM/GNF sample, various concentrations of HDPE (10% to 50% in weight) were added to create the aforementioned samples. The materials were blended using sonication for a time duration of four to six hours, after which the blend was poured into the cube-shaped aluminum test module and allowed to solidify. Five type-T thermocouples were inserted in the module to record the transient temperature response of the samples, and one type-T thermocouple was attached to the bottom of the module to measure the base temperature. The module was placed on a heater block, and the complete representation of the setup is shown in Figure 2.6. Data acquisition was stopped once the system reached steady-state or when the module was overheated which was the case for all tests. Results showed that, for an applied power of 50 W, the 5 wt% GNF/PCM sample displayed migration of the nanofibers in a thin clear paraffin layer resting above a black GNF/paraffin layer after one thermal cycle. Then, a second thermal cycle was performed, and collected data exhibited steeper heating curve, shorter heating time period and higher maximum temperature indicating greater isolation of the sample from the cold plate. The reason behind those effects is the settling of the GNF leaving a pure paraffin layer adjacent to the cold plate. After the second thermal cycle, no significant change in thermal behavior was observed due to the insulating layer of the pure PCM next to the cold plate and the creation of a stable fiber matrix at the bottom of the sample, but the

GNF continued to settle (Figure 2.7). For the SS-PCM/GNF sample with 30 wt% HDPE, the thermal behavior exhibited steeper heating curve and higher maximum temperature due to the reduction of the latent heat for the first thermal cycle, but the sample didn't display separation of nanofibers as seen with the PCM/GNF (Figure 2.8). The test was also repeated for twenty cycles, and no significant change in thermal response was observed proving that shape stabilization succeeded in stopping the GNF settling. Lastly, a 10 wt% HDPE sample was tested for 10 cycles, and results showed that the sample was also successful in preventing migration of the GNF, but the sample was not shape-stabilized due to the formation of ullage space at the top surface of the sample and the presence of density contraction.

Zhang et al. (2012) prepared a novel type of phase change material (PCM) by preparing a form-stable polyethylene glycol (PEG)/polymethyl methacrylate (PMMA) composite, which will be referred to as FSPCM. In order to enhance the thermal properties of the composite, various weight fraction (1, 2, 4, 6 and 8 wt%) of graphite nanoplatelets (GnP) were added to the mixture by ultrasonication using the surfactant azobisisobutyronitrile (AIBN). PEG and graphite were purchased from Sinopharm Chemical Reagent Co. Ltd. and Qingdao Tianhe Graphite Co. Ltd., respectively. The optimal mass ratio of PEG to PMMA was determined previously, by the authors to be 7:3 in order to maintain a good thermal storage density of the composites, while keeping it also stable. FESEM images of the pure FSPCM and FSPCM composites indicated that the PEG was successfully implanted inside the PMMA region, resulting in a mechanically stronger FSPCM composite; hence, the FSPCM will remain stable even after subjecting it to a temperature above the melting point of the PEG. Furthermore, FESEM showed that the GnP were dispersed uniformly in the composite leading to a better network between the materials. A Transient Planar Source system (2500S, Hot Disk) and a semiconductor characterization test

system (4200, Keithley) were used to measure the thermal and electrical conductivities of the samples, respectively. Results showed an increasing trend in thermal conductivity as the mass fraction of GnP increased due to the formation of thermal conductive networks in the FSPCM composites (Figure 2.9). A similar result was obtained for the electrical conductivity, with a significant enhancement starting to occur for a 2 wt% loading of GnP. For the highest loading (8 wt%) of the nano-enhancers, thermal and electrical conductivity were improved by 9 and 8 times than that of the pure PEG/PMMA composite, respectively. However, DSC data revealed that the addition of GnP had an inverse proportionality relation to the thermal properties of the samples; as the mass loading of GnP increased, the latent heat of melting and freezing and the melting temperature decreased, while the freezing temperature increased, as exhibited in Figures 2.10 and 2.11. The samples were also subjected to a stability test, from room temperature to 600 $^o$C, with the use of a thermogravimetric (TG, STA449c/3/G, NETZSCH) instrument at a heating rate of 10 $^o$C/min. Results indicated that the samples were degraded slightly and in two steps: 1$^{st}$ step in the range of 175-220 $^o$C, and 2$^{nd}$ step in the range 300-312 $^o$C. Moreover, as the mass loading of the GnP increased, the mass loss was reduced, an indication of the good thermal stability properties obtained with the inclusion of the graphite nanoplatelets. However, in this paper, the samples' temperature never exceeded 80 $^o$C, so the FSPCM composites were always stable.

Jia et al. (2013) investigated the melting temperature ($T_o$), phase change time ($t_{1/2}$), and enthalpy ($\Delta H$) of water-based nanofluids (NF) with the addition of different loading (0.05-1 wt%) of titanium dioxide nanoparticles (TiO$_2$ NP, purchased from Shanghai Huzheng nanotechnology Co., Ltd., China) at various cooling rates (0.5 to 9 $^o$C/min). The Malvern Zetasizer-nano device (Zetasizer Nano ZS, Malvern Instruments Ltd., England) showed that the TiO$_2$ NP had a diameter of 10-15 nm, while the average size of the particles of TiO$_2$ NF was in

19

the range of 200-300 nm. The spectrophotometer (VIS-722S, Shanghai Lvyu Precision Instrument Manufacture Inc., China) experiments showed that water-TiO$_2$ NF containing 0.15-0.7 wt% NP had good stability unlike the remaining loadings. Fifty (50) Differential Scanning Calorimetry (DSC) tests were conducted for each loading of TiO$_2$. The DSC data for $T_o$, $t_{1/2}$ and $\Delta H$ were plotted in 3 dimensions to determine the dependency of each thermal property on the following two parameters: mass concentration ($c_{TiO_2}$) and cooling rates ($\emptyset$) (Figure 2.12). Results showed that for low values of the cooling rate ($\emptyset < 5\,°C/min$), the thermal properties were more affected by the concentration of the nanoparticles, while for the range of $\emptyset >$ 5 °C/min, $T_o$, $t_{1/2}$ and $\Delta H$ were greatly influenced by the cooling rate. As $\emptyset$ increased, the melting point decreased for increasing mass concentrations of NP, and the solidification process was quicker. Also, results showed that water-TiO$_2$ NF with good stability exhibited the highest values of enthalpy and melting temperature while taking the longest time to solidify. On the other hand, the unstable water-TiO$_2$ NF were easily affected by the cooling rates, even at slower cooling rates; they exhibited the lowest phase change temperature and enthalpy, but solidified quickly.

He et al. (2012) developed a novel type of nanofluid phase change material by suspending various volume fractions (0.167, 0.283, 0.565 and 1.13 vol%) of titanium dioxide (TiO$_2$) nanoparticles (purchased from Chongqing Chemical Industry Co. Ltd., China) in barium dichloride (BaCl$_2$) solution. Several thermal properties were measured and analyzed. The thermal conductivity measurements were recorded using the transient hot wire (THW) method for a range of temperature from -5 to 25 $^o$C. Figure 2.13 shows the data recorded for the different volume fractions of TiO$_2$ nanoparticles. Results showed a nearly linear relation between the thermal conductivity and the temperature, and as the volume of titanium dioxide increased, the

thermal conductivity increased also. For the highest volume fraction of 1.13 vol% of $TiO_2$, the greatest enhancement was 16.74% at 25 $^o$C, while at a temperature of -5 $^o$C, the greatest enhancement was 12.76%. The supercooling effect of the nanofluids was also investigated using thermocouple readings during freezing/melting cycles and data acquisition software (DAS). Results showed that the volume of nanoparticles had a huge effect on the nucleating supercooling degree and the beginning of the nucleation time. For the highest loading of $TiO_2$, the supercooling degree was nearly eliminated and reduced by 84.92%, the total freezing time was reduced by 64.5%, and the nucleation time had started 1050 s before that of the pure $BaCl_2$ aqueous solution. Differential Scanning Calorimetry (DSC, made in German NETZSCH Company, DSC-200 PC Phox) was also used to measure the latent heat, phase change temperature and specific heat of the nanofluids. Results showed that the changes in the melting point and the specific heat, as the volume of nano-enhancers increased, were minimal. The highest reduction, for the 1.13 vol% suspension, was 2.84% and 12.4% for the phase change temperature and the specific heat, respectively. As for the latent heat, there was a slight decrease for the first loading (0.167 vol%), but a huge drop took place above the 0.283 vol% loading (Figure 2.14). Two explanations behind that phenomenon could be: (1) the reduction in the concentration of $BaCl_2$-$H_2O$ greatly by the $TiO_2$ nanoparticles, leading to the latent heat of the $TiO_2$-$BaCl_2$-$H_2O$ being offered completely by $BaCl_2$-$H_2O$, and (2) the formation of a fraction of liquid phase $BaCl_2$-$H_2O$ coating on the surface of the nanoparticles resulting in the decrease in the latent heat. Finally, the viscosity was measured using a cone-and-plate viscometer, and readings showed an increase in viscosity as the loading of nanoparticles increased, with the highest enhancement obtained at a volume loading of 1.13% resulting in a 31.9% enhancement.

However, an inversely proportional relation existed between the temperature and the viscosity; as the temperature increased, the viscosity of the nanofluids decreased.

Meng et al. (2013) investigated the thermal properties of a eutectic mixture of three fatty acids (capric acid, lauric acid, and palmitic acid) as phase change materials with a porous structure carbon nanotubes (CNT) as supporting nano-structures. Capric acid (CA) and lauric acid (LA) were both purchased from Sinopharm Chemical Reagent Co., Ltd., Shanghai, China, while palmitic acid (PA) was purchased from FuChen Chemical Reagent Co., Ltd., Tianjin China. The CNT, with a diameter range of 8-15 nm were obtained from Shenzhen Nanotech Port Co., Ltd., Shenzhen, China. The mixture of the PCM was prepared following a mass ratio of LA:CA:PA of 3:5:2 at a temperature of 80 $^{o}$C for 1.5 h at a stirring speed of 500 rev/min. Then, oxidized CNT were added to the mixture at a loading of 10, 20, 30, 40 and 50 wt% using ultrasonication for one hour. SEM images showed that fatty acids/CNT composites, with CNT contents of 20, 30 and 40 wt%, were homogeneous samples, meaning the CNT were fully absorbed by the acids (Figure 2.15). However, for a 10 wt% loading of CNT, the sample surface was very smooth leading to a leakage of acids at liquid state. As for the highest loading of CNT (50 wt%), the nanotubes were not dispersed uniformly and agglomeration was present. Differential Scanning Calorimetry (DSC, Q1000, America) and the transient plane source technique (Hot Disc 2005, Hot Disc AB, Sweden) were used to obtain the energy storage properties and thermal conductivity of the composites, respectively. Results indicated that CNT had a significant effect on the aforementioned properties. As the loading of CNT increased, the phase change temperature and the latent heat of the composites decreased due to the limitation to the crystal behavior of the fatty acids from the porous structure of the CNT. Moreover, thermal stability tests for up to 30 melting/freezing cycles were conducted on the samples with 20 wt%

loading of CNT, and results showed good thermal stability, since the latent heat and melting point of the sample remained unchanged. As for the thermal conductivity, the data obtained were the average of 3 runs conducted at room temperature. Results showed an increase in thermal conductivity as the loading of CNT increased, with the highest value of 0.6661 W/mK measured at a CNT loading of 50 wt% (Figure 2.16). Furthermore, thermal stability tests were conducted for the fatty acids/CNT composites using the thermogravimetric (TG) method, and results indicated a degradation in two stages: 1st stage at 150 $^o$C resulting from the decomposition of the acids, and a 2nd stage at 550 $^o$C corresponding to the decomposition of the CNT. The authors argued that the degradation temperature of all the composites were almost the same, and that the weight loss was only different in the first stage, and they concluded that the composites had good thermal behavior and cycling stability.

Ji et al. (2012) investigated the thermal conductivity enhancement of palmitic acid (PA)/ multiwalled carbon nanotubes (MWNT) by employing two types of carbon nanotubes: oxidation of MWNT and absorption of pyrogallol on the oxidized MWNT (O-MWNT). In preparing the oxidized samples, commercial MWNT (Shenzhen Nanotech Port Co., China) were purified with addition of aqueous $HNO_3$ at 70 $^o$C for 45 h, and then the nanotubes were oxidized in the mixture of $HNO_3$ and $H_2SO_4$ for 3, 6, 8 and 10 h. Finally, the samples were left to dry in a vacuum chamber at 80 °C. As for the second type of samples, a mixture of 100 mg of O-MWNT and 400 mg of pyrogallol were added to ethanol and then sonicated for a period of 30 min. Finally, the functionalized nanotubes (f-MWNT) were dried at 60 $^o$C. Both O-MWNT and f-MWNT were dispersed in palmitic acid using sonication to prepare the PA/MWNT composites. PA, pyrogallol and ethanol were all bought from Sino- pharm Chemical Reagent Company. Differential Scanning Calorimetry (DSC 131 Evo, SETRAM) was used to measure the latent heat, the

melting temperature, the phase change time, while steady-state heat flow meter (HFM) was used to measure the thermal conductivity. Data showed that the thermal conductivity increased as the mass fraction of carbon nanotubes (1, 2, 3, 5 and 7 wt%) increased, while the latent heat, melting point and the length time for phase change decreased. However, Ji et al. (2012) focused more on the influence of oxygen-containing groups of functionalized MWNT on the thermal conductivity of PA. Results showed that O-MWNT prepared following the 10 h oxidation period exhibited the highest latent heat, phase change time and thermal conductivity when compared to the other oxidation times (0, 3, 6 and 8 h) (Figure 2.17). Furthermore, Ultra Violet-visible spectroscopy (UV-vis) showed that O-MWNT with longer oxidation period have better dispersion in PA because of the increased hydrogen bonding interactions between the PA molecules and the O-MWNT. As for the f-MWNT composites, thermal conductivity enhancement was the greatest among all prepared MWNT composites as seen in Figure 2.17, due to the $\pi - \pi$ interactions between the benzene rings of pyrogallol and the graphitic surface of the nanotubes, leading to a better dispersion in the PA solution. It could be concluded that the f-MWNT provide the best heat transfer performance followed by O-MWNT with extended oxidation period.

Ho and Gao (2013) conducted experimental tests on octadecane-based PCM containing dispersed aluminum oxide ($Al_2O_3$) nanoparticles in a vertical enclosure in order to study the effects of the mass fraction of the nanostructures ($w_p$ = 0, 5 and 10 wt%) on the heat transfer properties. The test cell has a square cross-section of $25 \times 25$ mm and 60 mm in depth. The vertical walls were differentially-heated isothermally, while the remaining walls were insulated. Type-T thermocouples were placed on both walls at different locations to measure the temperature change across the test apparatus with the use of data acquisition software. A complete diagram of the test setup is shown in Figure 2.18. Data recorded showed that the

24

Nusselt number, $Nu_f$, starts at a high value when heating begins, then decreases and finally reaches a quasi-steady state value as natural convection begins to dominate regardless of the mass fraction of the particles. Also, as the weight fraction of the nanoparticles increased, the average Nusselt number values in the quasi-state phase were reduced by more than 60% compared to the base paraffin, due to suppression of natural convection (Figure 2.19). This can be attributed to the far greater increase in the effective dynamic viscosity (about 4 times) than the enhancement of thermal conductivity of the liquid nano-PCM. Moreover, as the temperature of the hot walls increased (32 $^o$C to 40 $^o$C), the melting rate of the PCM was accelerated due to the greater intensity of natural convection, and the total energy transfer was also greatly enhanced. However, when changing the temperature of the cold walls (24 $^o$C and 27.5 $^o$C) and maintaining the temperature of the hot wall at 40 $^o$C, a subcooling effect arises since the cold wall temperature is below the melting temperature of the n-octadecane. The subcooling effect increased as the mass fraction of aluminum oxide nanoparticles increased due to the enhancement of thermal conductivity of the composites. The increasing subcooled cold wall resulted in slowing the melt movement and in impeding the transition from conduction to natural convection-dominated heat transfer state.

Li (2013) prepared composites of nano-graphite (NG)/paraffin and evaluated the thermal properties and microstructure of the composites. The paraffin, supplied by Rubitherm PCMS Co., Ltd., China and possessing a base thermal conductivity of 0.1264 W/mK, was chosen as the base phase change material, while nano-graphite purchased from Beijing Dk Nano Technology Co., Ltd., China, with a diameter of 35 nm was chosen as the nano-enhancers. The samples were prepared by melting the paraffin at 60 $^o$C, and then mixing it with the desired mass fraction of NG (1, 4, 7 and 10 wt%) by agitation and ultrasonication at the same temperature. Finally, the

composites were solidified at 20 °C. Environmental Scanning Electron Microscopy (ESEM) showed that a NG/paraffin composite is more tightly packed than the paraffin and that the nanoparticles were dispersed and completely enclosed by the paraffin, thus creating a better heat transfer structure. Transient Plane Source (TPS) technique was also used to measure thermal conductivity enhancement, and results showed a significant increase in thermal conductivity as the weight fraction of NG increased. For a mass fraction of 10 wt%, the thermal conductivity value was measured to be 0.9362 W/mK, a relative increase of 7.41 times that of the pure paraffin. Finally, Differential Scanning Calorimetry (DSC) was used to determine the latent heat and melting temperature of the paraffin and the PCM composites. Measured data showed a slight decline in the phase change temperature as the mass fraction of NG increased, due to the decrease in the amount of the paraffin. Also, the latent heat of fusion decreased gradually as the amount of NG increased. Thermal conductivity and latent heat values for the pure paraffin and the various NG/paraffin composites are shown in Figure 2.20.

Based on two forms of nano-additives, Chen et al. (2013) prepared various types of graphite nanosheets (GN)/paraffin composites in order to examine the composites' microstructure and thermal properties. The two types of nanosheets were the following: randomly-distributed graphite nanosheets (R-GN) and oriented graphite nanosheets (O-GN). The paraffin and the graphite flakes were obtained from MERU Co., Ltd. (CAS No. 8002-74-2) and A JAHNSON MATTHEY Co., Ltd., respectively. After immersing the natural graphite flakes into an acid solution of 20 vol% $HNO_3$ and 80 vol% $H_2SO_4$, the solution was stirred for a period of 16 h at room temperature. Then the fabricated graphites were ultra-sonicated in alcohol for another 16 h, filtrated and finally dried under vacuum for 48 h at 70 °C to reach the desired thickness (20-100 nm). To obtain the R-GN/paraffin composites, the synthesized graphite

nanosheets were mixed with paraffin and stirred for 30 min at 75 $^{\circ}$C, and finally poured into a mold to solidify at room temperature. As for the O-GN/paraffin composites, these were prepared using a three-roll milling machine, by pouring the mixture into the machine and rolling it for 3 minutes resulting in thinner GN/paraffin composite (0.3-0.5 mm). The mass fractions of GN used were 0.1, 0.5, 1, 2, 3, 4 and 5 wt% for both types of composites and Transmission Electron Microscopy (TEM) image showed the formation of a thin, large-scale and entangled structure during ultrasonication, and it illustrated the hexagonal graphitic crystal structure of the composites (Figure 2.21). Scanning Electron Microscope (SEM) showed that the GN were uniformly dispersed in the paraffin, and that no voids were obtained in the R-GN/paraffin composite for a low particle loading, while the Field Emission Scanning Electron Microscopy (FESEM) showed the relatively parallel orientation of the O-GN because of the shearing factor during milling. Thermal conductivity was measured experimentally using a Laser Flash Analyser (LFA, LFA-447 Nanoflash, NETZSCH, Germany) unit and predicted theoretically using the Maxwell-Eucken model. The experimental data showed good agreement with the theoretical data, proving that the Maxwell-Eucken formula is a good model to predict the thermal conductivity. Results showed that as the mass fraction of GN increased, thermal conductivity rose due to the increase in the amount of graphite. Furthermore, due to the parallel orientation of the O-GN, the contact between GN is reduced. This resulted in a rise in phonon scattering at the GN/paraffin interface and prevented the GN in agglomerating in the composite sheet; thus leading to lower thermal conductivity values than that of the R-GN/paraffin composite, where the GN are uniformly dispersed and in contact with each other. For a loading of 5 wt%, thermal conductivity of an O-GN/composite is 1.68 W/mK; a 37% value of that of the R-GN/composite (4.47 W/mK). This also represents an increase of more than 13 times the thermal conductivity of

pure paraffin. In addition to thermal conductivity measurements, thermal diffusivity was measured and a similar pattern was observed, where the thermal diffusivity increases as the amount of GN increases. Finally, Differential Scanning Calorimetry (DSC) was used to measure the thermal properties of the different GN/paraffin composites. Data collected illustrated an inverse proportionality relation between the mass fraction of GN and the latent heat. As the mass of GN increased, the latent heat decreased due to the reduction of paraffin. However, for the melting temperature and the phase change temperature, no significant change was obtained for both types of GN/composites as the mass fraction of GN increased. The thermal conductivity, the thermal diffusivity and the thermal properties values of the solid pure paraffin and the GN/paraffin composites are illustrated in Figures 2.22 and 2.23, respectively.

A new phase change material (PCM) of organic ester base was examined by Parameshwaran, Jayavel and Kalaiselvam (2013) through inserting silver nano particles (AgNP) resulting in silver nano-based organic ester phase change material (SNOE PCM). AgNP of various mass fraction (0.1, 0.5, 1, 2 and 5 wt%) were added to the pure ethyl cinnamate (EC) PCM following ultrasonication, and the thermal properties of the SNOE PCM were examined. The prepared composites were crystalline in structure as shown by XRD, and were stable for more than 3 months without precipitation. TEM images showed that the size of the nanoparticles were in the range of 10-18 nm and that the AgNP were uniformly dispersed in the base PCM, while FTIR spectra proved that no chemical interaction took place between the AgNP and the EC PCM, due to the absence of any new vibrational peaks in the spectra of the SNOE PCM when compared to that of the base PCM (Figure 2.24). As for the measurement of thermal properties, Differential Scanning Calorimetry (DSC) was used. Data showed that both latent heat of melting and freezing decreased minimally as the amount of AgNP increased due to the

28

reduction in the number of molecules of the base PCM, while there was an almost negligible change in the phase change temperature of the composites when compared to the base PCM. In addition to the thermal properties, thermal conductivity was measured using the Flash Laser Analysis (LFA) method for various SNOE PCM composites in the liquid state. Figure 2.25 illustrates a non-linear increasing relation between the mass fraction of silver nanoparticles and thermal conductivity; as the weight fraction of AgNP increased so did the thermal conductivity, with the highest value of 0.765 W/mK measured at 5 wt%, an improvement of 67% from the thermal conductivity of the pure EC. Furthermore, the increase in silver nanoparticles accelerated the rate of nucleation and growth of the stable PCM crystals, and reduced the cooling time by 3.9–30.8 % and 2.4–11.3 % in the freezing and melting processes for the 1 wt% and 5 wt% loading, respectively.

Using the chemical vapor deposition (CVD) method, Zhou et al. (2013) have prepared three dimensional (3D) graphene on porous aluminum oxide ($Al_2O_3$) substrates in order to improve the thermal and electrical properties of the phase change material (PCM). The graphene/$Al_2O_3$ (G-AAO) composites were synthesized at 1200 °C for three various time periods (30, 60 or 120 min) for the growth of the graphene tubes on the anodic aluminum oxide (AAO). TEM images and Raman spectroscopy illustrated that for a longer growth period, the quality, the number of layers and the structure of the graphite tubes were improved, thus creating a better interconnected graphene network for electrical and thermal transfer. Using the laser flash analyzer (LFA) technique, the thermal conductivity of the AAO and the G-AAO were measured. Results showed an increase in thermal conductivity as the growth period of graphene increased, with the 120 min G-AAO exhibiting a value of 8.28 W/mK, significantly greater than that of the porous $Al_2O_3$ (1.84 W/mK). In addition to that, the sheet resistance decreased, leading to a high

electrical conductivity as the number of graphene layers augmented due to the abundance of pores and the multi-dimensional electron transport pathways. One major application of such composite would be the highly conductive reservoirs used for thermal energy storage. As a result, the authors added a phase change material, stearic acid (SA), to a larger macro porous ceramic in order to obtain an SA-graphene-$Al_2O_3$ composite. Such a composite with high thermal conductivity, and moderate latent heat value of 130 J/g would be a desired choice as a thermal material in electronic devices.

Chen et al. (2012) prepared a multifunctional phase change material by dissolving an amount of pure paraffin wax (PW) in $CH_2Cl_2$, and then added porous carbon nanotube sponges (CNTS) of different mass fraction to obtain PW-CNTS composites. The solution was allowed to dry under low pressure until the $CH_2Cl_2$ solvent evaporated, thus resulting in the formation of solid composites with various loadings of carbon nanotubes. The aforementioned composites formed a highly porous structure, creating a better interconnected carbon network for electrical and thermal transfer. Thermal conductivity of PW-CNTS composites with 10 to 30 wt% loading was measured using the transient hot wire (THW) method for both solid and liquid states at a temperature range of 5-40 °C. Thermal conductivity increased as the weight loading of carbon nanotubes increased in the solid state. In the liquid state, thermal conductivity decreased to about 1 W/mK, but still relatively close to its highest value in the solid phase of 1.2 W/mK. The authors argued the reason is that the carbon network remains undisturbed by the melting of the paraffin wax, and therefore the structure of the composite was still stable. In addition to measuring thermal conductivity, DSC testing was used to measure thermal properties. Results illustrated that a higher latent heat exists for a higher concentration of paraffin wax, and that the samples remained stable for 100 freezing/melting cycles (Figure 2.26). Furthermore, the PW-

CNTS composites could be used for thermal energy storage by applying small voltages or sunlight absorption. For the electro-to-heat storage method, the efficiency of such system rises with increasing voltage. As an example, the efficiency rose from 40.6% to 52.5%, when the voltage was changed from 1.5V to 1.75 V, due to the reduction of the phase change period which reduces the convection heat loss to the environment. As for the photo-to-thermal storage method, the carbon nanotubes are vertically aligned and act as a black body, an indication of a greater absorption of sunlight. As the intensity of the light increases, the energy storage efficiency of the PW-CNTS composites increases. Due to the electro-to-heat and the photo-to-thermal energy storage, the PW-CNTS composites have a wide area of applications, especially in batteries.

Ma et al. (2012) investigated the thermal properties of paraffin wax (PW) based phase change materials with the addition of carbon nanotubes (CNT) by ultrasonication. To improve heat transfer furthermore, metallic (copper) mesh structures were introduced into the PW/CNT composites. Various loadings (2, 5 and 10 wt%) of CNT were added in the preparation of the samples, and thermal conductivity was measured using the KD2 Pro Thermal Properties Analyzer at both liquid and solid states in the range of 20-60 $^o$C. Results showed an increase in thermal conductivity as the mass fraction of CNT increased, with the maximum enhancement recorded at 31.4% and 40.2% at the highest loading of CNT, in the solid and liquid states, respectively. Furthermore, when the temperature of the samples was close to the melting point, thermal conductivity rose significantly, and then dropped to as low as 0.15 W/mK when in liquid state. However, after subjecting various PW/CNT composites to several heating/freezing cycles, thermal conductivity for the 2 and 5 wt% CNT loading decreased greatly as a function of the temperature due the agglomeration of the CNT, while the 10 wt% CNT/PW composite remained the same. In addition to the thermal conductivity measurements, DSC was used and data showed

a decrease in the latent heat and melting temperature as the weight fraction of the CNT increased. As for the addition of the mesh structures, thermocouples were used to measure the transient temperature as a function of time, and results showed a decrease in the charging and discharging time by 40.3% and 30.2%, respectively.

In an effort to improve thermal properties of the PCM N-docosane, Karunamurthy et al. (2012) introduced various volumes (0.01, 0.02, 0.03, 0.04, 0.05, 0.1 and 0.15 vol%) of CuO nanoparticles into the base material using ultrasonication for a period of 8 hours. The Transient Hot Wire (THW) method was used to measure thermal conductivity of seven different composites, and results illustrated an increase in thermal conductivity as the loading of CuO nanoparticles increased. The maximum conductivity, measured at 0.15 vol% loading, was 0.3802 W/mK, a significant increase from that of the pure N-docosane (0.214 W/mK). In addition to the experimental method, the authors predicted the thermal conductivity analytically using the Maxwell-Garnet Equation, and relatively similar results were obtained for both methods at all the various volume concentrations (Figure 2.27). Moreover, the PCM composites showed an improved thermal performance in that the charging and discharging times were improved with the increase of CuO nanoparticle additives.

Harikrishnan et al. (2013) prepared stearic acid-based nanofluids through dispersion of various mass fractions (0.05, 0.1, 0.15, 0.2, 0.25 and 0.3 wt%) of $TiO_2$ by using a two-step method via ultrasonication. The goal behind this study was to examine the thermal and heat transfer characteristics of the prepared phase change materials using Differential Scanning Calorimetry (DSC) for thermal properties testing and Laser Flash Analyzer (LFA) for thermal conductivity measurements. TEM and FTIR images showed that the nanoparticles, with average size of 23 nm, were uniformly dispersed in the base nanofluid and that only a physical reaction

took place between the stearic acid and the $TiO_2$ nanoparticles. DSC data showed a minimal decrease and increase in latent heat and phase change temperature as the loading of the enhancers increased, respectively. Furthermore, stability tests for up to 5000 cycles of melting/freezing processes were conducted. Results showed that the samples remained stable due to maximum decrease in melting and solidification temperatures being 0.35% and 0.59%, respectively and the maximum decline in latent heat being 1.29% and 1.47% in melting and freezing cycles, respectively (Figure 2.28). Those values could be considered negligible, and therefore the heat performance and the energy storage of the PCM would not be affected greatly. In addition to the latent heat measurements, thermal conductivity was measured at room temperature for the various loadings of $TiO_2$ nanoparticles, and the results are plotted in Figure 2.29. As the mass fraction of the nanoparticles increased, thermal conductivity increased with the highest value obtained at a concentration of 0.3 wt% of $TiO_2$ resulting in an enhancement of 70.52% when compared to that of the pure PCM. Due to the increasing thermal conductivity and the relatively similar latent heat values for the various mass fraction of $TiO_2$, the PCM composites present a desirable option for use in thermal energy storage for low-temperature applications.

Ye et al. (2014) examined the thermal stability and thermal properties of $Na_2CO_3/MgO$ composites for high-temperature storage applications that were prepared by mixing a desired weight ratio (40:60, 50:50, 60:40 and 80:20) of $Na_2CO_3$ ($\geq$ 99% purity, Chemical Reagent Co. Ltd., Beijing, China) to MgO ($\geq$ 99% purity, Beijing Chemical Factory, China). Then, multiwalled carbon nanotubes (MWCNT) of different mass fractions (0.1, 0.2, 0.3 and 0.5 wt%) were added to the mixture to obtain the $Na_2CO_3/MgO$ composites. The nanotubes, with a diameter of 11 nm, were purchased from Beijing DK Nano technology Co., China. Before the

addition of MWCNT, XRD and TGA tests were conducted on the $Na_2CO_3/MgO$ composites. X-ray diffraction patterns showed that no chemical interaction existed between the materials. As for the thermal gravity analyses, results illustrated degradation of the $Na_2CO_3/MgO$ composites as the mass of the MgO decreased. The $Na_2CO_3$ served the role of latent heat storage material, while MgO provided the support for a well-percolated network structure for the phase change material. So, as the MgO material decreased in the sample, the thermal stability diminished and the highest mass losses reached about 6.86% for the (80:20) $Na_2CO_3/MgO$ composite (Figure 2.30). As a result, the authors argued that a weight ratio of (60:40) $Na_2CO_3/MgO$ composite possesses the best thermal stability and constitute the optimal candidate for thermal energy storage. Subsequently, a 0.5 wt% MWCNT was added to that composite. TGA analysis of the aforementioned composite showed that the mass loss decreased from 4% to 2.5% from that of the (60:40) $Na_2CO_3/MgO$ composite without MWCNT (Figure 2.31). As for the thermal conductivity, measurements were tested using the guarded heat flow meter method (UNITHERM$^{TM}$ model 2022, Anter Corporation, Pittsburgh, PA) at three temperatures (40, 75 and 120 $^oC$) for various loadings of the MWCNT. Results indicated an increase in thermal conductivity as the mass fraction of the MWCNT increased and as the temperature of the samples increased.

Zhong et al. (2013) introduced three-dimensional graphene aerogel (GA) as thermal enhancer into octadecanoic acid (OA) phase change material to examine its thermal behavior for thermal energy storage. GA was prepared from the graphene oxide's sheets using the one-step hydrothermal method, and then added by capillary forces to a solution of OA at 80 $^oC$ for 1 hour. Finally, the samples were left to solidify and the GA/OA composite was obtained. FESEM images showed that almost 98% of the porous structure of GA was filled with OA, which created

a thermally conductive network between the material, and that no cracking or interfacial separation was present. Laser Flash Analyzer (LFA) was utilized to measure the thermal conductivity at room temperature for the GA/OA composite with a mass fraction of 15 wt% of GA. The thermal conductivity of the GA/OA composite was measured to be 2.635 W/mK, an enhancement of approximately 13 times that of the OA (0.184 W/mK). Furthermore, an infrared camera was used to take photographs at a 1-second interval during the heating/freezing cycles of the composite and pure AO samples in order to investigate its thermal response. Figure 2.32 presents the thermal images taken at several time intervals along with a DSC curve for the heating and freezing cycle. As seen in the images, during the heating cycle (Fig. 2.32a-d), the GA/OA composite reached a higher maximum temperature (70 $^{o}$C) compared to that of OA (60 $^{o}$C) and also had a slower thermal response since it took about 200 s to reach thermal balance compared to the 150 s attributed to the OA sample. On the other hand, during the cooling cycle (Fig. 2.32e-h), the temperature distribution was much higher for the GA/OA composite in comparison with OA, and the temperature at the surface of the GA/OA samples can be maintained stable at the melting temperature (56 °C) of OA for several minutes. These results, along with the latent heat value of the composite (181.8 kJ/kg) which is relatively close to that of OA (186.1 kJ/kg), prove that the GA/OA composite would be a potential candidate in thermal management.

With the goal to develop energy efficient systems, Parameshwaran, Dhamodharan and Kalaiselvam (2013) investigated silver-titania HyTES (hybrid nanocomposite-based cool thermal energy storage) combined with an air conditioning system (A/C) for use in sustainable buildings. Silver-titania HyNC (hybrid nanocomposite) of various mass fractions (0.05 and 1.5 wt%) were dispersed into the base PCM (dimethyl adipate) using ultrasonication to obtain the HyNPCM

(hybrid nanocomposite phase change material). The authors investigated the thermophysical properties of the system both analytically and experimentally for summer and winter conditions. Thermal conductivity of the PCM nanofluid was predicted analytically using the Wasp model discussed in Murshed et al. (2005), with the researchers claiming that the results were similar to the Maxwell and Hamilton and Crosser models for the spherical models. Experimentally, LFA was utilized to measure thermal conductivity. Results showed an increase in thermal conductivity as the mass fraction of the HyNC increased from 0.05 to 1.5 wt% corresponding to thermal conductivity enhancements of 7.3% and 58.4%, respectively. In addition to thermal conductivity, the melting and freezing cycles were also analyzed analytically and experimentally using DSC (Differential Scanning Calorimetry). Results showed a slight change in the latent heat values and phase change temperatures as the loading of silver-titania HyNC augmented; thus maximizing the possibility for effective nucleation and preserving the cooling temperature much below the melting temperature of the HyNPCM. Also, the freezing time was reduced by as much as 15% compared to that of the pure PCM, thanks to the improvement in thermal conductivity and the relatively similar latent heat values when the nanocomposite were introduced. Other than improvement of thermal properties, the HyTES system enhanced energy efficiency, lowered the total energy, and increased energy savings throughout the year. The coefficient of performance (COP) of the HyTES system improved from 1.47 to 4.21 during the summer, while in the winter, COP was increased from 1.43 to 4.1 for the HyTES system. As for the energetic aspects, a conventional A/C system consumed on average 156,596 kWh, while a 0.5 and 1.5 wt% HyTES system consumed 145,264 kWh and 140,603 kWh corresponding to a yearly energy saving potential of 7.2% and 10.2%, respectively. A complete representation of the energy saved per day, per summer/winter and per year is illustrated in Figure 2.33. The enhanced thermophysical

properties and the potential benefits on energy efficiency and savings make the HyTES A/C system an advantageous model for use in buildings.

Wang et al. (2013) prepared a novel type of hybrid material of shape-stabilized PCM by mixing single walled carbon nanotubes (SWCNT) with polyethylene glycol (PEG) using ultrasonication. The SWCNT (2 nm in diameter and 5-10 μm length) were supplied by Shenzhen Nanotech Prot Co., Ltd., China, while PEG, serving as the base PCM, was purchased from Shanghai National Medicines Co. Inc., China. Due to their strong inter-tube Van der Waals interactions, SWCNT are strongly bundled to each other making it very difficult for researchers to dissolve them in organic/inorganic solvents. Thus, Wang et al. (2013) treated the SWCNT surfaces with nitrophenyl groups (4-nitrophenyldiazonium cations) in order to obtain a uniform dispersion of the nanotubes. Multi-walled carbon nanotubes (MWCNT) and carbon black (CB) were also introduced into PEG to create MWCNT/PCM and CB/PCM composites. Upon solar irradiation, the SWCNT/PCM composites' temperature increased due to the absorption of the light, and then the sample transformed the radiation to thermal energy and stored it. Due to solar irradiation, the temperature starts to decrease gradually due to the release of the absorbed heat. In comparing the three type of composites, DSC results showed a minimal change in latent heat of fusion and melting temperature when compared to the pure PCM regardless of the nano-structures. As for thermal conductivity, using the steady-state heat flow meter method, enhancements of 25.1%, 16.9% and 4.9% were obtained for the SWCNT/PCM, MWCNT/PCM and CB/PMC, respectively, when compared to the base material. Moreover, the heating and freezing cycles were much faster for the SWCNT/PCM (870 and 940 s) than those of the MWCNT/PCM (970 and 1075 s) and CB/PMC (1065 and 1195 s) which would improve the heat transfer rate and provide a better efficiency. Furthermore, XRD illustrated the crystalline

structure of the SWCNT/PCM composites, and thermogravimetric analysis (TGA) of up to 100 cycles showed that the SWCNT/PCM exhibited excellent thermal and reversible stability.

Due to the low thermal conductivity of the base fluid in the traditional nanofluid, Zhang and Liu (2013) evaluated a novel type of nano liquid metal for use in thermal management and energy storage. Liquid metal alloys possess a much higher electrical and thermal conductivity than the base fluid in the conventional nanofluid, while maintaining a relatively moderate heat capacity. Figure 2.34 illustrates the thermal conductivity and latent heat of some liquid metals and typical base fluids. Furthermore, liquid metal has a much higher surface tension than that of the base fluid allowing the possibility of a greater concentration of nanoparticles. One barrier to overcome though in development of a nano liquid metal is the uniform dispersion of the nanoparticles in the liquid metal. The authors solved this problem by the preparation of silicon-coated metal powders, such as nickel and iron before the preparation of the nano liquid metal, due to the high affinity of silicon for liquid gallium. Other than the increase in thermal conductivity, the nano liquid metal proved to be a great candidate as a phase change material for energy storage due to its excellent reversibility of phase transition, small phase expansion and heat transfer capacity. Focusing on energy conversion, the nano liquid metal covers a wide range of possibilities like magnetic, electrical, acoustic and solar energy. However, due to the questions that remain unanswered when it comes to the suspension stability and dispersion of nanoparticles, and the experimental approaches in preparing the sample, more work and research are needed to understand the full applications and physical mechanisms of the nano liquid metal.

In order to examine the energy storage and thermal properties of carbon nanofillers enhanced phase change materials, Fan et al. (2013) prepared four types of carbon nanofillers dispersed in paraffin wax, with a melting temperature of 59 $^\circ$C. Short multi-walled carbon

nanotubes (S-MWCNT), carbon nanofibers (CNF), and graphite nanoplatelets (GNP), were obtained from Chengdu Organic Chemicals Co., Ltd, China, while long multi-walled carbon nanotubes (L-MWCNT) were purchased from Shenzhen Nanotech Port Co. Ltd., China. Various types and mass fractions (1, 2, 3, 4 and 5 wt%) of carbon nanofillers were firstly dispersed in the paraffin wax, then shear-mixed using a magnetic stirrer for 15 minutes, followed by ultrasonication for 50 minutes, and finally allowed to solidify at room temperature for about 3 h. Differential Scanning Calorimetry (DSC) was used to measure the phase change temperature and latent heat during both the melting and solidification cycles. DSC curves showed the occurrence of two peaks: the first peak corresponds to a solid-solid phase transition, and the second one represents the solid-liquid phase change of the PCM. DSC data showed a slight decrease in melting temperature; the maximum decline being 1.1 $^{o}$C. As for the solidification temperature, negligible changes were measured for all four types of PCM, except in the case of GNP-enhanced PCM where, surprisingly, the phase change temperature increased. In addition to that, heat of fusion and solidification decreased as the loading of the carbon nanomaterial increased due to the decrease in the paraffin wax. The authors also measured thermal conductivity for all 4 types of carbon nanofillers using the KD 2 Pro Analyzer. Tests were conducted in the solid state, for a temperature range of 10-50 $^{o}$C, on three specimens for each different type of carbon nanofillers. Thermal conductivity measurements of the carbon nanofillers enhanced PCM as a function of temperature is plotted in Figure 2.35. Results showed a decrease in thermal conductivity as the temperature increased, except at 30 $^{o}$C and 50 $^{o}$C. Fan et al. (2013) argued that the increase at 30 $^{o}$C is due to the transition of crystallization structure and absorption of the latent heat related to the first peak, analogous of the solid-solid phase change. And when close to the melting point, a sudden jump was observed in thermal conductivity, which is in good

agreement with other researchers' work. Furthermore, thermal conductivity was increased as the mass fraction of the carbon nanofillers increased. Moreover, the geometry and the size of the nanofillers play a major role in the improvement of thermal conductivity; the enhancement of thermal conductivity is greater for smaller size of the nanofillers. The S-MWCNT exhibited the highest thermal conductivity at 5 wt% loading, a value of 0.324 W/mK, while the L-MWCNT and CNF had values of 0.309 and 0.305 W/mK, respectively. However, GNP possessing a geometry-induced low thermal interface resistance, provided the best enhancement at the same loading; a thermal conductivity value of 0.7 W/mK, equal to an enhancement of 164% (Figure 2.36). However, when comparing the data to other published data on GNP PCM, a discrepancy occurred in the amplitude of the enhancement, indicating a dependence of the performance of GNP on the control of their size and thickness.

Ju et al. (2013) investigated the thermal conductivity of GF/PPS composites experimentally at room temperature using the transient plane source method and computationally using the non-equilibrium molecular dynamics simulation (NEMD). Poly p-phenylene sulfide (PPS) was purchased from Chevron Phillips Chemical Company, while the graphite flakes were obtained from Peilong Enterprise Company. In the preparation of the composites, various weight fraction (5, 10, 20 and 40 wt%) of GF were mixed with the PPS using two methods: an injection method and a hot press process. For low mass fraction of graphite fillers, GF was dispersed uniformly in the solution prepared via the hot press method, while the samples prepared following the injection method exhibited a significant gradient in the concentration of the GF in the samples. When the mass fraction reached a value of 40 wt%, both methods created an improved thermally conductive structure. Thermal conductivity results showed that samples prepared via the hot press method exhibited higher thermal conductivity values when compared

to that of the samples of the injection method. The difference in thermal conductivity becomes even greater as the mass fraction of the fillers increased due to the increased probability of the formation of GF/PPS networks. The COMPASS (Condensed-phase Optimized Molecular Potential for Atom Simulation Studies) force field and the Maxwell-Eucken model, for the NEMD simulation and analytical solution, were used to determine the thermal conductivity of the GF/PPS composites, respectively. Figure 2.37 represents the thermal conductivity of the pure PPS and the GF/PPS composites prepared following the experimental, analytical and NEMD methods. NEMD simulation and Maxwell-Eucken model results matched those obtained from the experimental methods. And once again, for low mass fraction of graphite fillers (10 wt% or less), the enhancement of thermal conductivity was negligible, but as the mass fraction of GF increased, thermal conductivity improved significantly.

Liu et al. (2013) prepared carbon nanotubes array (CNTA) by chemical vapor deposition (CVD) method, and then added eicosane ($C_{20}H_{42}$) as phase change material to the porous structure of the CNTA to create a highly conductive network between the materials. In order to keep the carbon nanotubes (CNT) close to each other and increase the interfacial area per unit volume, lateral compression took place. The CNTA-$C_{20}$ composite were compressed to strains of 20 and 40%, thus reducing the volume of the composite, but still maintaining the alignment of the CNT and increasing its area density since they are closer to each other. SEM images of the compressed composites illustrated that CNT were well-dispersed in the matrix and proved the higher density of CNT obtained by compressing the array before the infiltration of eicosane and solidification of the samples. Differential Scanning Calorimetry (DSC) tests were repeated for up to 100 cycles of melting/freezing cycles, which resulted in great reproducible data of latent heat and melting temperature for the composites. For the compressed composites, the phase change

temperature differed slightly from that of the pure eicosane, and the transition periods for the endothermic and exothermic reaction were shortened when compared to the original eicosane array. Thermal gravitational analysis showed that weight reduction in the composites doesn't occur until a temperature of 250 $^o$C in the compressed composites, up from the 200 $^o$C for the pure eicosane. Furthermore, the authors investigated and compared the electro-to-heat energy storage efficiency and stability of the CNTA-C$_{20}$ composites by applying a desired amount of voltage (1 to 2 V) and measuring the temperature evolution inside the composite by a Pt sensor. It was found that for CNTA samples of 20 and 40% compression strains, a mere voltage of 1.4-1.7 V and 1-1.3 V is enough for the eicosane to undergo complete phase transition, respectively. As for the pure eicosane, a voltage of 2 V is required for the PCM to melt completely. This indicates a heat transfer enhancement and a reduction in bulk resistance resulting from the addition of the nanotubes. As for the storage efficiency, the CNTA-C$_{20}$-c20% provided an efficiency of 74.7% at 1.3 V, while the CNTA-C$_{20}$-c40% composite resulted in an efficiency of 38.9% at 1.7 V. It must be noted that a higher voltage prompts shorter phase change time and less convection heat loss, which will result in improved efficiency. Finally, after stability tests of 100 melting and freezing cycles, the CNTA-C$_{20}$-c40% composite showed no degradation and a slight decrease in efficiency, down to 70%.

An aqueous solution of polyethylene glycol (PEG)/sulfonated graphene (SG) composite was prepared by Li et al. (2013). Various mass fractions (1, 2, 3 and 4 wt%) of SG was introduced into the phase change material, polyethylene glycol, by sonication at room temperature, followed by stirring at 80 $^o$C for 4 h. Finally, the samples were left to solidify inside a vacuum oven at 70 $^o$C for 48 h. Once solidified, thermal conductivity measurements were carried out using the Laser Flash Analyzer technique at a temperature of 37 $^o$C. Thermal

conductivity values of pure PEG and PEG/SG composites as a function of the mass fraction of SG are plotted in Figure 2.38. The authors claimed the uncertainty to be in the range of 5%. Results showed an increase in thermal conductivity as the loading of the nanofillers increased, with the highest value (1.042 W/mK), measured at 4 wt% loading, being four times greater than that of the measured value of pure PEG (0.263 W/mK). SEM and TEM images of the surfaces of the composites showed good compatibility between the PCM and the nanofillers, and that the SG sheets were overlapping layer by layer and well dispersed in the PEG matrix, thus creating an effective thermal conductive network resulting in the increase of thermal conductivity. Differential Scanning Calorimetry (DSC) was also used by the authors to investigate the thermal properties of PEG/SG samples. Results showed a decrease in the latent heat and insignificant change in melting temperature of the composites as the weight fraction of the nanofillers increased, due to reduction in PCM volume that undergoes phase transition. Moreover, three DSC runs were conducted on the 4 wt% PEG/SG composite at 75 $^{\circ}$C, a temperature above the melting point of PEG (61 $^{\circ}$C), and results showed minimal decrease in latent heat values (~2%), thus proving that no considerable leakage of PEG occurred in the solution.

Zeng et al. (2013) investigated the melting rate of multi-walled carbon nanotubes-enhanced phase change materials. 1-dodecanol ($C_{12}H_{26}O$) served the role of the base PCM, while multi-walled carbon nanotubes (MWCNT), purchased from Timesnano Co. Ltd., China, played the role of nano-enhancers. Various mass fractions (0, 1 and 2 wt%) of MWCNT were dispersed into the solution by shear-mixing followed by sonication at high temperature to ease the dispersion of the nanostructures. In order to examine the melting process of the pure 1-dodecanol and the PCM composites, a bottom-heated aluminum cylindrical cavity was designed and constructed. Also, eleven type-K thermocouples (TC) were placed at different locations of the

test cell to record the transient temperature changes of the samples, and the TC's readings were recorded by a digital acquisition system. The composite was pre-melted before being poured in the test cell, then the sample was left to solidify at room temperature. Once solidified, the temperature setting of the bath was set to 50 $^o$C, and melting began; a process that took nearly a period of one hour. In the initial phase of melting, the addition of MWCNT had inconsiderable effect on the melting cycle. However, after 150 s, natural convection initiated, and although still weak at this phase, the melting process was faster for the 1 and 2 wt% composites due to the increase in thermal conductivity of the MWCNT-enhanced PCM samples resulting from the addition of the nanofillers. Thermal conductivity measurements were conducted using the transient plane source technique (TPS 2500S) in the liquid state at 40 $^o$C, and results showed an increase in thermal conductivity for the aforementioned samples, an enhancement of 4.6% and 11%, respectively, which lead to enhanced heat transfer. Recorded data exhibited that the loss of natural convection outweighs the enhanced conduction provided by the addition of the MWCNT, which leads to a slower melting process compared to that of the pure PCM; the pure 1-dodecanol is free of nanofillers, therefore the melting is dominated by natural convection. As the weight fraction of the MWCNT increases, natural convection becomes less marked and vanishes for the 2 wt% loading. Furthermore, the decrease in natural convection was evaluated by Zeng et al. (2013) using variation of the Grashof number, and just as determined experimentally, the Grashof number was calculated to decrease significantly with the addition of the MWCNT, proving the decline of natural convection.

Fang et al. (2013) prepared eicosane-based PCM composites through dispersion of various mass fractions (0, 1, 2, 3, 5 and 10 wt%) of graphene nanoplatelets (GNP). Eicosane ($C_{20}H_{42}$) was purchased from TCI Company, Ltd., China, while the nanostructures were provided

by Chengdu Organic Chemicals Co., Ltd., China. Thermal conductivity was measured using the Transient Plane Source technique (TPS 2500S, Hot Disk. AB, Sweden) in the solid state for a temperature range of 10 to 35 $^{o}$C. Thermal conductivity data for the pure eicosane and GNPs/eicosane-based PCM for different loading of nanoplatelets are plotted in Figure 2.39. Results showed an increase in thermal conductivity as the mass fraction of GNP increased, with the highest enhancement obtained at a loading of 10 wt%, an improvement of more than 400% compared to pure eicosane (0.4148 W/mK). The authors attributed this increase to the high thermal conductivity of the GNP, and more significantly to the low eicosane/GNP thermal interface resistance. An analytical model was used by Lin et al. (2010) to predict the thermal conductivity of PCM with the effect of the filler/matrix interface resistance. The same model was used by Fang et al. (2013), and results showed a thermal interface between $6\times10^{-9}$ and $10^{-9}$ m$^{2}$ K/W, with thermal conductivity increasing as the interface resistance decreased as observed in Figure 2.40. Furthermore, at temperatures close to the melting point (37 $^{o}$C), a sudden rise in thermal conductivity was observed for the PCM composites; with the authors claiming that the transition of crystalline structure along with molecular vibrations of eicosane near the transition temperature is responsible for such behavior. In addition to thermal conductivity measurements, the heat of fusion and melting temperature were measured using Differential Scanning Calorimetry (DSC. Netzsch DSC 200 F3). Results showed a decrease in the latent heat as the mass fraction of the GNP increased with the highest reduction occurring at 10 wt% of GNP; a drop of 16% from that of the pure eicosane. As for the transition temperature, insignificant change occurred ($\pm$0.2 $^{o}$C) as the loading of GNP increased. The elevated thermal conductivity of the eicosane-based GNP composites, even with the slight reduction in heat storage capacity, makes the aforementioned samples desirable for thermal energy storage applications

Table 2.1    Summary of studies on thermal conductivity enhancement of Nanostructure-enhanced Phase Change Materials (NePCM) (papers are listed chronologically according to the date received by the editor of the respective journal)

| Authors (year) | PCM | | Nano-Structured Materials | | |
|---|---|---|---|---|---|
| | Material | Properties | Materials | Properties, Dimensions, etc. | Concentration of Enhancers |
| **Sanusi et al. (2010)** | Blended paraffin | $T_m$: 54-58 $^o$C<br>$m$: 100 g-2.8 kg | Graphite nano-fibers (GNF) | Diameter: 2-100 nm<br>Length: up to 100 $\mu$m | 10 wt% |
| **Mei et al. (2011)** | Capric acid (CA) | $T_m$: 29 $^o$C<br>$\Delta H$: 139.77 kJ/kg<br>$T_f$: 25.57 $^o$C<br>$\Delta H_f$: 140.12 kJ/kg<br>$k$: 0.2-0.3 W/mK | Graphite | N/A | 5 wt% |
| **Chintakrind a et al. (2011)** | Organic paraffin wax (IGA-1230A) | $T_m$: 54 $^o$C<br>$\Delta H$: 220 kJ/kg<br>$k$: 0.25 W/mK<br>$C_p$: 2700 J/kgK<br>$\rho_s$: 880 kg/m$^3$<br>$\rho_l$: 745 kg/m$^3$ | Graphite nano-fibers (GNF) | Diameter: 50-100 nm<br>Length: ~ 100 $\mu$m | 10 wt% |
| | | | Graphite foam | Total porosity: 61%<br>Mean pore diameter: 350 $\mu$m<br>$k$ (in plane): 245 W/mK<br>$k$ (out of plane): 70 W/mK | N/A |
| | | | Aluminum foam | 40 PPI ( pores per inch)<br>Relative density: 8-10%<br>$K_p$= 1.44x10$^{-9}$ m$^2$<br>Mean pore size: 500 $\mu$m<br>$k$: 5 W/mK | N/A |
| **Ehid and Fleischer (2012)** | Paraffin wax (IGA-1230A) | $T_m$: 57 $^o$C<br>$\Delta H$: 197 kJ/kg<br>$\alpha$: 3.7x10$^{-6}$ m$^2$/s<br>$k$: 0.25 W/mK<br>$C_p$: 2.7 kJ/kgK<br>$\rho_s$: 880 kg/m$^3$<br>$\rho_l$: 645 kg/m$^3$ | High density polyethylene (HDPE)[1] | $T_m$: 130 $^o$C<br>$\Delta H$: 154 kJ/kg<br>$k$: 0.46 W/mK<br>$C_p$: 1.8 kJ/kgK<br>$\rho$: 940 kg/m$^3$ | 0, 10, 20, 30, 40 and 50 wt% |
| **Ehid et al. (2012)** | Paraffin wax (IGA-1230A) | $T_m$: 57 $^o$C<br>$\Delta H_m$: 197 kJ/kg<br>$\alpha$: 3.7x10$^{-6}$ m$^2$/s<br>$k$: 0.25 W/mK<br>$C_p$: 2.7 kJ/kgK<br>$\rho_s$: 880 kg/m$^3$<br>$\rho_l$: 645 kg/m$^3$ | High density polyethylene (HDPE)[1] | $T_m$: 130 $^o$C<br>$\Delta H$: 154 kJ/kg<br>$k$: 0.46 W/mK<br>$C_p$: 1.8 kJ/kgK<br>$\rho$: 940 kg/m$^3$ | 10, 20, 30, 40 and 50 wt% |
| | | | Graphite nano-fibers (GNF) | Diameter: 2-1000 nm<br>Length: up to 100 $\mu$m | 5 wt% |
| **Zhang et al. (2012)** | Polyethylene glycol (PEG) | $T_m$: 50.9 $^o$C<br>$\Delta H_m$: 178.3 kJ/kg<br>$T_f$: 35.7 $^o$C<br>$\Delta H_f$: 160.6 kJ/kg<br>$k$: 0.293 W/mK | Graphite nanoplatelets (GnP) | Diameter: 35 $\mu$m<br>Thickness: 80 nm | 1, 2, 4, 6 and 8 wt% |
| **Jia et al. (2013)** | NanoFluid (Deionized | Average Size: 200-300 nm | Titanium dioxide | Diameter: 10-15 nm | 0.05-1 wt% |

46

| | | | nanoparticles (TiO$_2$ NP) | | |
|---|---|---|---|---|---|
| **He et al. (2012)** | NanoFluid (BaCl$_2$-H$_2$O+ TiO$_2$) | N/A | Titanium dioxide nanoparticles (TiO$_2$ NP) | Average Diameter: 20 nm | 0, 0.07, 0.13, 0.25 and 0.50 wt% |
| **Meng et al. (2013)** | Mixture of Capric Acid (CA) + Lauric Acid (LA) + Palmitic Acid (PA) | $T_m$: 16.8 °C $\Delta H$: 140.5 kJ/kg | Carbon nanotubes (CNT) | Outer Diameter: 8-15 nm Length: 50 $\mu$m | 0, 10, 20, 30, 40 and 50 wt% |
| **Ji et al. (2012)** | Palmitic Acid (PA) | $\Delta H$: 207.6 kJ/kg | Multiwalled carbon nanotubes (MWCNT) | Diameter: 20-40 nm Length: 10-15 $\mu$m | 1, 2, 3, 5 and 7 wt% |
| **Ho and Gao (2013)** | n-Octadecane | N/A | Aluminum oxide nanoparticles (Al$_2$O$_3$) | N/A | 0, 5 and 10 wt% |
| **Li (2013)** | Paraffin | $k$: 0.1264 W/mK | Nano-graphite (NG) | Diameter: 35 nm Purity: 99.95% | 1, 4, 7 and 10 wt% |
| **Chen et al. (2013)** | Paraffin | $\rho_s$: 574 kg/m$^3$ $k$: 0.33 W/mK | Graphite nanosheets (GN) | Thickness: 10-30 nm $\rho_s$: 170 kg/m$^3$ $k$: 47.19 W/mK $SSA$: 122.36 m$^2$/g | 0.1, 0.5, 1, 2, 3, 4 and 5 wt% |
| **Parameshwaran et al. (2013)** | Ethyl cinnamate | $\Delta H$: 94.1 kJ/kg $k$: 0.257 W/mK $T_m$: 7.74 °C $T_f$: 5.69 °C | Silver nanoparticles (AgNP) | Diameter: 10-18 nm | 0.1, 0.5, 1, 2 and 5 wt% |
| **Zhou et al. (2013)** | Aluminum Oxide (Al$_2$O$_3$) ceramics | Mean Pore Size: 95 nm Mean pore center to center distance: 115 nm $R_s$: > 10$^7$ Ω $\sigma$: < 10$^{-7}$ S/m $k$: 1.84 W/mK $\alpha$: 1.07 mm$^2$/s | Graphene tubes | Diameter: 80-120 nm $\sigma$: 950 S/m | N/A |
| **Chen et al. (2012)** | Paraffin Wax | $T_m$: 20 °C $\Delta H$: 136 kJ/kg $k$: 0.16-0.2 W/mK | Carbon nanotubes sponge (CNTS) | Diameter: 20-30 nm Length: 10 $\mu$m | 10, 20 and 30 wt%[2] |
| **Ma et al. (2012)** | Paraffin Wax | $T_m$: 53 °C $\Delta H$: 145.92 kJ/kg | Carbon nanotubes (CNT) | Diameter: 20-30 nm Length: 30 $\mu$m Specific surface area: 200 m$^2$/g | 2, 5 and 10 wt% |
| **Karunamurthy et al. (2012)** | Paraffin (N-docosane) | $T_m$: 52-55 °C $\Delta H$: 190 kJ/kg $k$: 0.214 W/mK $C_{p,s}$: 1.94 kJ/kgK $C_{p,l}$: 2.4 kJ/kgK $\rho_s$: 785 kg/m$^3$ | CuO nanoparticles | $k$: 6540 W/mK | 0.01, 0.02, 0.03, 0.04, 0.5, 0.1 and 0.15 vol% |
| **Harikrishna** | Stearic Acid | $T_m$: 57-59 °C | TiO$_2$ | Diameter: 17-85 nm | 0.05, 0.1, 0.15, |

| | | | nanoparticles | | 0.2, 0.25 and 0.3 wt% |
|---|---|---|---|---|---|
| **Ye et al. (2014)** | Na$_2$CO$_3$/ MgO | $T_m$: 851 °C<br>Purity ≥ 99% | Multi-walled carbon nanotubes (MWCNT) | Diameter: 11 nm<br>Length: 10 $\mu$m<br>Purity ≥ 95% | 0.1, 0.2, 0.3 and 0.5 wt% |
| **Zhong et al. (2013)** | Octadecan-oic acid (OA) | $T_m$: 56 °C<br>$k$: 0.184 W/mK<br>$\rho_s$: 0.84 g/cm$^3$<br>$C_p$: 2.3 kJ/kgK<br>α: 0.095 mm$^2$/s<br>$\Delta H$: 186.1 kJ//kg | Graphene aerogel (GA) | $k$: 2.183 W/mK<br>$\rho_s$: 0.227 g/cm$^3$<br>$C_p$: 1.121 kJ/kgK<br>α: 8.58 mm$^2$/s | 15 wt% |
| **Parameshwa ran and Kalaiselvam (2013)** | Dimethyl adipate (DMA) | $T_m$: 9.7 °C<br>$\Delta H_m$: 164.5 kJ/kg<br>$T_f$: 9.5 °C<br>$\Delta H_f$: 164.6 kJ/kg<br>$k$: 0.358 W/mK | AgTiO$_2$ HyNC (Silver-titania hybrid nano-composite) | Diameter: 60-98 nm | 0.05 and 1.5 wt% |
| **Wang et al. (2013)** | Polyethylene glycol toluene-2,4-diisocyanate (PEG:TDI) | $T_m$: 51.7 °C<br>$\Delta H_m$: 100.3 kJ/kg<br>$T_f$: 30.4 °C<br>$\Delta H_f$: 100.2 kJ/kg<br>$k$: 0.267 W/mK | Single walled carbon nanotubes (SWCNT) | Diameter: < 2 nm<br>Length: 5-10 $\mu$m<br>Specific surface area: 350-400 m$^2$/g<br>Purity: 90% | 1, 2, 3, 4 and 5 wt% |
| | | | Multi-walled carbon nanotubes (MWCNT) | Diameter: 8-15 nm<br>Length: 0.5-2 $\mu$m<br>Specific surface area: > 233 m$^2$/g<br>Purity: > 95% | N/A |
| | | | Carbon Black (CB) | N/A | N/A |
| **Zhang and Liu (2013)** | Several Liquid Metals | N/A | CNTs, Gold (Au), Silver (Ag) and Copper (Cu) | N/A | 0.02, 0.05, 0.08, 0.1, 0.15 and 0.2 vol% |
| **Fan et al. (2013)** | Paraffin Wax | $T_m$: 59 °C<br>$\Delta H_m$: 207 kJ/kg<br>$T_f$: 51 °C<br>$\Delta H_f$: 205 kJ/kg<br>$k$: 0.263 W/mK | Short multi-walled carbon nanotubes (S-MWCNT) | Diameter: 8-15 nm<br>Length: 0.5-2 $\mu$m<br>Purity: > 95% | 1, 2, 3, 4 and 5 wt% |
| | | | Long multi-walled carbon nanotubes (L-MWCNT) | Diameter: 30-50 nm<br>Length: 5-15 $\mu$m<br>Purity: > 97% | 1, 2, 3, 4 and 5 wt% |
| | | | Carbon nano fibers (CNF) | Diameter: 150-200 nm<br>Length: 10-30 $\mu$m<br>Purity: > 95% | 1, 2, 3, 4 and 5 wt% |
| | | | Graphite nanoplatelets (GNP) | Diameter: 5-10 nm<br>Thickness: 420 nm<br>Purity: > 99% | 1, 2, 3, 4 and 5 wt% |
| **Ju et al. (2013)** | Poly(p-phenylene sulfide) (PPS) | $T_m$: 280-290 °C<br>$k$: 0.23-0.26 W/mK<br>$\rho$: 1.28 kg/m$^3$ | Graphite flake (GF) | N/A | 5, 10, 20 and 40 wt% |
| **Liu et al. (2013)** | Eicosane (C$_{20}$H$_{42}$) | $T_m$: 35.68 °C<br>$\Delta H_f$: 242.38 kJ/kg<br>$k$: 0.26 W/mK | Carbon nanotubes (CNT) | N/A | 10 wt% |

| Li et al. (2013) | Polyethylene glycol (PEG) | $k$: 0.263 W/mK<br>$T_m$: 61 $^o$C | Sulfonated graphene (SG) | N/A | 0, 1, 2, 3 and 4 wt% |
|---|---|---|---|---|---|
| Zeng et al. (2013) | 1-dodecanol ($C_{12}H_{26}O$) | $T_m$: 22 $^o$C<br>$k$: 0.154 W/mK<br>$\Delta H_f$: 231.4 kJ/kg<br>$\rho$: 800 kg/m$^3$<br>$\beta$: 0.001 K$^{-1}$ | Multi-walled carbon nanotubes (MWCNT) | Diameter: 8-15 nm<br>Length: 0.5-2 $\mu$m<br>$k$ : 2000 W/mK | 0, 1 and 2 wt% |
| Fang et al. (2013) | Eicosane ($C_{20}H_{42}$) | $T_m$: 37 $^o$C<br>Purity: > 99%<br>$k$: 0.4148 W/mK<br>$\Delta H_f$: 262 kJ/kg | Garphene nanoplatelets (GNP) | Purity: > 99.5%<br>Diameter: 5-10 $\mu$m<br>Thickness: 4-20 nm | 0, 1, 2, 5 and 10 wt% |

[1] Represents a polymer used as a shape-stabilizer to the PCM and not nano-enhancers.

[2] These loadings were only used for thermal conductivity enhancement. Different weight fractions of carbon nanotubes were added to measure other properties.

Table 2.2    Summary of preparation, characterization methods and instruments for studies of colloidal dispersions utilized as Nano-enhanced Phase Change Materials (NePCM) (papers are listed chronologically according to the date received by the editor of the respective journal)

| Authors (year) | Preparation | | Characterization | | Study of Heat Transfer | |
|---|---|---|---|---|---|---|
| | Methods | Dispersion and Stabilization[1] | Thermal Conductivity [2] | Other Measurements and Instruments | Stability Concerns | |
| Sanusi et al. (2010) | Two-step | Ultrasonication Manual mixing | N/A | Particle Size, TEM[3] | Observed by TEM | TC[4] readings for melting/ freezing experiments |
| Mei et al. (2011) | Two-step | Ultrasonication | THW[5], S-1T | Brunauer-Emmet-Teller Surface Area, SSAA[6]  Microstructure, TEM, FTIR[7]  Thermal Properties, DSC[8] | Visually Observed; thermal stability tests for up to 50 cycles of melting/ freezing cycles | TC readings for melting/ freezing experiments |
| Chintakrinda et al. (2011) | Two-step | Ultrasonication | N/A | N/A | Observed agglomeration after multiple melting/ solidification cycles | TC readings for melting |
| Ehid and Fleischer (2012) | Two-step | Magnetic Stirring | N/A | Volume contraction, Denver Instruments Digital  Hardness, A-Scale Shore Durometer  Latent heat and melting temperature, DSC | N/A | TC readings for melting/ freezing experiments |
| Ehid et al. (2012) | Two-step | Sonication | N/A | N/A | Thermal stability tests for up to 20 cycles of melting/ | TC readings for melting/ freezing experiments |

| | | | | | freezing cycles | |
|---|---|---|---|---|---|---|
| **Zhang et al. (2012)** | Two-step | Ultrasonication Surfactant: Azobisisobutyro nitrile (AIBN) | TPS[9], S-1T | Morphology, FESEM[10]  Microstructure, XRD[11]  Chemical Properties, FTIR  Electrical Conductivity, Four Probe Method  Thermal Properties, DSC  Thermal Stability, TGA[12] | Observed by FESEM.  The prepared samples were stable since the maximum temperature was 80 $^{o}$C, but degradation would occur at 175-220 $^{o}$C and again at 300-312 $^{o}$C | N/A |
| **Jia et al. (2013)** | Two-step | Ultrasonication Surfactant: Sodium dodecyl sulfate (SDS) | N/A | Thermal properties, DSC  Particle Dimensions, DLS[13]  Stability, AS[14] | TiO$_2$ NF < 0.15 wt% and TiO$_2$ NF > 0.7 wt% were unstable | N/A |
| **He et al. (2012)** | Two-step | Ultrasonication Surfactant: hydrophilic | THW, SL-mT | Particle Size, TEM  Supercooling effect, DAS[15]  Latent heat and specific heat, DSC  Viscosity, CPV[16] | Observed by TEM, thermal stability tests for up to 50 cycles of melting/ freezing cycles | TC readings for melting/ freezing experiments  Uncertainty measurement for the super cooling degree data |
| **Meng et al. (2013)** | Two-step | Ultrasonication | TPS, S-1T | Microstructure of CNT, FTIR  Morphology, NAD[17], and SEM[18]  Thermal Stability, TGA  Thermal Properties, DSC | Observed by SEM; thermal stability tests for up to 30 cycles of melting/ freezing cycles | N/A |

| | | | | | | |
|---|---|---|---|---|---|---|
| **Ji et al. (2012)** | Two-step | Sonication | HFM[19], S-1T | Characterization of MWNT, XPS[20], FTIR, <br><br> Solar radiation, UV-vis[21] <br><br> Thermal properties, DSC | N/A | N/A |
| **Ho and Gao (2013)** | Two-step | Ultrasonication | N/A | N/A | N/A | TC readings for melting experiments |
| **Li (2013)** | Two-step | Agitation and Ultrasonication | TPS, S-1T | Microstructure, ESEM[22] <br><br> Thermal properties, DSC | Visually Observed | N/A |
| **Chen et al. (2013)** | Two-step | Ultrasonication | LFA[23], S-1T | Morphology, FESEM <br><br> Brunauer-Emmet-Teller Surface Area, SSAA <br><br> Thickness, AFM[24] <br><br> Thermal properties, DSC <br><br> Microstructure, TEM | Visually Observed | N/A |
| **Parameshwaran et al. (2013)** | Two-step | Ultrasonication | LFA, L-1T | Crystallization, XRD <br><br> Thermal Stability, TGA <br><br> Microstructure and morphology, TEM, FTIR <br><br> Thermal properties, DSC | Observed by TEM; Samples were stable for more than 3 months without any precipitation | N/A |
| **Zhou et al. (2013)** | Two-step | Chemical Vapor Deposition (CVD) | LFA, S-1T | Morphology and microstructure, FESEM, HRTEM[25], SEM and TEM <br><br> Quality and layer number of graphene, | N/A | N/A |

| | | | | RS[26]<br><br>Electrical Properties, VdP[27]<br><br>Thermal properties, DSC<br><br>Surface chemistry, XPS | | |
|---|---|---|---|---|---|---|
| **Chen et al. (2012)** | Two-Step | Chemical Vapor Deposition (CVD) | THW, SL-mT | Crystallization, XRD<br><br>Morphology, SEM<br><br>Thermal properties, DSC<br><br>Thermal Stability, TGA | Thermal stability tests for up to 50 cycles of melting/ freezing cycles | N/A |
| **Ma et al. (2012)** | Two-Step | Ultrasonication | KD2 Pro, SL-xT | Thermal Properties, DSC | Thermal stability tests for up to 3 cycles of melting/ freezing cycles | TC readings for melting/ freezing experiments |
| **Karunamurt hy et al. (2012)** | Two-Step | Ultrasonication | THW, S-1T | N/A | N/A | N/A |
| **Harikrishna n et al. (2013)** | Two-Step | Ultrasonication<br><br>Surfactant: Sodium dodecyl benzene sulfonate (SDBS) | LFA, S-1T | Morphology and microstructure, TEM and FTIR<br><br>Crystallization, XRD<br><br>Thermal Properties, DSC | Observed by TEM; thermal stability tests for up to 5000 cycles of melting/ freezing cycles | TC readings for melting/ freezing experiments |
| **Ye et al. (2014)** | Two-Step | Mixed and sintered in a furnace | Steady-state guided heat flow meter, S-xT | Morphology, SEM<br><br>Crystallization, XRD<br><br>Thermal Stability and Characterization, TGA and DSC | Observed by SEM; thermal stability tests from 25 to 900 $^{\circ}$C, degradation occurred (lower than 5 %) | N/A |
| **Zhong et al. (2013)** | Two-Step | Capillary forces | LFA, S-1T | Crystallization, XRD<br><br>Morphology, FESEM | N/A | N/A |

| | | | | | | |
|---|---|---|---|---|---|---|
| | | | | Thermal Properties, DSC | | |
| **Parameshwaran and Kalaiselvam (2013)** | Two-Step | Ultrasonication | LFA, S-1L | Microstructure and Morphology, FESEM, TEM, and EDAX[28] | Observed by TEM | N/A |
| | | | | Thermal Properties, DSC | | |
| **Wang et al. (2013)** | Two-Step | Ultrasonication | Steady-state heat flow meter, S-1T | Solar radiation, UV-vis | Thermal and reversible stability tests for up to 100 cycles of melting/ freezing cycles | N/A |
| | | | | Microstructure, FTIR and PNMR[29] | | |
| | | | | Thermal properties, DSC | | |
| | | | | Thermal stability, TGA | | |
| | | | | Crystallization, XRD | | |
| **Zhang and Liu (2013)** | Two-Step | Ultrasonication and mechanical vibration | N/A | N/A | N/A | N/A |
| **Fan et al. (2013)** | Two-Step | Melt-mixing scheme; dispersion, then shear mixing, followed by ultrasonication | KD2 Pro, S-xT | Microstructure and Morphology, SEM, AFM and TEM | Observed by TEM and SEM | TC readings to measure thermal equilibrium between temperatures of bath and samples |
| | | | | Thermal Properties, DSC | | |
| **Ju et al. (2013)** | Two-Step | Injection and hot press methods | TPS, S-1T | Microstructure, SEM | N/A | N/A |
| | | | | Molecular Dynamics, COMPASS[30] force field | | |
| **Liu et al. (2013)** | Two-Step | Chemical Vapor Deposition (CVD) followed by a melt impregnation method | N/A | Microstructure, SEM | Observed by SEM, thermal stability tests for up to 100 cycles of melting/ freezing cycles | N/A |
| | | | | Thermal Properties, DSC | | |
| | | | | Thermal stability, TGA | | |
| | | | | Crystallization, XRD | | |

| Li et al. (2013) | Two-Step | Sonication | LFA, S-1T | Microstructure and morphology, FTIR, TEM, SEM and POM[31] Crystallization, XRD Density, Vibrating tube densimeter Thermal Properties, DSC | Observed by SEM | N/A |
|---|---|---|---|---|---|---|
| Zeng et al. (2013) | Two-Step | Shear mixing followed by sonication | TPS, L-1T | Microstructure and Morphology, TEM and SEM Dynamic Viscosity, Rotational Viscometer Thermal Properties, DSC | Visually observed, observed some precipitation after 3 melting/ freezing cycles | TC readings for melting experiments |
| Fang et al. (2013) | Two-Step | Stirring followed by sonication | TPS, S-xT | Microstructure and Morphology, TEM, SEM and AFM Thermal Properties, DSC | Observed by TEM | TC readings for temperature variations measurements |

[1] This column is only applicable to the two-step method.

[2] Under thermal conductivity column, SL-$x$T stands for S = solid phase, L = liquid phase, $x$ = 1 for single and m for multiple, T = temperature measurements.

[3] TEM denotes transmission electron microscopy.

[4] TC denotes thermocouples.

[5] THW denotes transient hot wire method.

[6] SSAA denotes specific surface area analyzer.

[7] FTIR denotes Fourier transform infrared spectroscopy.

[8] DSC denotes differential scanning calorimetry.

[9] TPS denotes transient plane source technique.

[10] FESEM denotes field emission scanning electron microscopy.

[11] XRD denotes X-ray diffraction.

[12] TGA denotes thermogravimetric analysis.

[13] DLS denotes dynamic light scattering.

[14] AS denotes absorption spectroscopy.

[15] DAS denotes data acquisition software.

[16] CPV denotes cone-and-plate viscometer.

[17] NAD denotes nitrogen adsorption-desorption measurement.

[18] SEM denotes scanning electron microscopy.

[19] HFM denotes heat flow meter.

[20] XPS denotes X-ray photon spectroscopy.

[21] UV-vis denotes ultra violet-visible spectroscopy.

[22] ESEM denotes environmental scanning electron microscopy.

[23] LFA denotes laser flash analyzer.

[24] AFM denotes atomic force microscopy.

[25] HRTEM denotes high resolution transmission electron microscopy.

[26] RS denotes Raman spectroscopy.

[27] VdP denotes Van der Pauw method.

[28] EDAX denotes energy dispersive X-ray.

[29] PNMR denotes proton nuclear magnetic resonance analysis.

[30] COMPASS denotes Condensed-phase Optimized Molecular Potential for Atom Simulation Studies.

[31] POM denotes polarized optical microscopy.
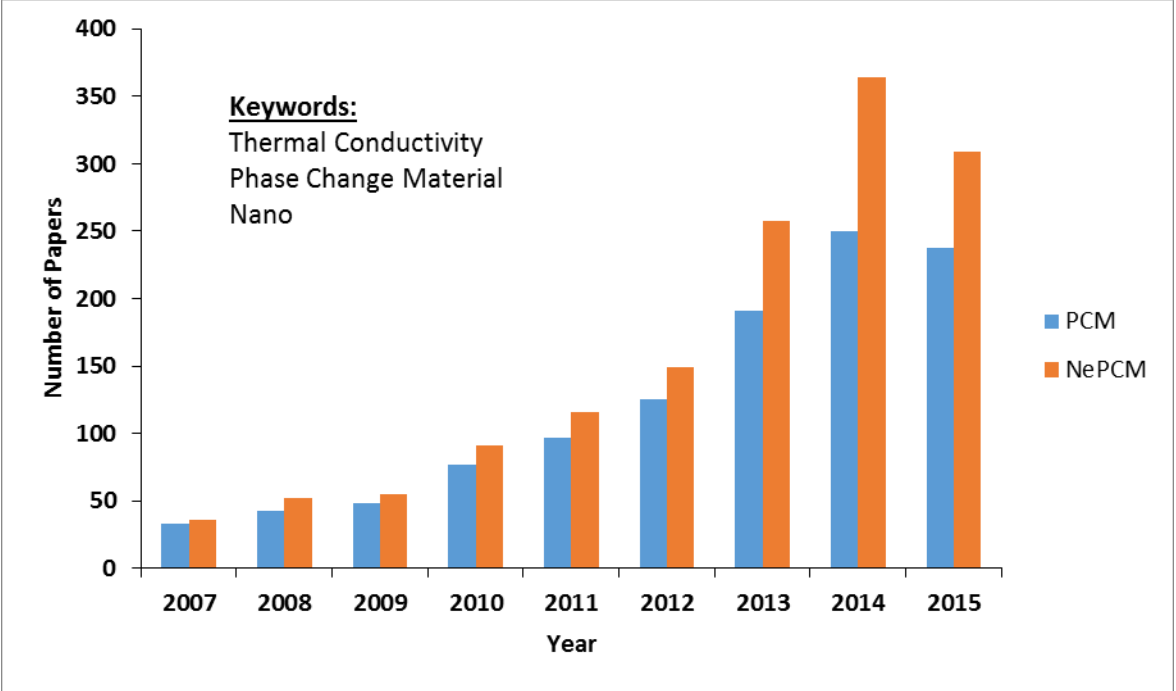
Figure 2.1    Diagram showing the numbers of published PCM and NePCM-related papers since 2007 using the "Science Direct" search engine and the featured keywords in the inset (Search Date: July 1, 2015)
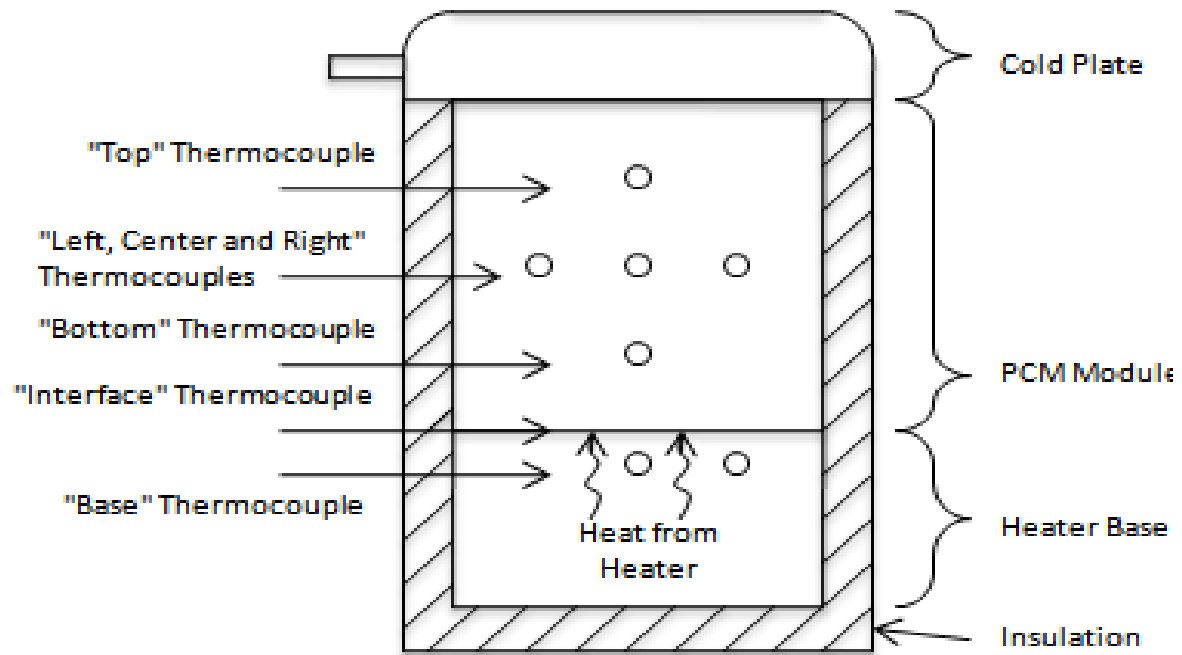
Figure 2.2    Experimental test module for testing PCM composites with thermocouple positioning (Sanusi, Fleischer and Weinstein, 2010)
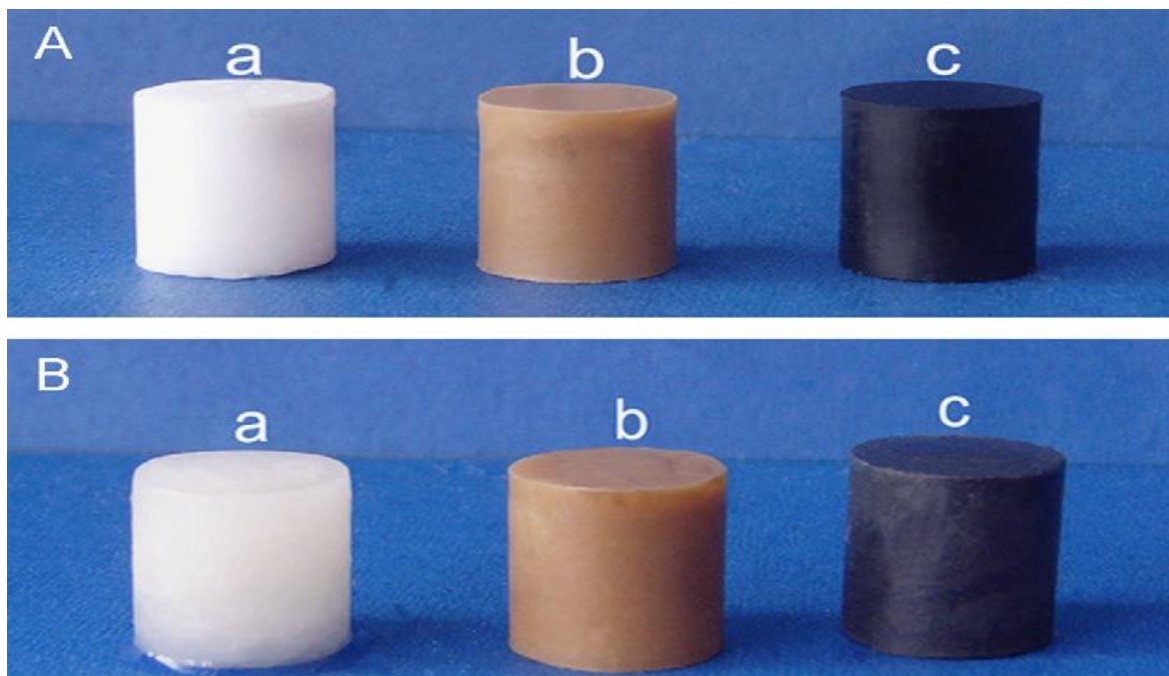
Figure 2.3    Photographs of (a) pure capric acid, (b) CA/HNT composite and (c) CA/HNT/G composite at (A) room temperature and (B) after being heated to 40 $^{\circ}$C (Mei et al., 2011)
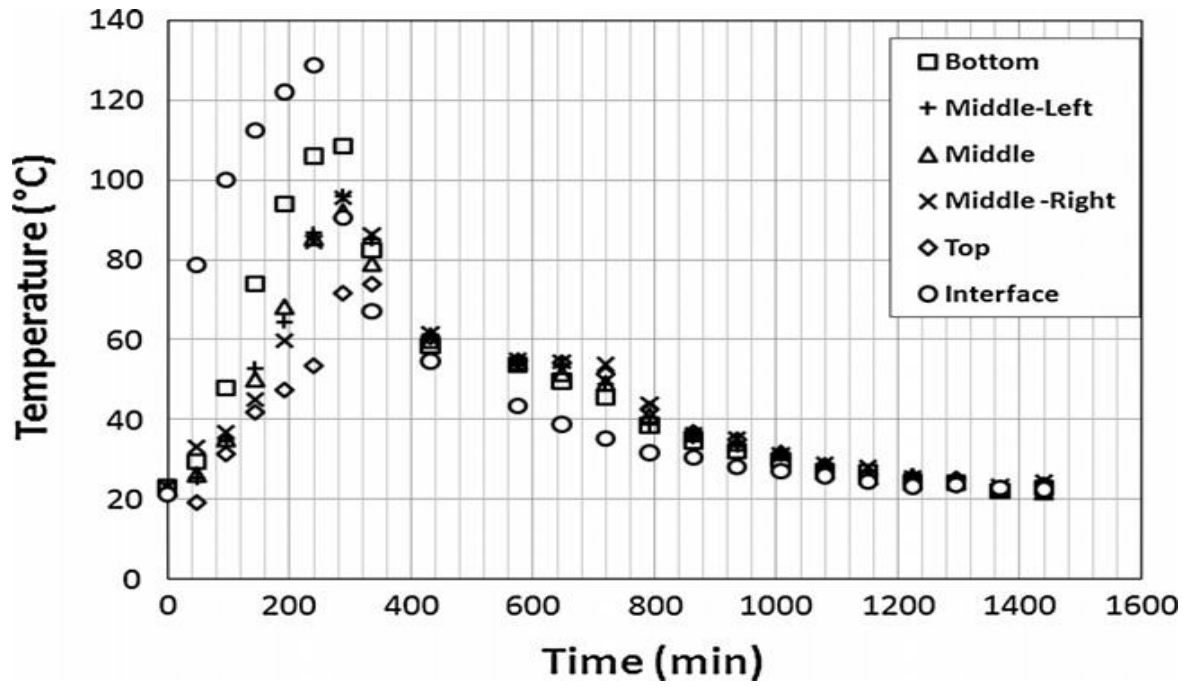
Figure 2.4    Heating curve for the 80/20 composite subjected to a power of 100 W (Ehid and
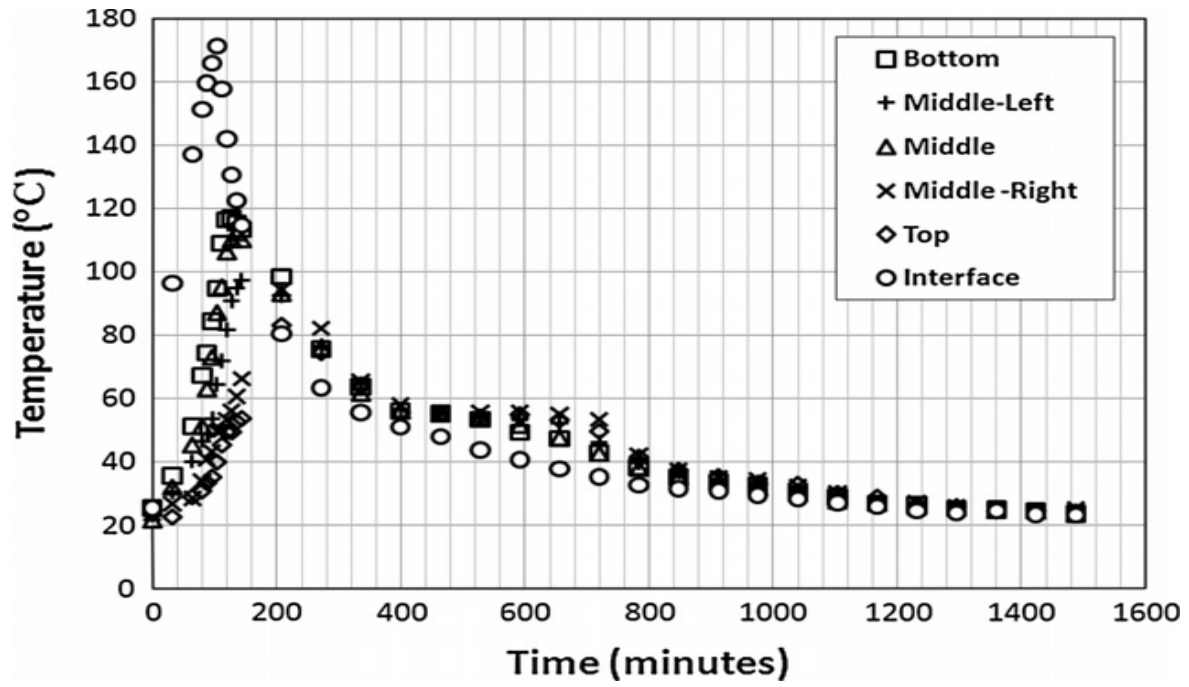
Fleischer, 2012)

Figure 2.5    Heating curve for the 70/30 composite subjected to a power of 100 W (Ehid and

Fleischer, 2012)
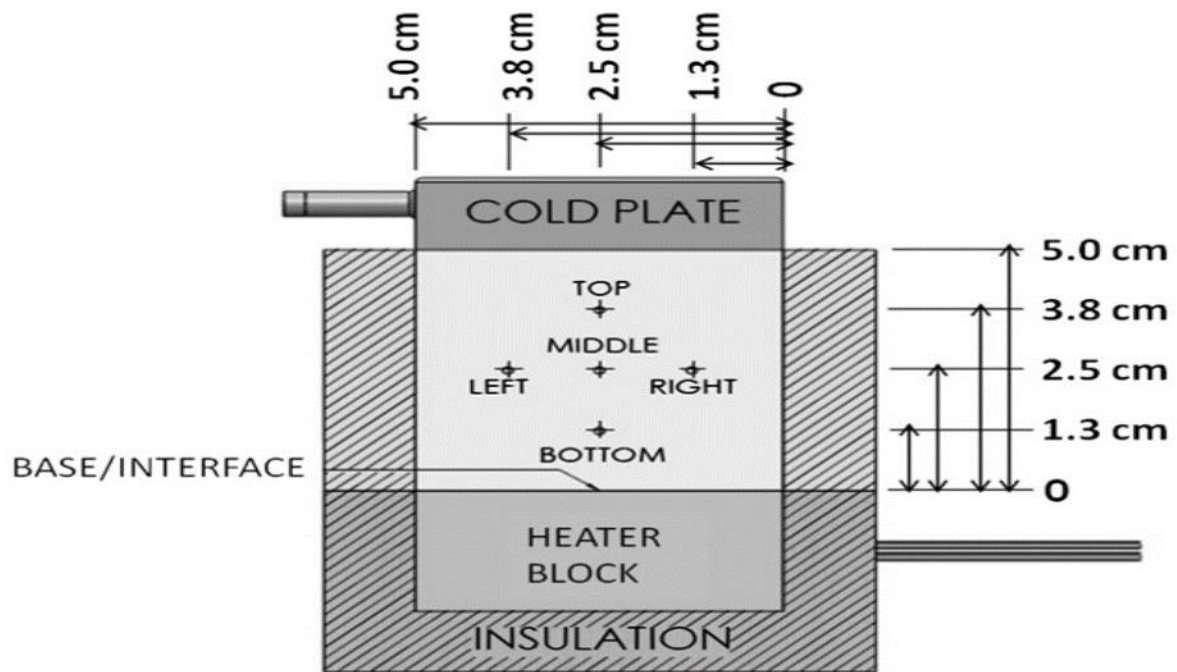
Figure 2.6    Experimental test module for testing PCM composites showing thermocouple positioning, heater block and insulation (Ehid et al., 2012)
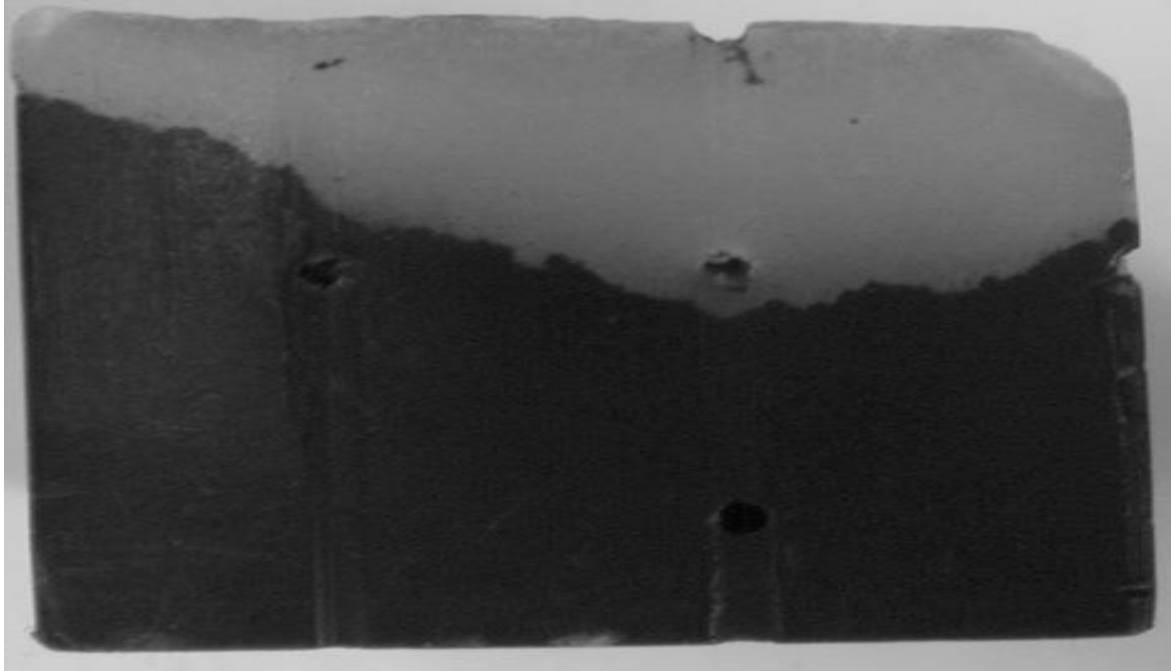
Figure 2.7    Image of the 5 wt% GNF/PCM sample without any added HDPE after 20 thermal

cycles (Ehid et al., 2012)

Figure 2.8    Image of a 5 wt% GNF/PCM sample with 30% added HDPE after 10 thermal

cycles (Ehid et al., 2012)
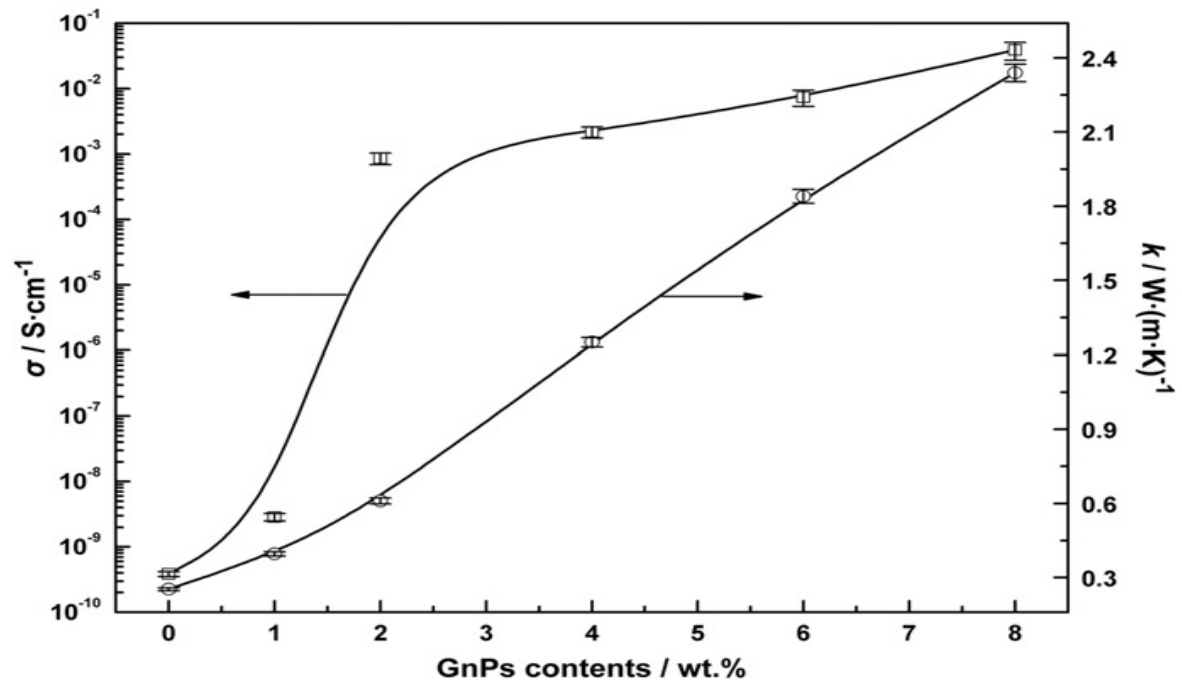
Figure 2.9    Thermal and electrical conductivities of the composite form-stable phase change

materials (FSPCM) as a function of the contents of the graphite nanoplatelets
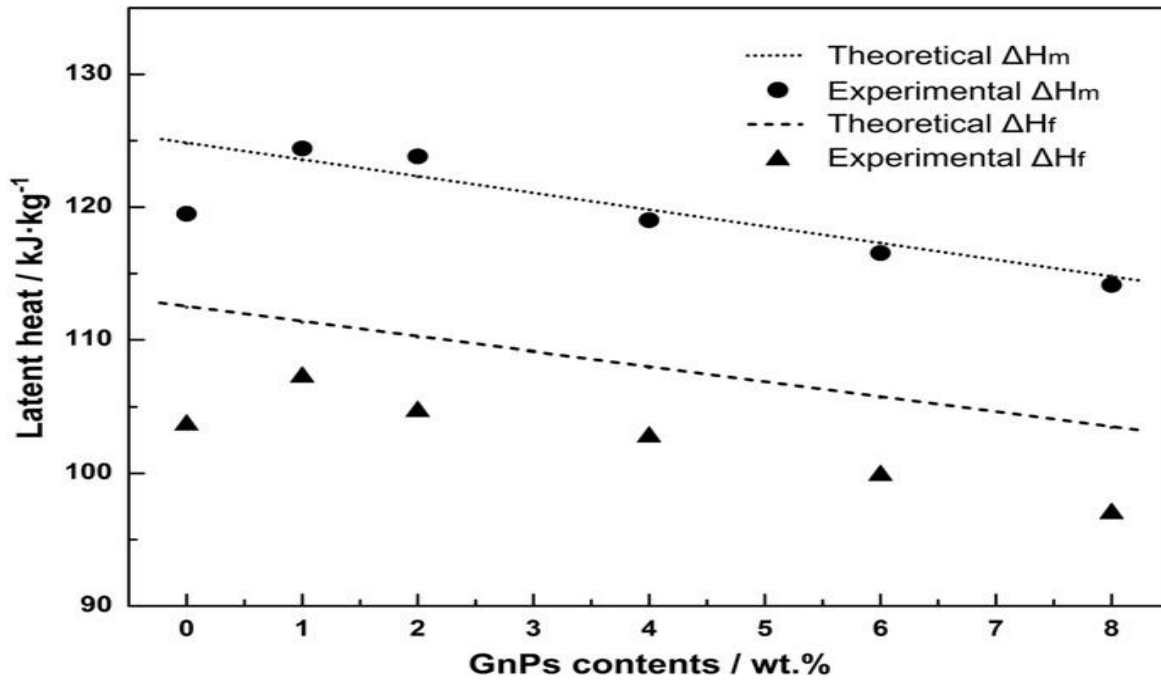
(GnP) (Zhang et al., 2012)

Figure 2.10    Latent heat of melting and freezing of the composite form-stable phase change materials (FSPCM) as a function of the contents of the graphite nanoplatelets (GnP) (Zhang et al., 2012)
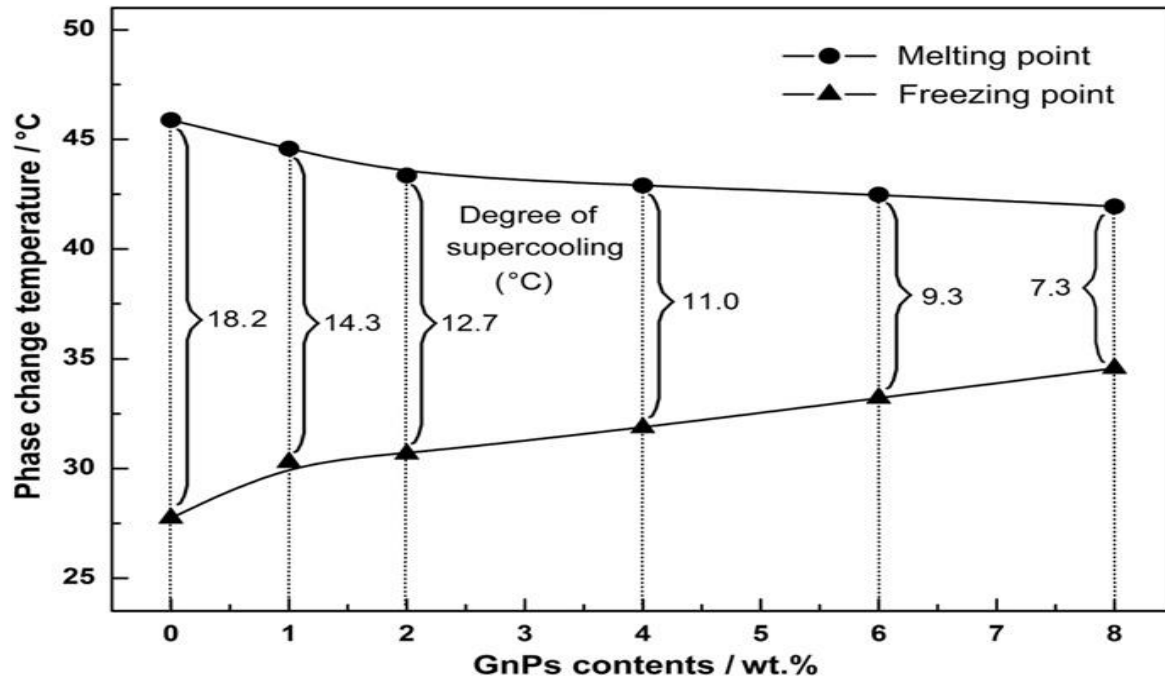
Figure 2.11    Phase change temperature of melting and freezing cycles of the composite form-stable phase change material (FSPCM) as a function of the contents of the graphite nanoplatelets (GnP) (Zhang et al., 2012)
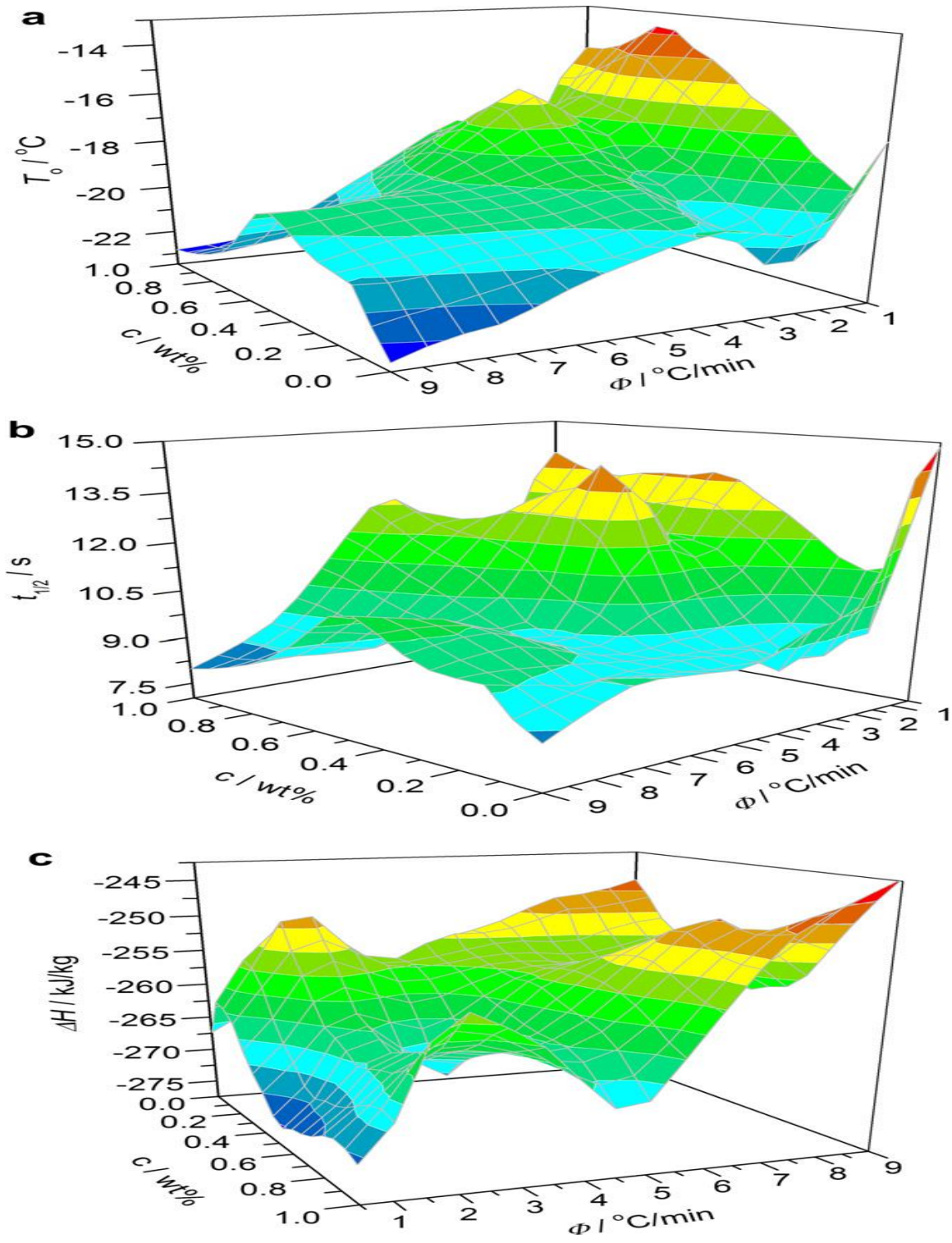
Figure 2.12    3D surface graphs representing the distribution of (a) melting temperature, (b) phase change time and (c) latent heat as a function of the concentration of $TiO_2$ and the cooling rate (Jia et al., 2013)
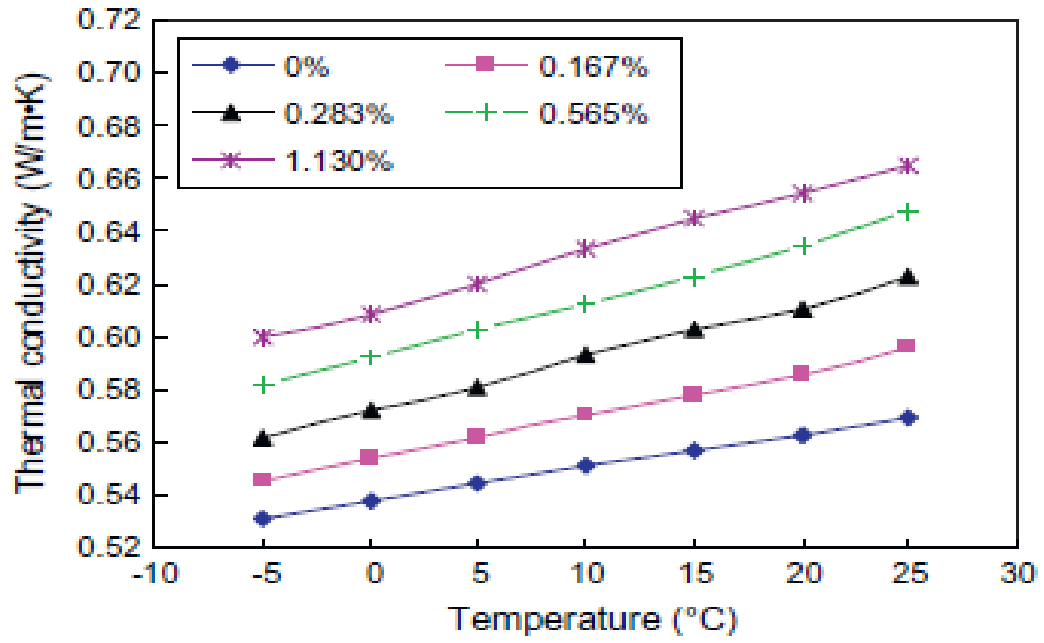
Figure 2.13    Thermal conductivity of the nanofluid for different volume fractions of $TiO_2$

nanoparticles for a range of temperature from -5 $^o$C to 25 $^o$C (He et al., 2012)
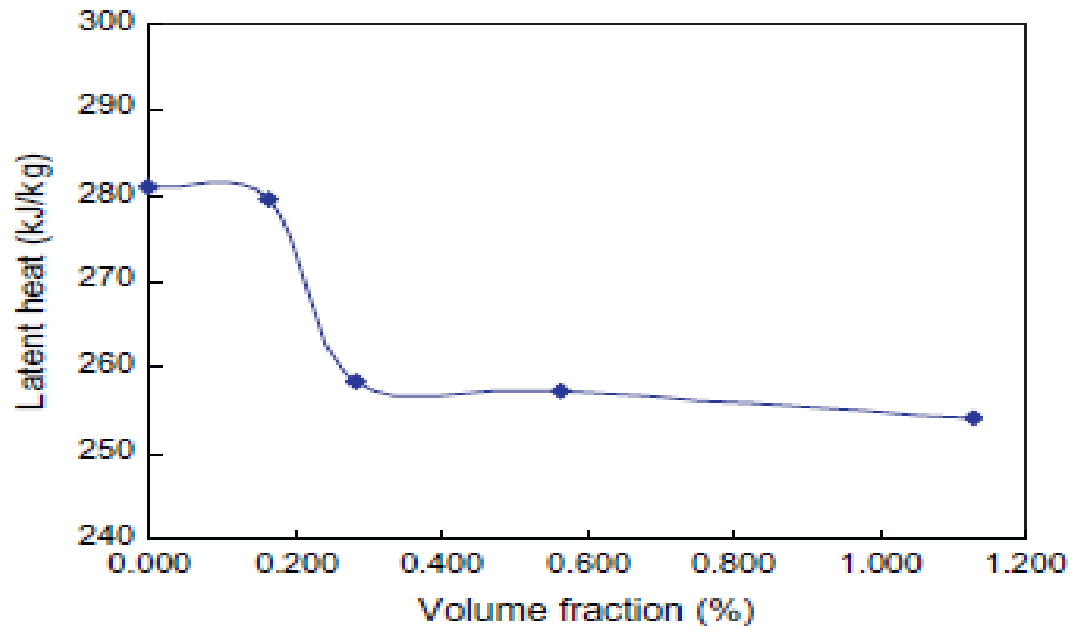
Figure 2.14    Latent heat of the nanofluid $TiO_2$–$BaCl_2$–$H_2O$ for different volume fractions of

$TiO_2$ nanoparticles evaluated using DSC (He et al., 2012)
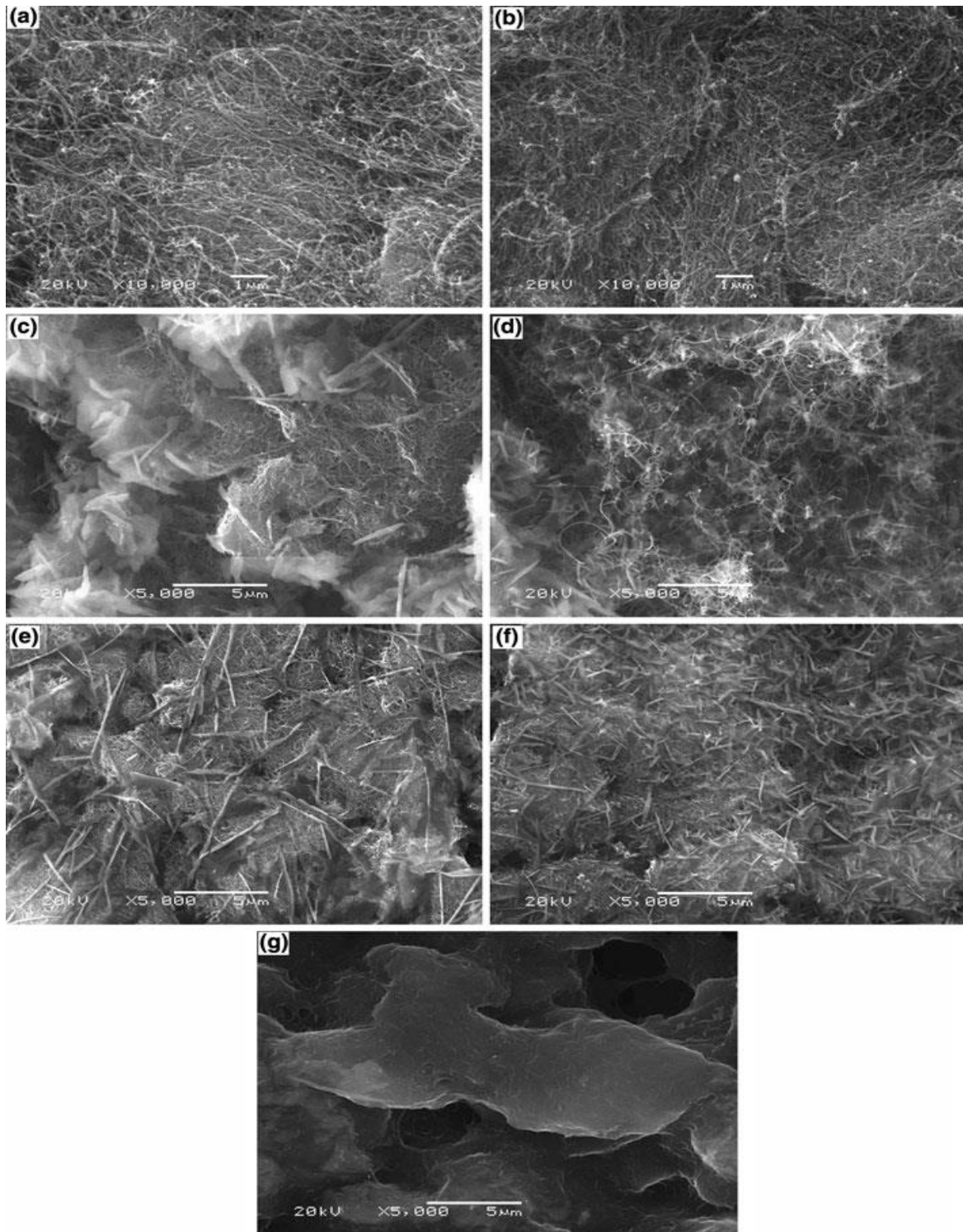
Figure 2.15    SEM images of (a) untreated CNT, (b) oxidized CNT, (c) 50 wt% CNT/fatty

acids, (d) 40 wt% CNT/fatty acids, (e) 30 wt% CNT/fatty acids, (f) 20 wt%

CNT/fatty acids and (g) 10 wt% CNT/fatty acids (Meng et al., 2013)

71
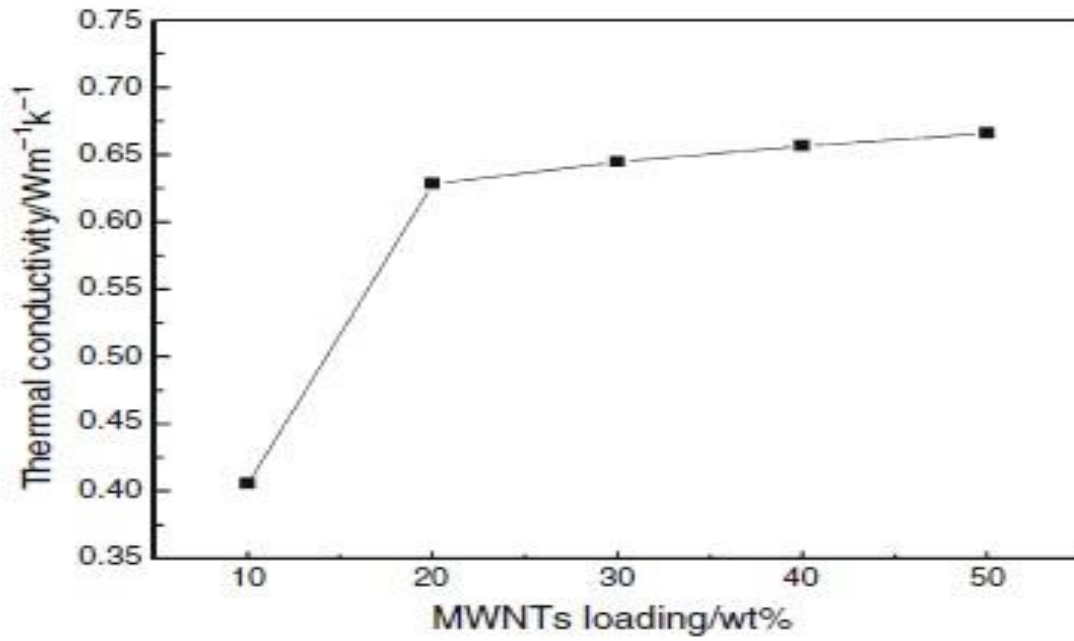
Figure 2.16    Thermal conductivity values of the composite fatty acids/CNT as a function of the

loading of carbon nanotubes (Meng et al., 2013)
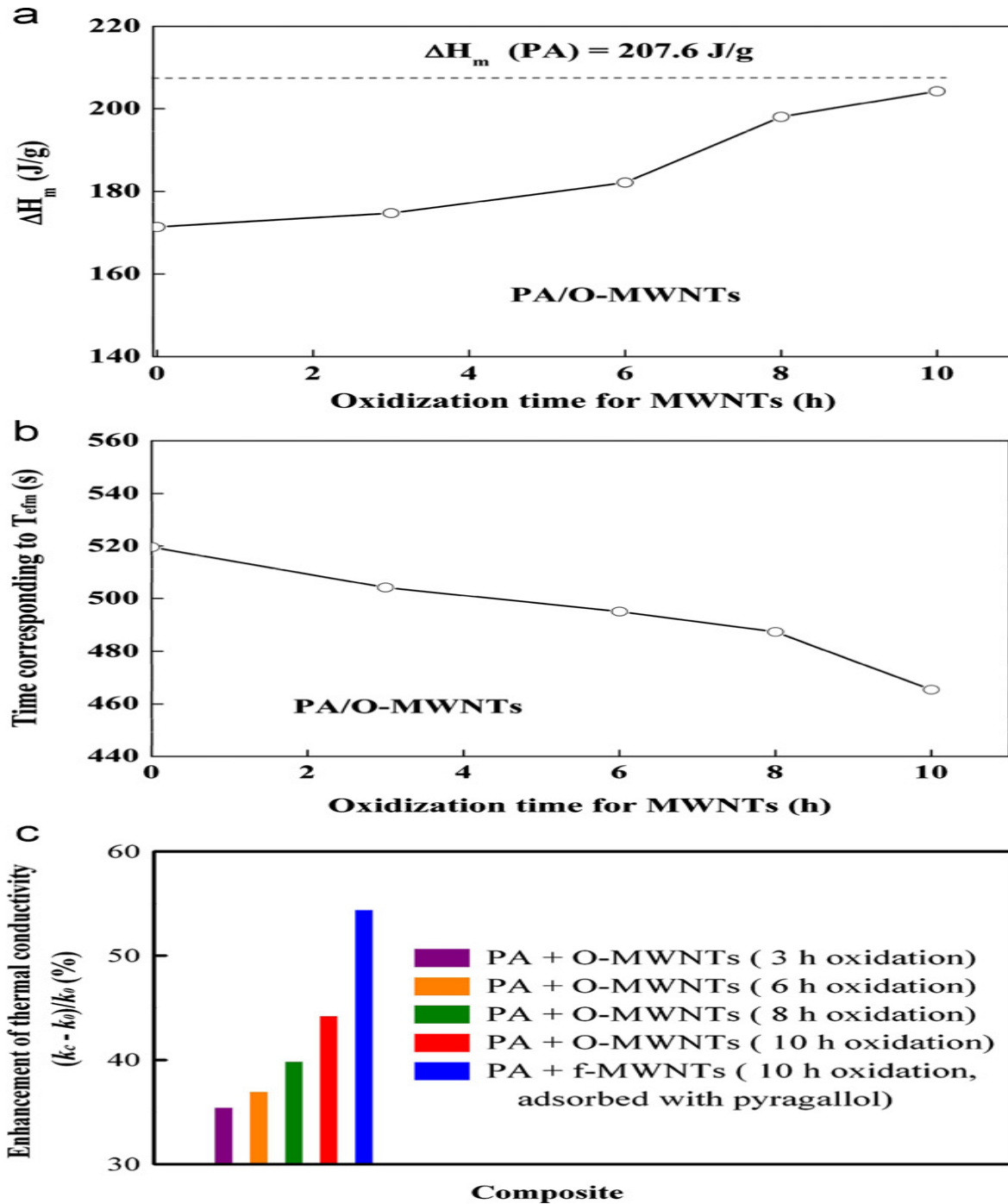
Figure 2.17    (a) Latent heat of melting, (b) The time corresponding to melting temperature as a

function of the various oxidation time of the O-MWNT and (c) Enhancement of

the thermal conductivity of Palmitic Acid for the various composites of O-

MWNT and f-MWNT (Ji et al., 2012)
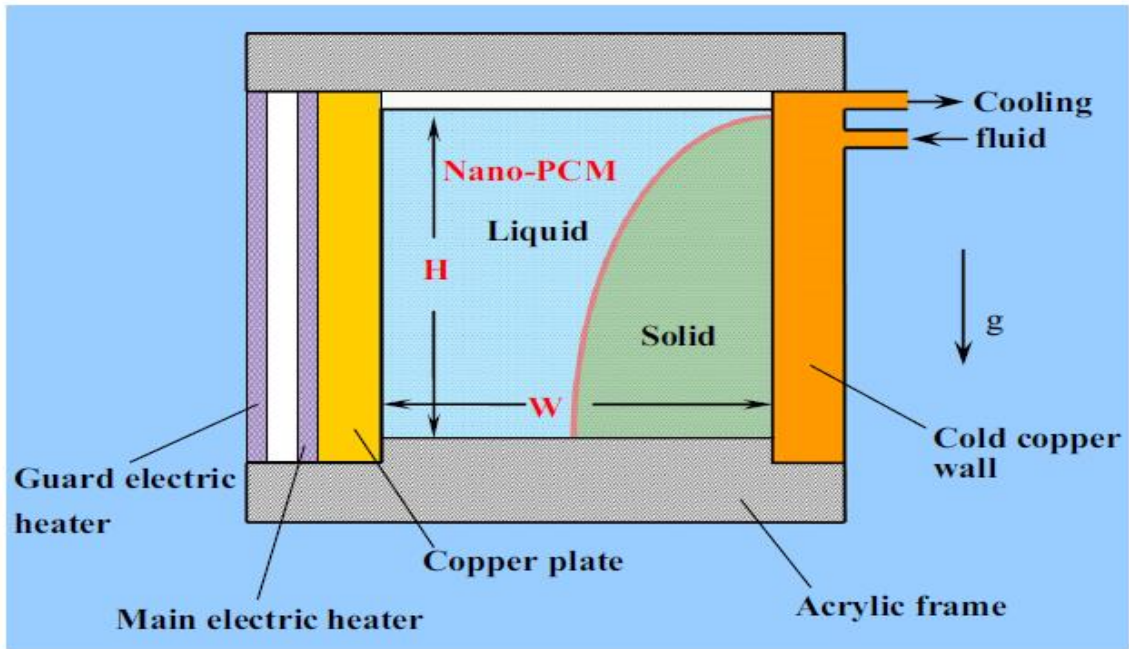
Figure 2.18    A diagram of the experimental test module for testing PCM composites (Ho and

Gao, 2013)
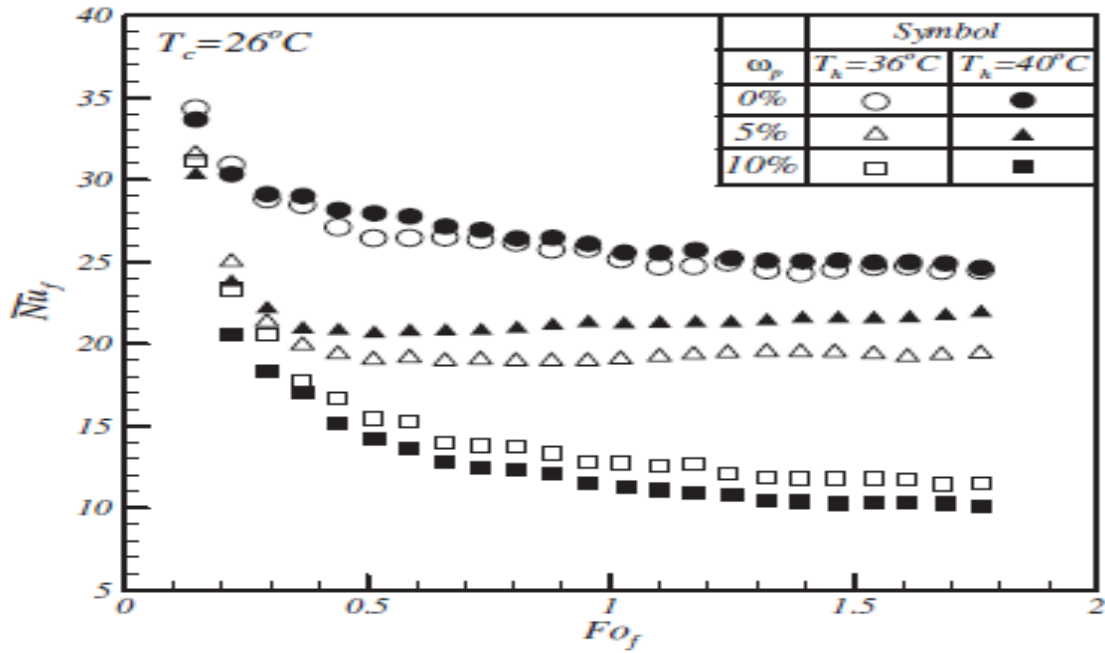
Figure 2.19    Effect of the variation of the hot wall temperature on the Nusselt number for different mass factions of alumina nanoparticles while maintaining the cold wall at a uniform temperature (Ho and Gao, 2013)
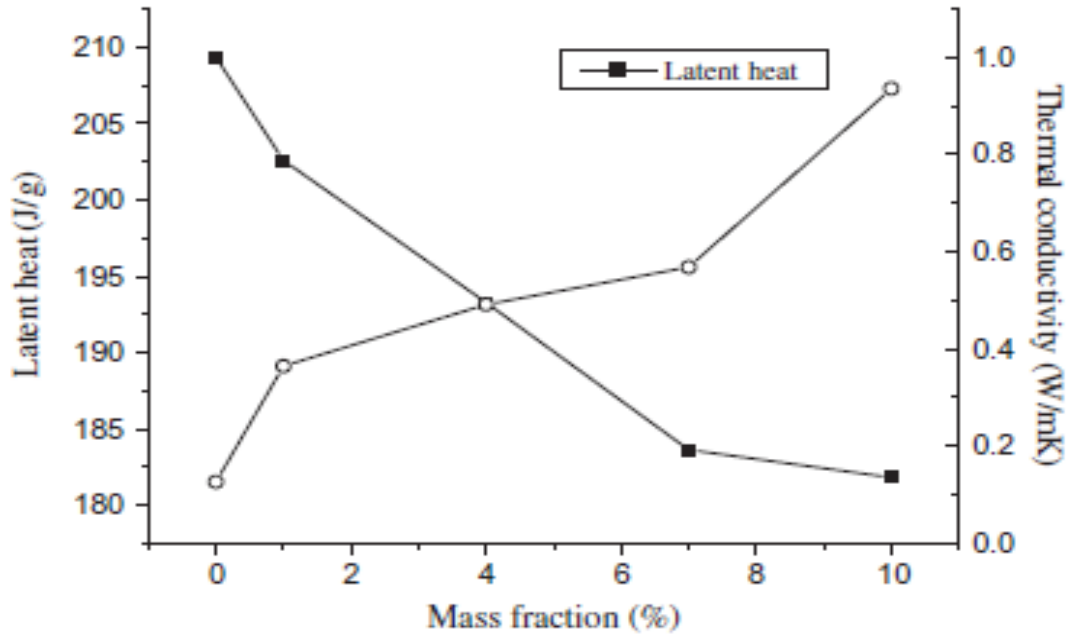
Figure 2.20    Experimental values of the latent heat and thermal conductivity of the NG/paraffin composite as a function of the mass fraction of nano-graphite (Li, 2013)
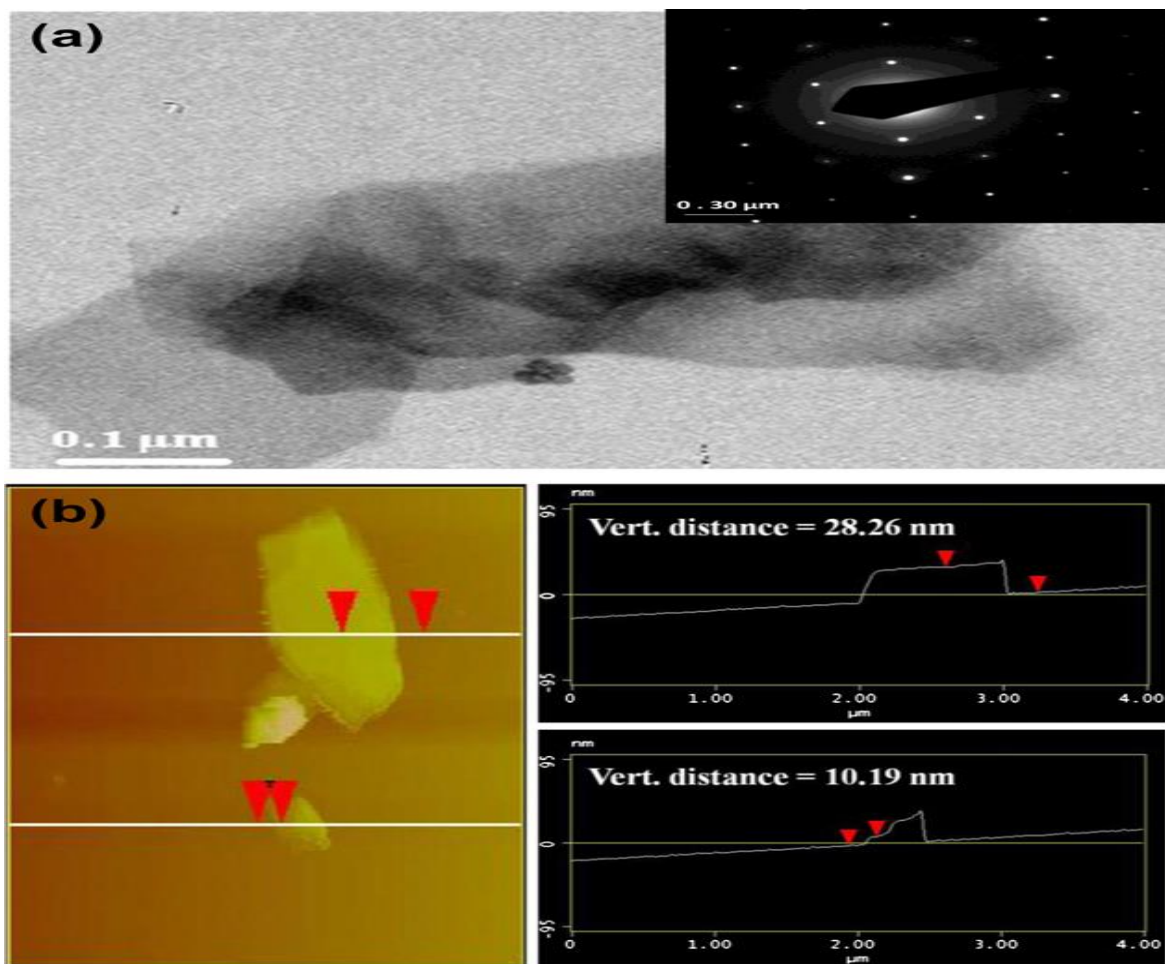
Figure 2.21    (a) TEM image of graphite nanosheets and (b) AFM image and depth profiles of

graphite nanosheets (Chen et al., 2013)
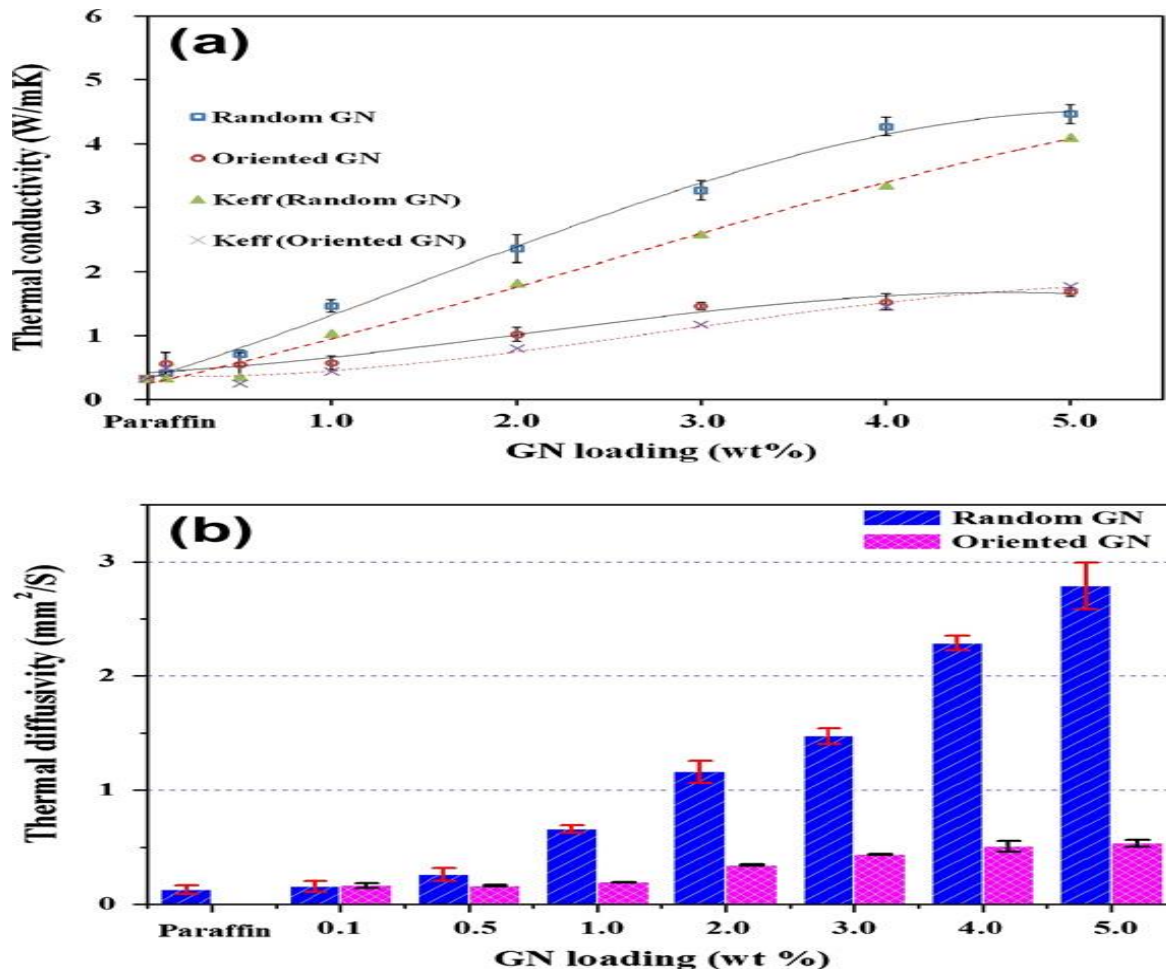
Figure 2.22    (a) Thermal conductivity and (b) thermal diffusivity of the R-GN/paraffin and the O-GN/paraffin composites filled with various mass fractions of graphite nanosheets (Chen et al., 2013)
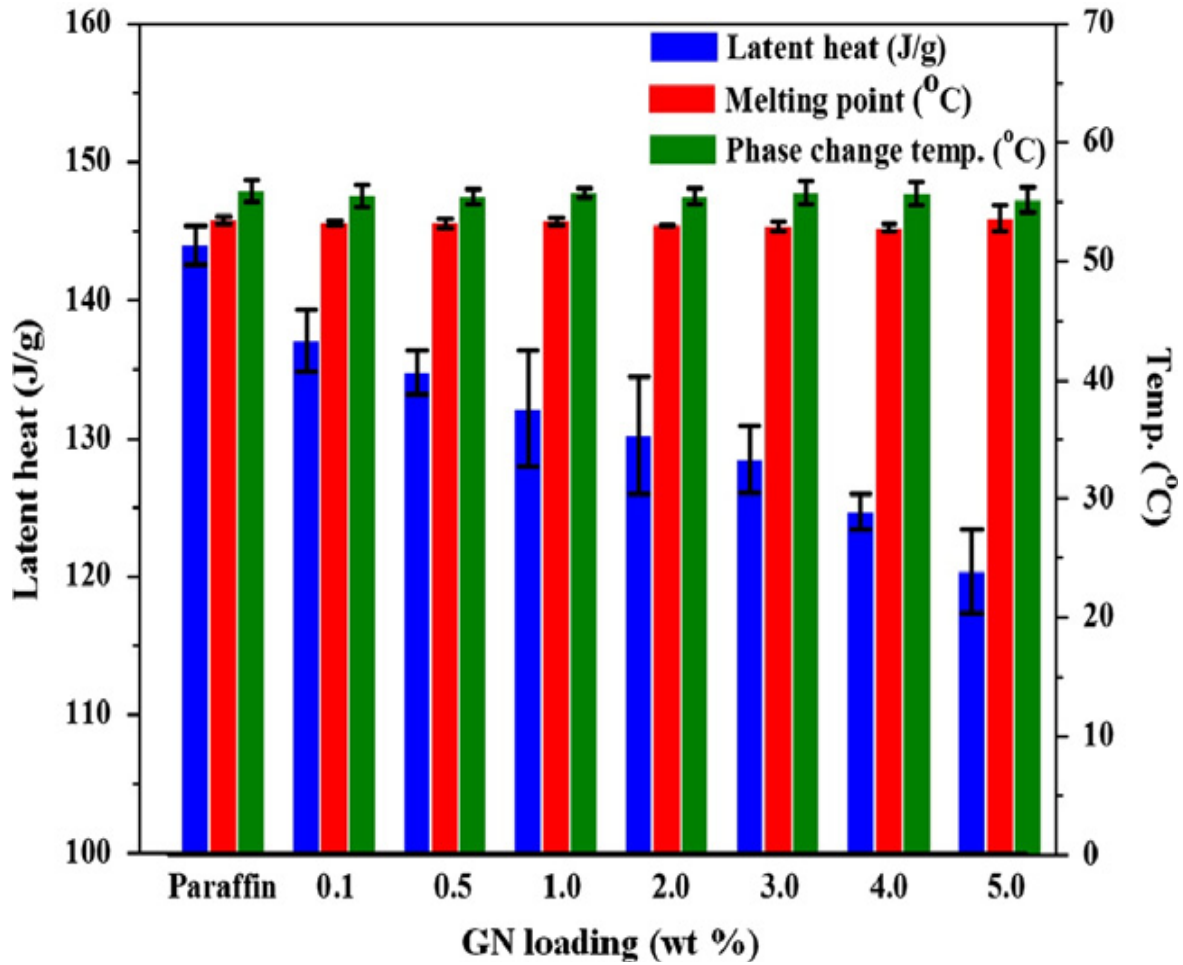
Figure 2.23　Thermal properties (melting point, phase transition temperature, and latent heat) of the R-GN/paraffin composites evaluated using Differential Scanning Calorimetry (Chen et al., 2013)
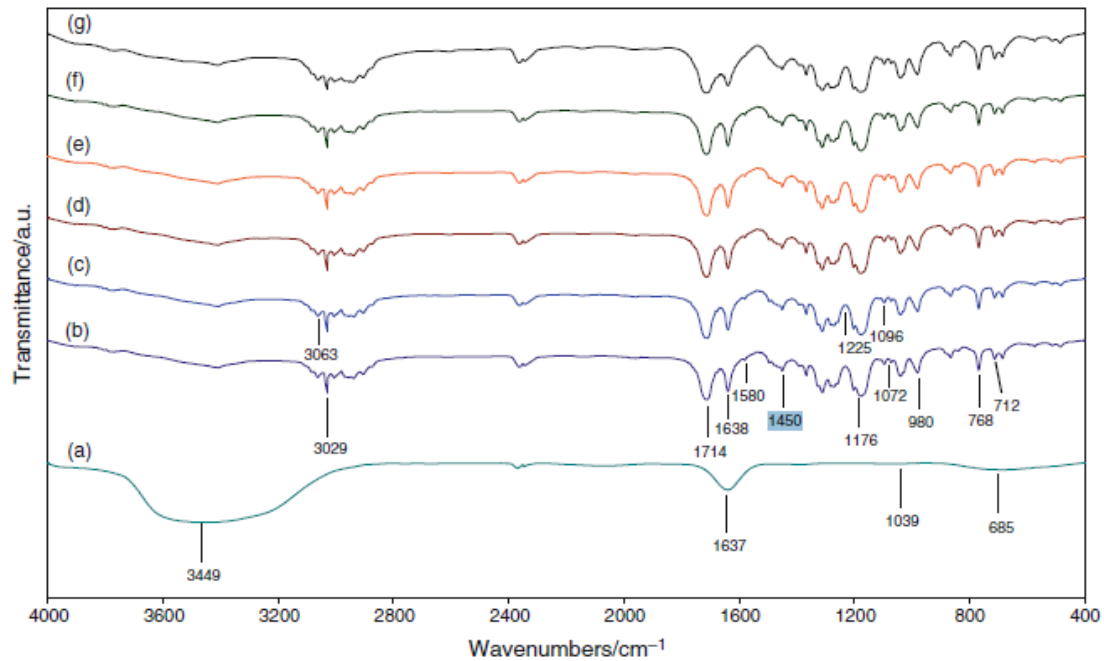
Figure 2.24     FTIR curves of (a) base EC, (b) 0.1 wt% AgNP, (c) 0.5 wt% AgNP, (d) 1.0 wt%

AgNP, (e) 2.0 wt% AgNP and (f) 5.0 wt% AgNP, with all loadings dispersed in

base PCM (Parameshwaran, Jayavel and Kalaiselvam, 2013)
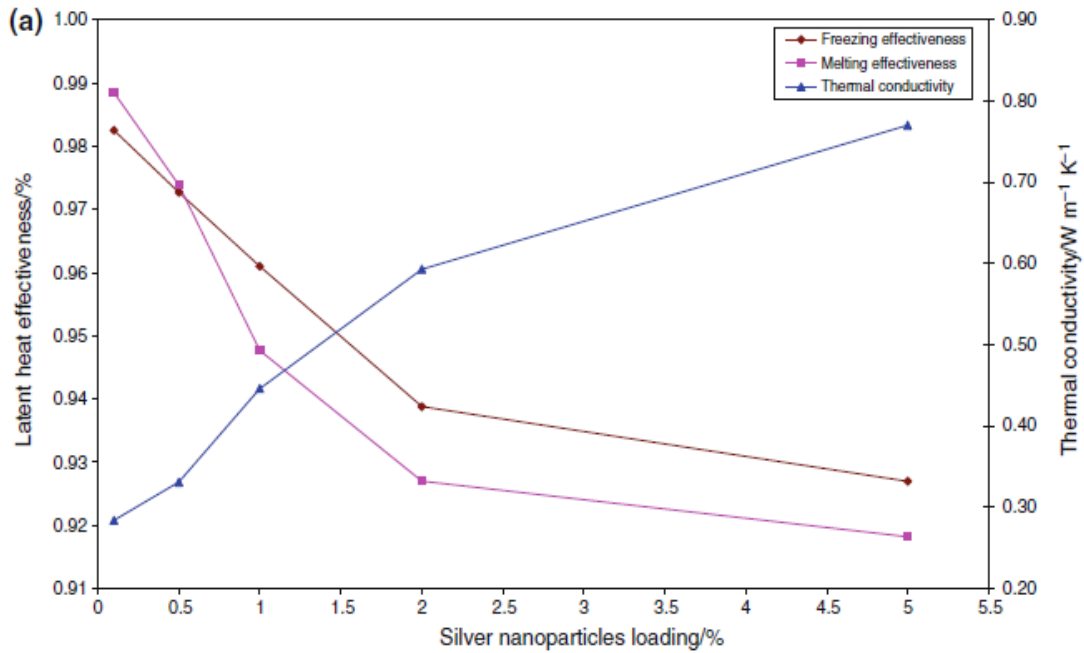
Figure 2.25    Latent heat effectiveness and thermal conductivity of SNOE PCM as a function of the loading of silver nanoparticles (AgNP) (Parameshwaran, Jayavel and Kalaiselvam, 2013)
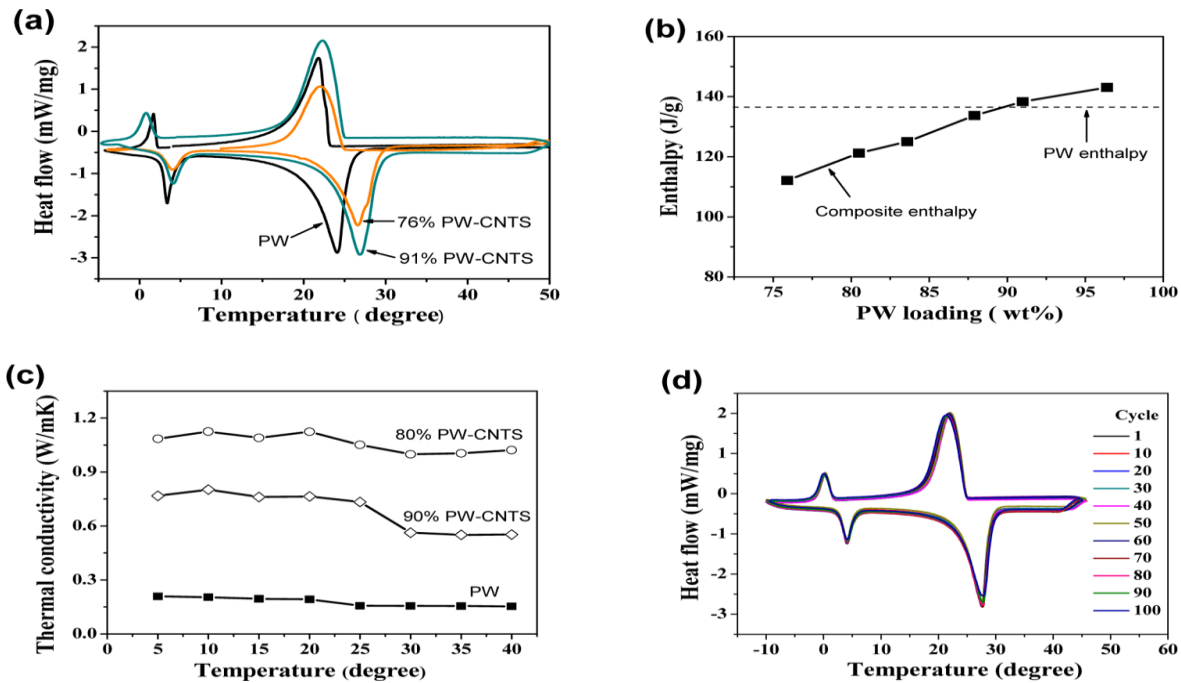
Figure 2.26    (a) DSC curves of pure PW and PW-CNT composites with PW loading of 76% and 91%, respectively, (b) Measured phase change enthalpy of PW-CNT composites with different mass fraction of paraffin wax compared to the pure paraffin wax (dashed line: 136 kJ/kg), (c) Thermal conductivities of pure PW and PW composites with PW loading of 80% and 90%, respectively, recorded for a temperature range of 5 to 40 °C using THW and (d) DSC curves of a 90.5 wt% PW-CNT composite tested for 100 cycles, showing minimal changes during the heating and cooling processes (Chen et al., 2012)
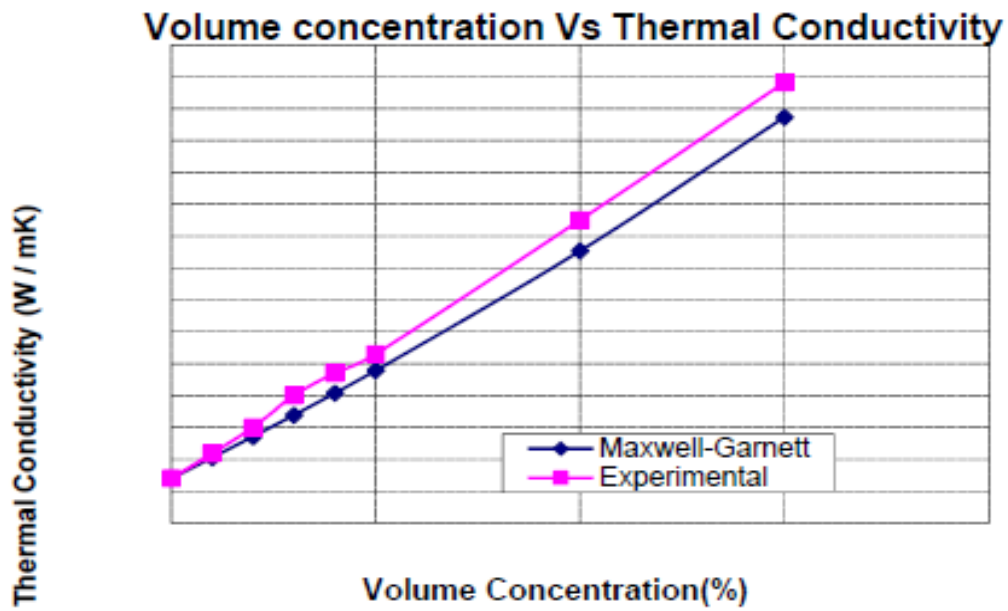
Figure 2.27    Experimental and Maxwell-Garnett model predictions of thermal conductivity of the PCM composites as a function of the volume concentration of CuO nanoparticles (Karunamurthy et al., 2012)
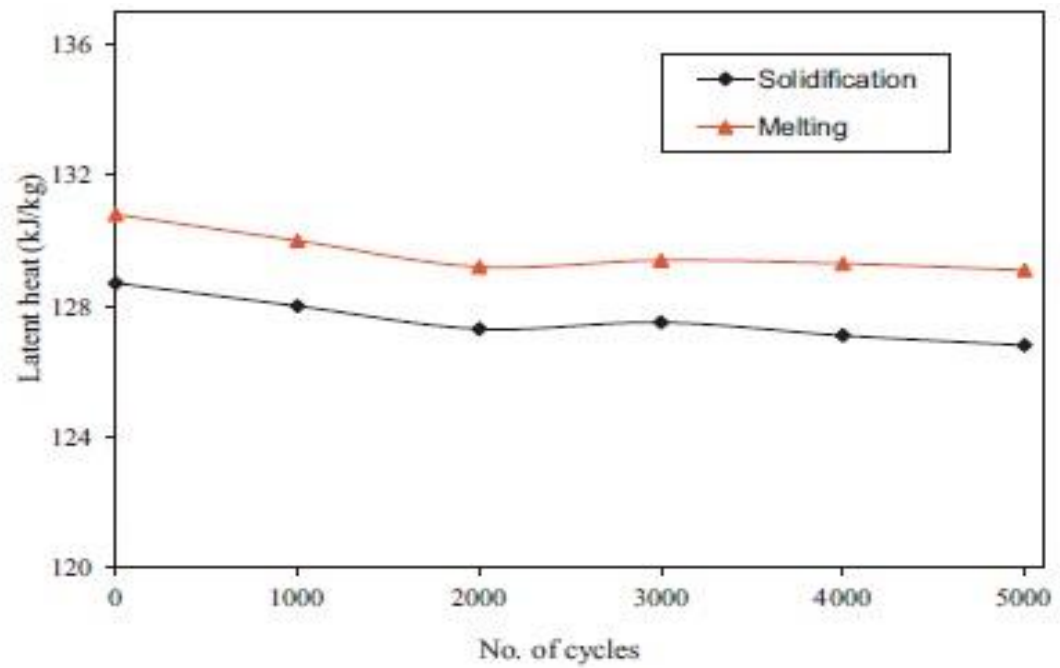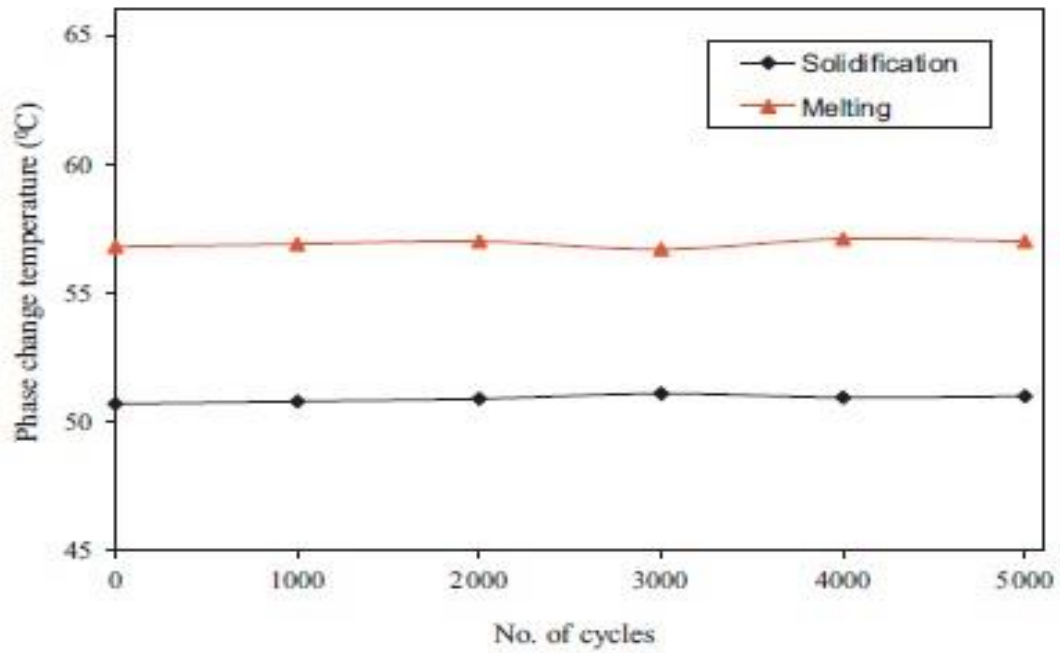
Figure 2.28    Phase change temperature and latent heat values of stearic acid based TiO$_2$ nanofluid as a function of the number of freezing and melting cycles (Harikrishnan et al., 2013)
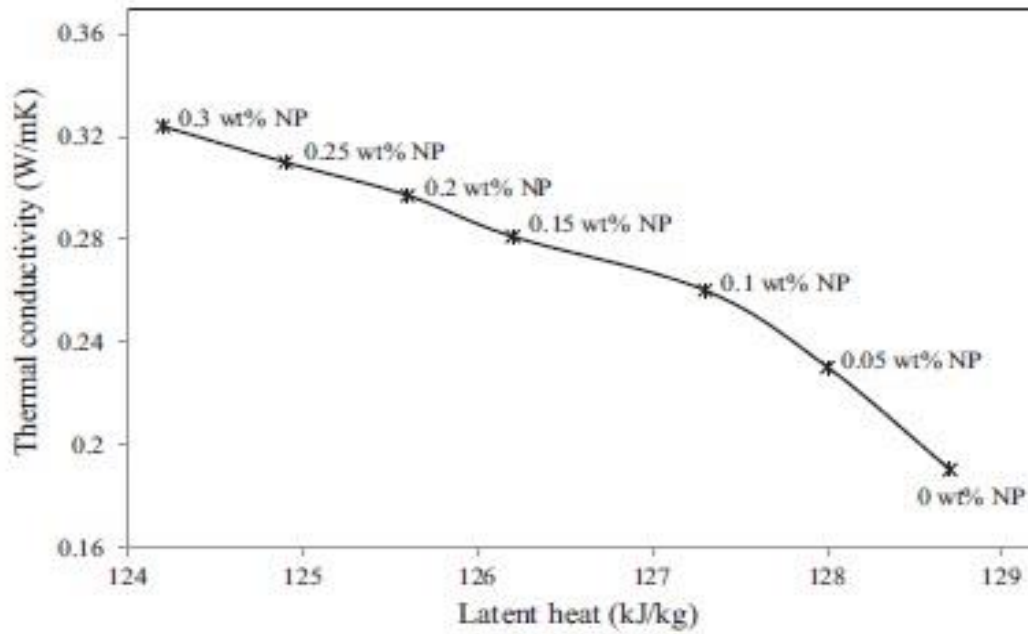
Figure 2.29    Thermal conductivity and latent heat values of stearic acid based TiO$_2$ nanofluid

for the various mass fractions of TiO$_2$ nanoparticles (Harikrishnan et al., 2013)
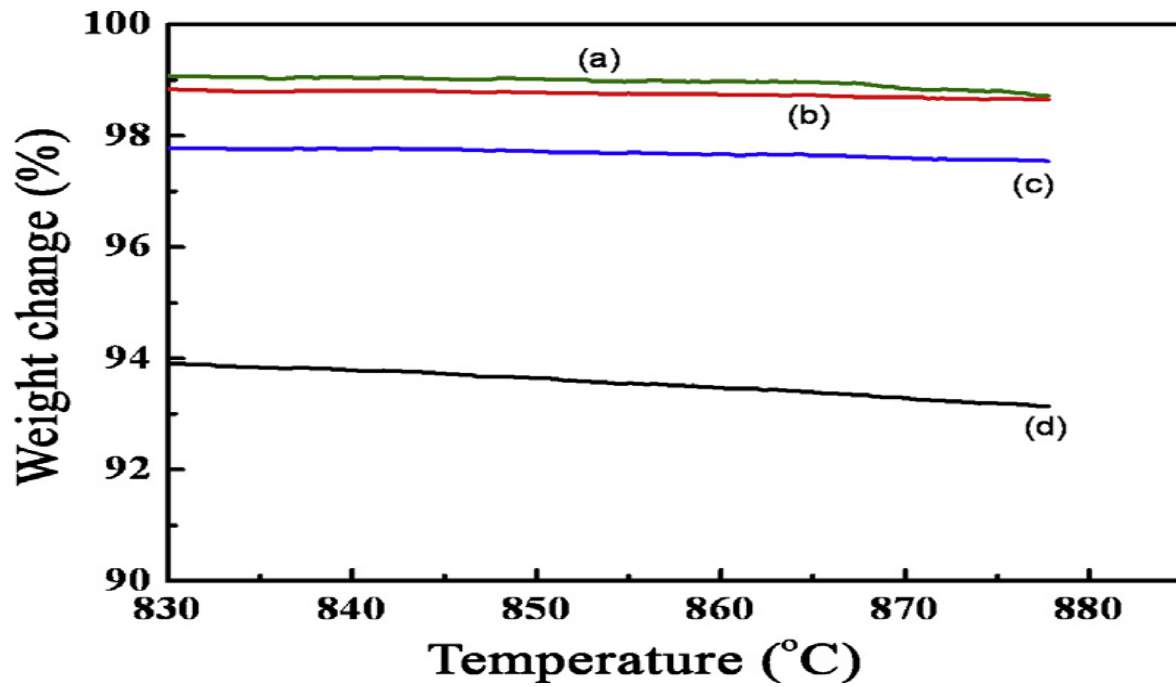
Figure 2.30    Thermal gravity analyses (TGA) of $Na_2CO_3$/MgO composite PCM at different

weight ratios of (a) 40:60, (b) 50:50, (c) 60:40 and (d) 80:20 (Ye et al., 2014)
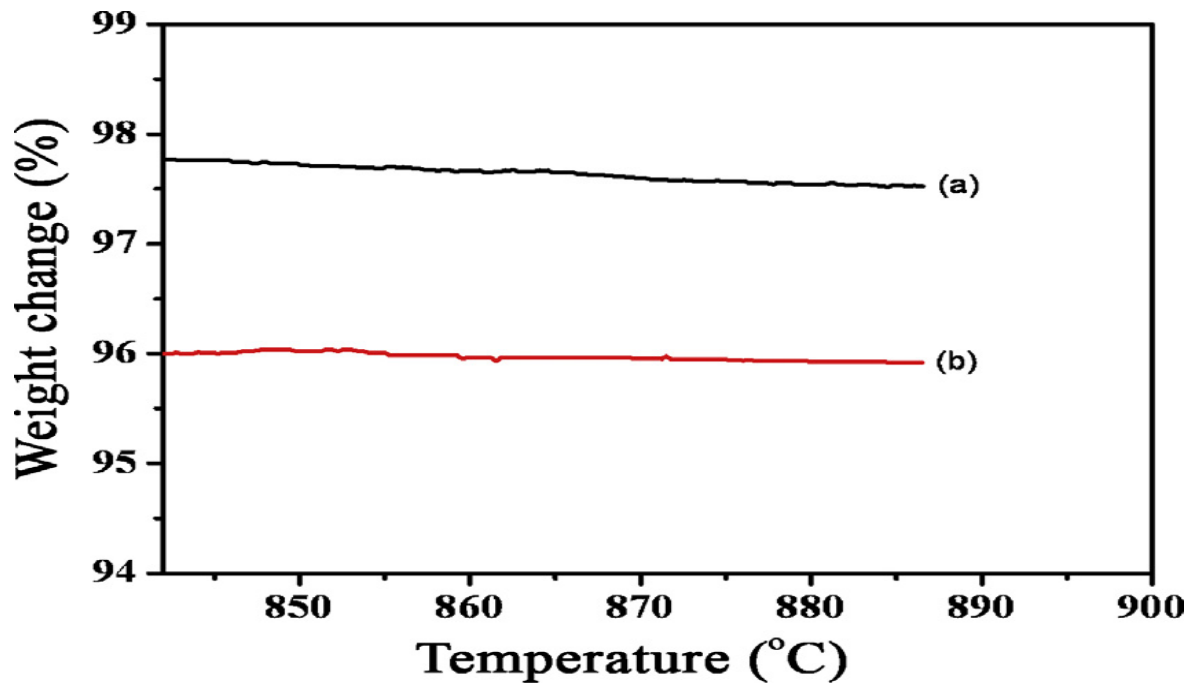
Figure 2.31    Thermal gravity analyses of 60:40 weight ratio of $Na_2CO_3$/MgO composite PCM

(a) with 0.5 wt% MWNT and (b) without MWCNT (Ye et al., 2014)
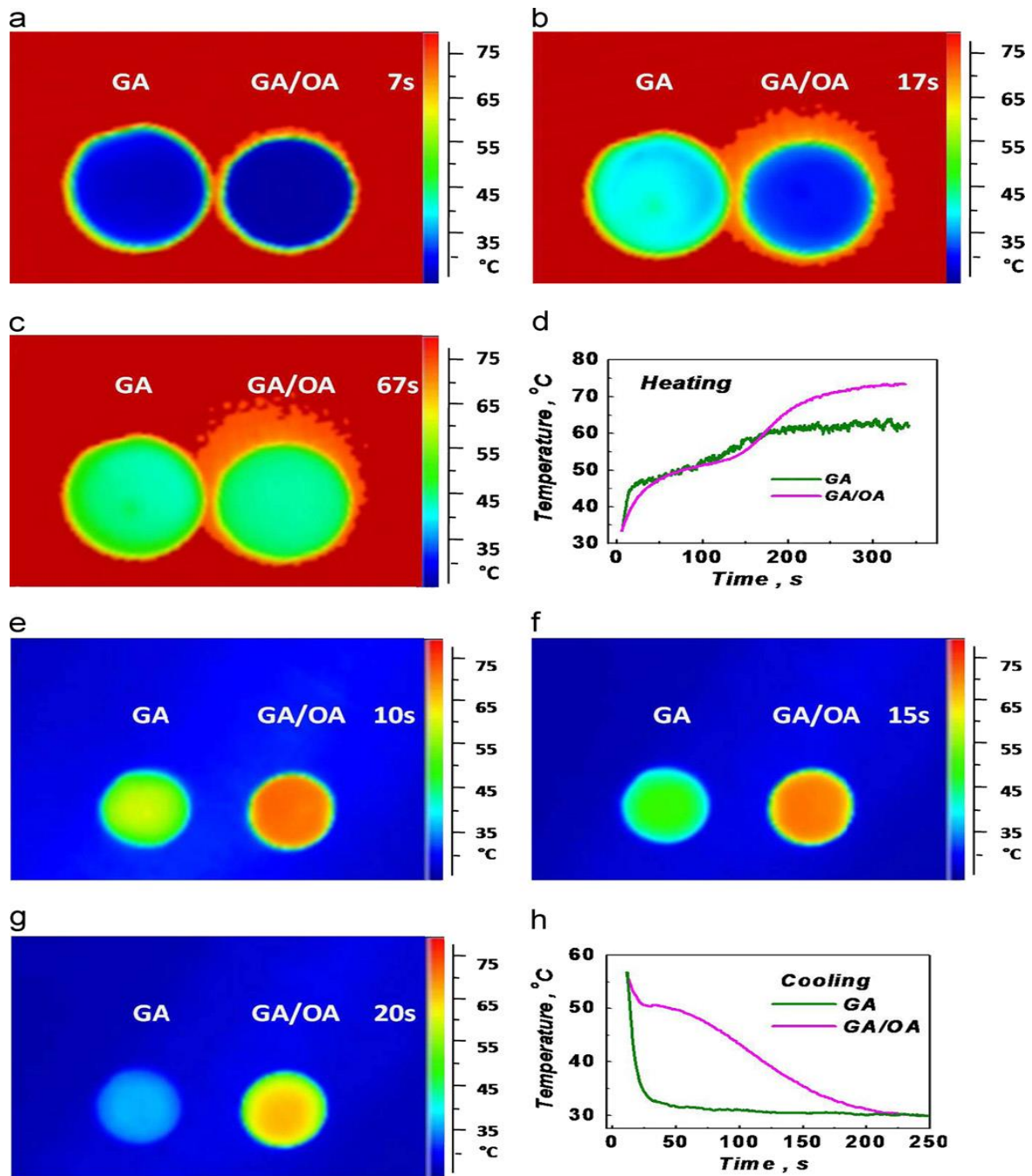
Figure 2.32    (a–c) Thermal images of the GA and GA/OA samples during the heating cycle for three different intervals (7, 17 and 67 s), (d) Transient heating response of GA and GA/OA composites, (e–g) Thermal images of the GA and GA/OA samples during the cooling cycle for three different intervals (10, 15 and 20 s) and (h) Transient cooling response of GA and GA/OA composites (Zhong et al., 2013)
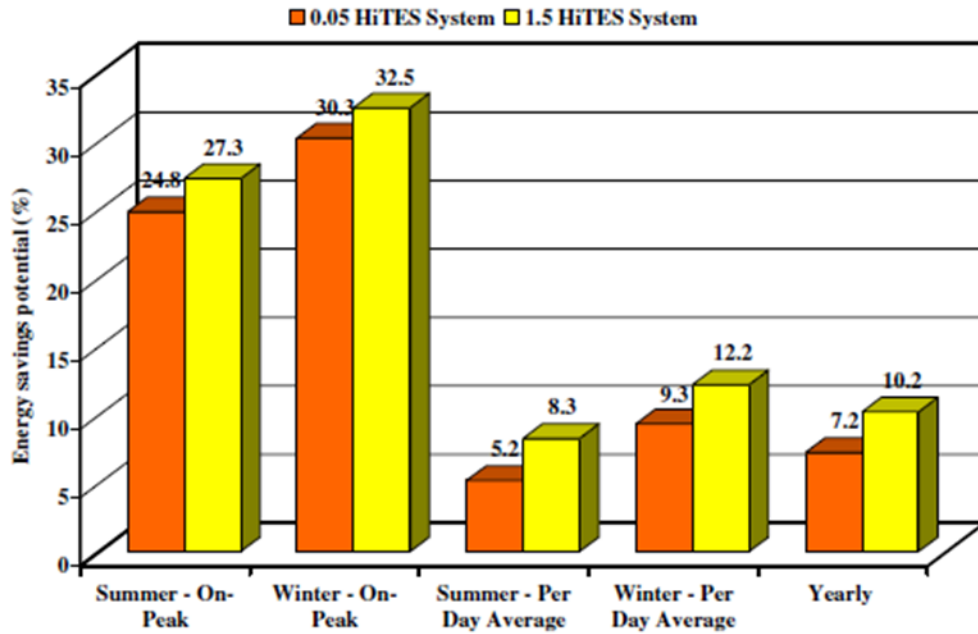
Figure 2.33    Potential energy savings of the 0.05 and 1.5 hybrid nanocomposites-based cool

thermal energy storage system (Parameshwaran and Kalaiselvam, 2013)
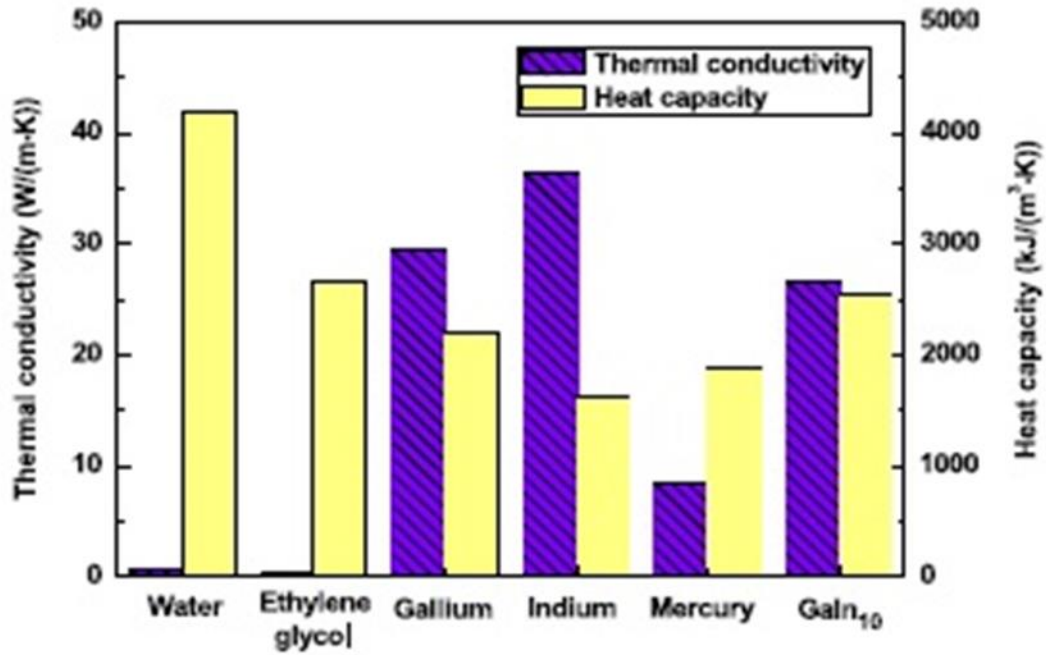
Figure 2.34   Thermal conductivity and heat capacity, per unit volume, of typical liquid metals

and conventional base fluids (Zhang and Liu, 2013)
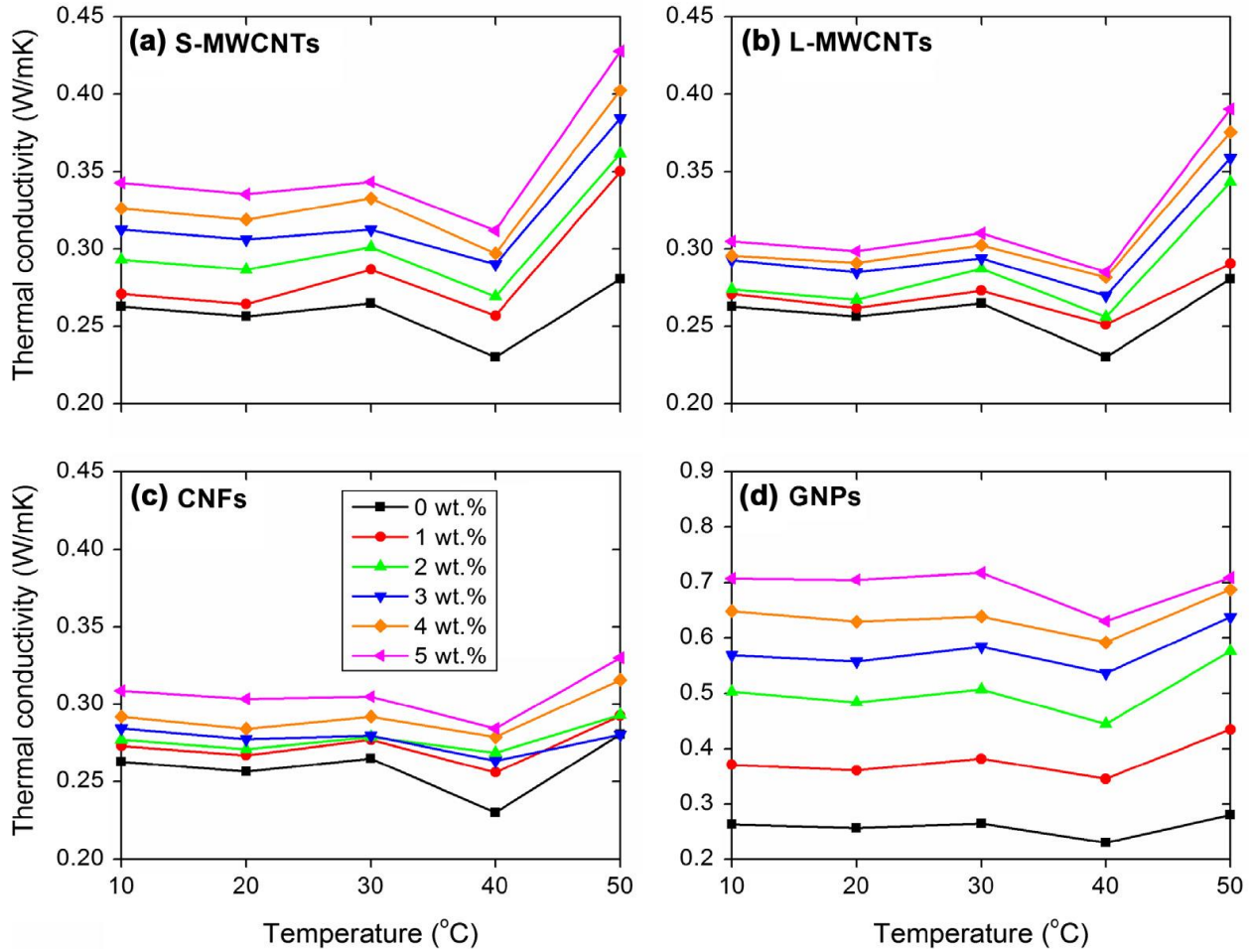
Figure 2.35     Thermal conductivity measurements of the carbon nanofillers-enhanced PCM as a function of temperature, for the four types of nanomaterials (a) S-MWCNT, (b) L-MWCNT, (c) CNF and (d) GNP (Fan et al., 2013)
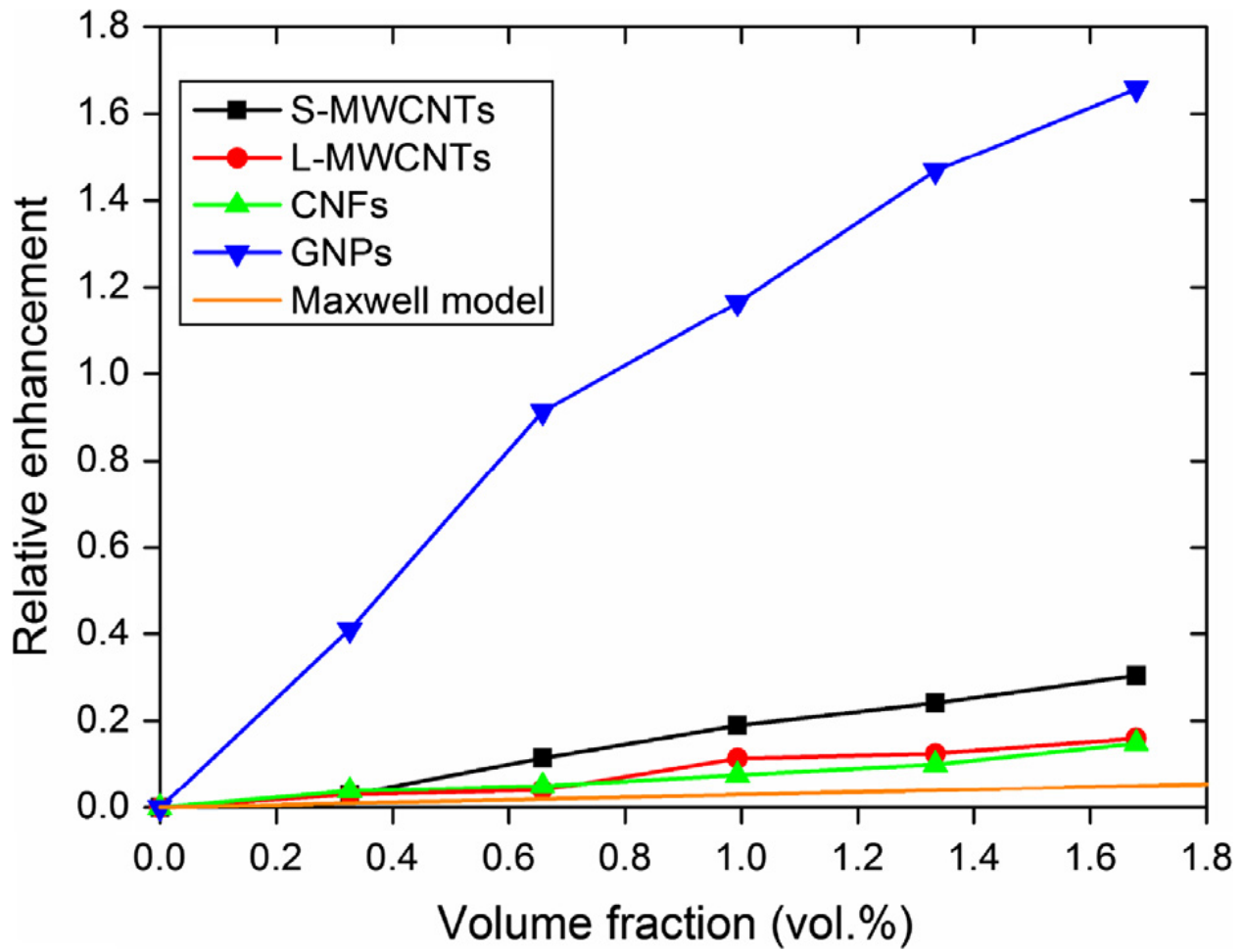
Figure 2.36    Thermal conductivity enhancement of the carbon nanofillers-enhanced PCM as a

function of the volume fraction of the nanomaterials (Fan et al., 2013)
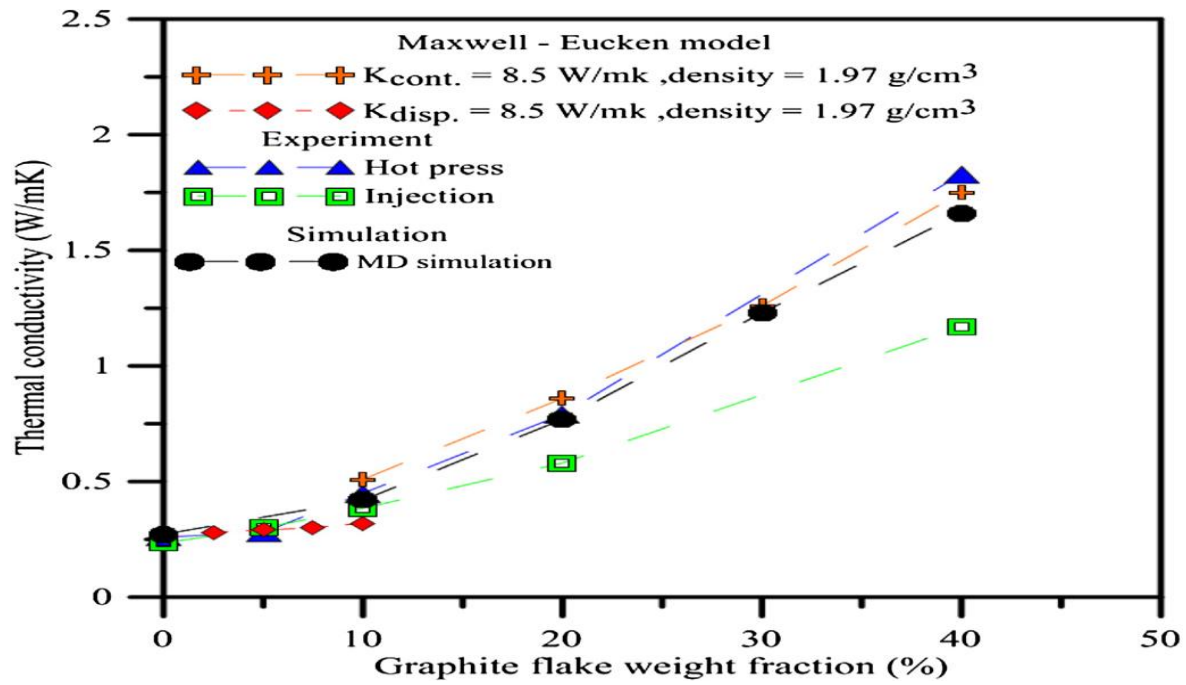
Figure 2.37    Thermal conductivity of pure PPS and GF/PPS composites from experimental methods, NEMD simulation and prediction of the Maxwell-Eucken model (Ju et al., 2013)
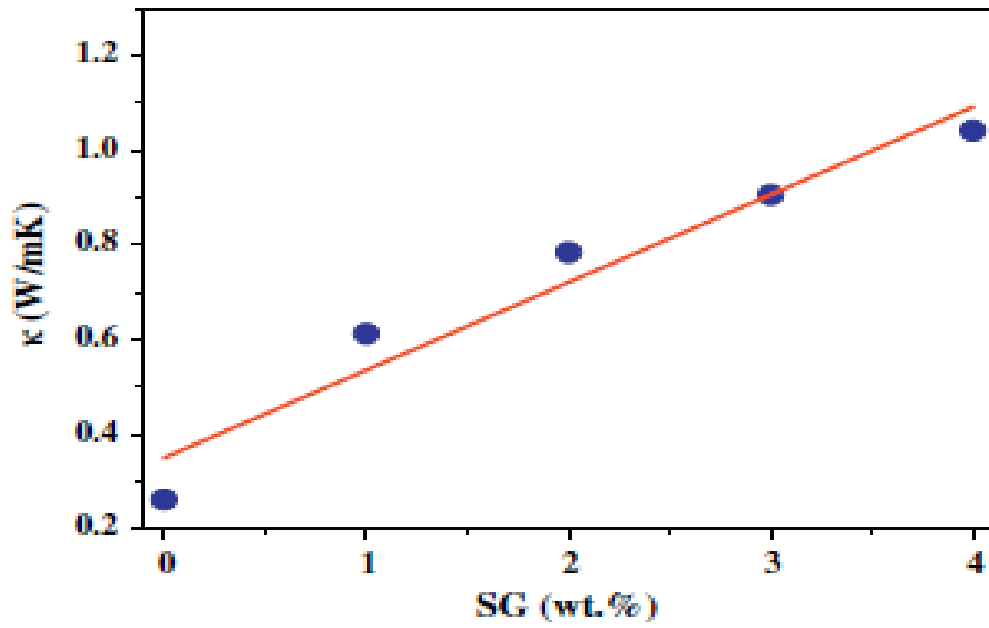
Figure 2.38     Thermal conductivity values at 37 °C for pure PEG and PEG/SG composites as a

function of the mass fraction of SG (Li et al., 2013)
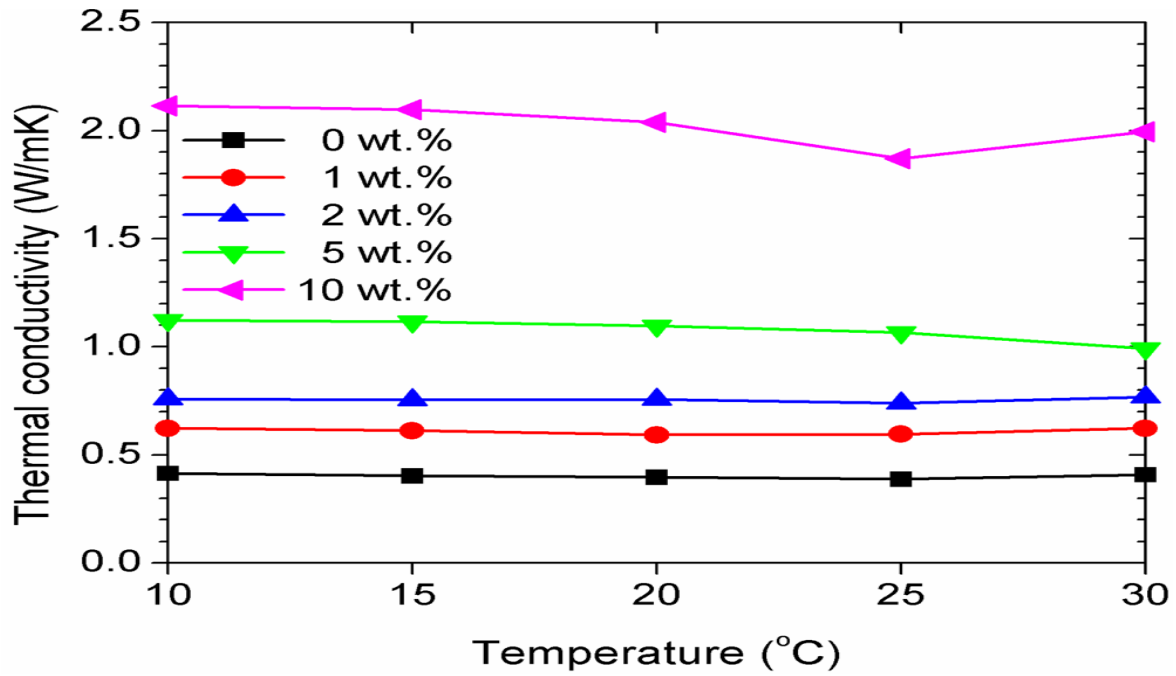
Figure 2.39   Measured thermal conductivity of the pure eicosane and GNP eicosane-based

PCM for different loading of nanoplatelets as a function of temperature from 10

to 30 °C (Fang et al., 2013)
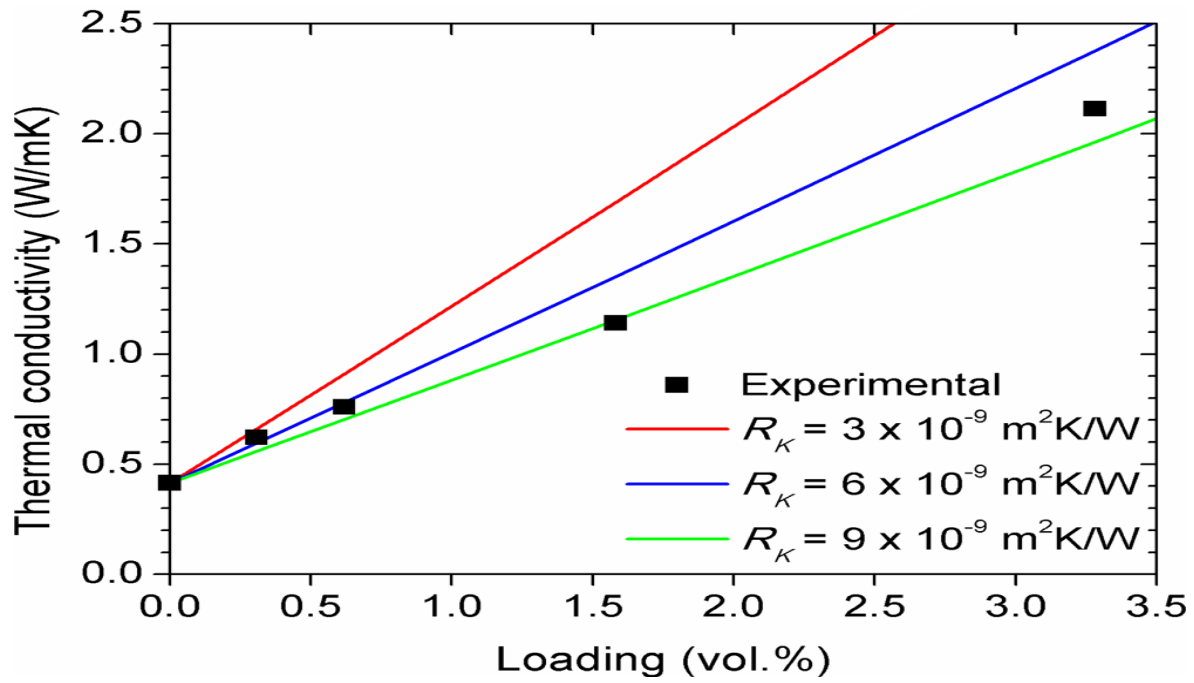
Figure 2.40    Comparison of the measured thermal conductivity enhancement of the eicosane-based composite PCM including the filler/matrix thermal interface resistance effect (Fang et al., 2013)

Chapter 3 Experimental Studies of Eicosane/Silver Nanoparticle Colloids

Moving away from the literature review of Chapter 2, this chapter will focus on presenting results of an experimental study of metallic nanoparticles, specifically silver nanoparticles, dispersed in base paraffin, eicosane, serving the role of the specific phase change material (PCM). Preparation of the Ag/eicosane samples, the experimental and analytical methods of determining the thermal conductivity of the composites for various loadings of Ag nanoparticles will be discussed. Moreover, the effect of the silver nanoparticles on other thermal properties (latent heat and melting temperature) of the NePCM composites will be elucidated.

**3.1 Prior Research Studies on Pure Eicosane and Silver Nano-Structures Dispersed in PCM**

Before going in depth in the present study, a summary of thermal conductivity measurements conducted by several authors on pure eicosane will be discussed. Eicosane, with a melting temperature of 36.4 $^{o}$C, has been the topic of many studies over the years. Eicosane belongs to the family of alkanes (commonly known as Paraffins) and studies of these materials date back numerous decades (Freund et al., 1982). Rastorguev et al. (1974) measured the thermal

conductivity of pure eicosane in the liquid state using the steady-state heated-filament technique. Thereafter, Griggs and Yarbrough (1978) conducted experiments under the solid-state condition using an unguarded radial-heat flow apparatus. To date, more than 20 papers have been published on eicosane focusing on its thermal conductivity, heat transfer properties, crystallization, morphology, microstructure, etc. However, due to the focus of this study on thermal conductivity, 10 relevant papers were extracted and the thermal conductivity data of pure eicosane in both solid and liquid states are listed in Tables 3.1 and 3.2, respectively. The data in these tables were obtained by digitizing the relevant information (http://arohatgi.info/WebPlotDigitizer/app/?) from the relevant publications. Figure 3.1 illustrates the thermal conductivity of the pure eicosane samples in both liquid and solid states; values of the thermal conductivity higher than 0.5 W/mK have been excluded for clarity, however those few omitted data are given in the aforementioned tables. The thermal conductivity data of pure eicosane solid samples of the present study (Table 3.1) correspond to the room temperature preparation route that will be discussed in the experiment section below. In the solid state, for measurements at temperatures less than 36.4 $^{o}$C, an agreement exists between the thermal conductivity values measured in this study and those reported by Nabil (2013), and Stryker and Sparrow (1990). Thermal conductivity values in this study and that of Nabil (2013) were measured using the transient plane source (TPS) technique, a transient method that allows data to be collected in a few minutes, and sometimes as short as 2.5 seconds. On the other hand, Stryker and Sparrow (1990) utilized the steady-state method; a technique where the user must wait for a long period of time in order for the test samples to attain thermal equilibrium. However, when comparing this study's data to those of Griggs and Yarbrough (1978), Yarbrough and Kuan (1981), Fang et al. (2013) and Velez at al. (2014), a discrepancy occurs in

that the measured thermal conductivity decreased as the temperature of the sample increased, whereas in our tests, thermal conductivity was generally directly proportional to temperature; when temperature of the sample was raised, its thermal conductivity was augmented. Griggs and Yarbrough (1978) and Yarbrough and Kuan (1981) credited the decreasing thermal conductivity to the unguarded radial heat flow apparatus leading to a 20% error in measurements because of the changing temperature of the sample. On the other hand, in the liquid state, all measured data showed a decrease in thermal conductivity as the temperature of the eicosane increased with Velez et al. (2014) attributing the decline of thermal conductivity to the change in density, typical of first order phase transition. Rastorguev at al. (1974) observed a similar result, and in order to confirm this decline in thermal conductivity, the authors adopted the Bondi (1962) formula to predict the thermal conductivity where only the structural formula of the paraffin is needed. Bondi (1962) estimated the errors of his formula at 8%, and when the formula was used to theoretically predict thermal conductivity, the deviation varied between 4% and 6% only, exhibiting a decline in thermal conductivity as the temperature was increased in the liquid state.

Regarding metal-based nanoparticles that are investigated in thermal energy storage systems, such nanostructures generally consist of metals that can be silver, copper, aluminum, or oxides that can be magnesium oxide, copper oxide, alumina, and titanium oxide (Khodadadi et al., 2013). In general, nanoparticles with different shapes, sizes and concentrations play a crucial role in the modification of the thermophysical properties of composites (Zhang and Liu, 2013). In this project, metallic silver nanoparticles have been suspended in the PCM to investigate the change in thermal properties of the NePCM samples. Previously, other researchers have used metallic silver or silver oxide as nano enhancers due to their stability, good dispersion within the PCM and very high thermal conductivity compared to other metals. A listing of the data of silver

nanostructure-enhanced PCM is summarized in Table 3.3. In 2010, Zeng et al. (2010) introduced

silver nanowires (Ag NW) into 1-Tetradecanol (TD). Several 1-Tetradecanol/Ag NW composites

with different mass loading (9.09, 23.08, 37.58, 46.08 and 62.73 wt%) of Ag nanowires were

prepared using ultrasonication. Then, thermal conductivity was measured using the transient

plane source technique at room temperature. Results showed a relatively linear increase in

thermal conductivity of the composite as the concentration of the Ag nanowires increased.

Parameshwaran et al. (2014) prepared hybrid nanocomposite phase change material (HyNPCM),

by suspending silver-titania (AgTiO$_2$) nanoparticles into the pure PCM, dimethyl adipate

(C$_8$H$_{18}$O$_4$). The thermal conductivity, measured using the Laser Flash Analyzer (LFA) technique,

of the pure PCM was found to be 0.286 W/mK. Then, the thermal conductivity increased as the

mass fraction of the silver-titania nanoparticles increased from 0.08 to 1 wt%. Parameshwaran et

al. (2014) also examined the thermal conductivity of suspended silver-titania nanoparticles into

the pure PCM ethyl trans-cinnamate (C$_{11}$H$_{12}$O$_2$). Using the LFA technique again, thermal

conductivity was recorded for various mass fractions (0.1, 0.5, 0.8, 1 and 1.5 wt%) of

nanoparticles, and results illustrated an increase in thermal conductivity as the mass fraction of

the nanoparticles increased. Measured thermal conductivity ratios of silver-based nanostructure-

enhanced PCM at room temperature as a function of the mass fraction of the nanoparticles are

plotted in Figure 3.2.  Experimental values of Zeng et al. (2010) were left out to assure clarity of

graphics since they used very high loading of nanostructures (9.09, 23.08, 37.58, 46.08 and 62.73

wt%) and due to the absence of data of the same loading range for comparison. The highest

enhancement of thermal conductivity was obtained by Parameshwaran, Dhamodharan and

Kalaiselvam (2013) using TiO$_2$ nanoparticles, showing an enhancement of approximately 237%.

Still, it must be noted that Zeng et al. (2010), in adding 62.73 wt% of Ag nanowires, exhibited

the highest thermal conductivity, an improvement of 456% from that of the pure PCM. This is attributed to the high aspect ratio of the nanowires, good compatibility with the PCM, and the high thermal conductivity of Ag nanowires. Moreover, all samples exhibited a linear increase in thermal conductivity as the loading of the nanostructures increased; as a result, all the different combinations of the silver-based nano-enhanced phase change materials represent valid candidates for low-temperature thermal energy storage applications.

## 3.2 Preparation of the NePCM Samples

The preparation of the NePCM samples involving suspensions of in-house copper oxide nanoparticles in eicosane was discussed in great detail by Nabil (2013). A similar procedure was followed in the present study with slight changes which will be discussed in the following section. For this research project, eicosane ($C_{20}H_{42}$) with a melting point of 36.4 °C was selected as the base PCM. Eicosane with a purity of 99%, purchased from Sigma-Aldrich, is a white colored paraffin, with a latent heat (heat of fusion) of 247.5 kJ/kg, a boiling point of 345.1 °C and liquid and solid densities of 789 and 840 kg/m$^3$, respectively (Freund et al., 1982). Silver (Ag) was chosen as the nanoparticle enhancers. Silver, possessing good thermal stability and the highest thermal conductivity of all metals, justified its choice of use (Lide, 2005). Silver neodecanoate ($C_{10}H_{19}O_2$) was purchased from Strem Chemicals and served the role of precursor to the silver nanoparticles. The high purity of silver and eicosane, 97% and 99%, respectively, meant that drying of the chemicals was unnecessary to obtain credible data with a low deviation

and error. Transmission electron microscopy (TEM) image (Hossain and Mills, 2015) exhibited that the nanoparticles were nearly spherical with a diameter of approximately 5.5 nm (Figure 3.3). Oleoyl Sarcosine (OS) was obtained from TCI America and was used as a stabilizer for the particles. The standard procedure for the preparation of Ag colloids was described in detail by Darvin et al. (2015). Silver neodecanoate, a white powder, was added rapidly to a solution containing OS in eicosane preheated to 160 °C in an oil bath under vigorous stirring. After addition of silver neodecanoate, the temperature was maintained at that value until the reaction was completed (~ 40 minutes). In order to check the long-term stability of the liquid samples prepared, specimen of different mass fractions (1, 5 and 10 wt%) were left inside the vacuum oven at a temperature of 50 ºC for a time period of 1 week and no precipitation was visually observed for all three Ag/eicosane samples. In preparing solid specimen, a certain amount of colloids was poured into custom-made aluminum molds; the molds have dimensions of 2.54 cm in diameter and 0.9525 cm in height. Upon dispensing the liquid samples in the molds, phase transition was achieved by subjecting the samples to three different methods of solidification. The three distinct solidification/freezing methods entailed:

1. exposing the aluminum molds to an ice-water bath,

2. leaving the molds in the laboratory at room temperature, and

3. placing the molds inside the oven with the oven being turned off.

In effect, the various solidification schemes differed in the period of time the specimens were allowed to freeze at different temperatures while being held at atmospheric pressure. For the first method, the aluminum molds holding the NePCM samples were directly in contact with a bowl of crushed ice, and the duration of the freezing time was about 5 minutes. As for the second route, the samples were left out on a laboratory workbench under the room temperature

and solidification took almost 30 minutes. Finally, for the third and last scheme of freezing of specimen, the vacuum oven (Fischer Scientific, Isotemp® Vacuum Oven Model 281A) was heated to 50 ºC and then turned off with the samples inside; this route took almost 3 hours to be completed. Upon solidification of the samples, the samples were removed from the aluminum molds and pairs of disks with different surface morphologies were obtained. Photographs of the pure paraffin, 1 wt% Ag/eicosane and 10 wt% Ag/eicosane are shown in Figure 3.4. When the mass loading of Ag increased, the color of the samples changed from black to purple to blue; however, after applying heat to the samples during thermal conductivity determination tests, black color persisted as the dominant color of all the samples. Due to the requirements imposed by the transient plane source (TPS) theory in having a tight contact between the heater/sensor and the two samples and the variation of the surface morphology of each sample, two grades of sand paper -beginning with grade 300 and finishing with grade 400- were used to flatten the sides of the disks before subjecting these to thermal conductivity measurements. The samples weighed on average 4 grams, and a brief overview of the preparation steps is shown in Figure 3.5.

## 3.3 Thermal Conductivity Measurements

There are numerous ways to measure the thermal conductivity of a material such as the *steady-state method* adopted by Beck (1957), and the *transient methods* which are more common and widely adopted by researchers. To name a few studies, Nagasa and Nagashima (1981) used

the transient hot wire (THW) technique, Parker et al. (1961) adopted the laser flash technique, while the transient plane source (TPS) technique was investigated by Nabil and Khodadadi (2013). All the aforementioned techniques fall under the category of the transient methods. Depending on the state, type, and form of the material under consideration, an appropriate method is chosen. For liquid samples, in order to avoid onset and persistence of natural convection during the measurements which would affect the thermal conductivity data, transient methods are favored due to its desirable feature of acquiring data over a short time duration compared to the steady-state methods, where one must wait a long time for establishment of a stable temperature gradient within the testing sample. The concepts and theory behind the two classes of approach are discussed in great detail by Wakeham and Assael (1999).

### 3.3.1 Instrumentation

For this project, the thermal conductivity measurements of the Ag/eicosane NePCM samples were obtained using the transient plane source (TPS) technique at different temperatures ranging from 10 ºC to 35 ºC or up to the melting point of the specific sample, whichever temperature was reached first. The instrument used, a Hot Disk Thermal Constants Analyzer (TPS 500), can measure the thermal conductivity of the material along with other thermophysical properties (thermal diffusivity, specific heat, etc.) in a period of time as short as 2.5 seconds. In addition, the instrument can measure values of thermal conductivity as low as 0.1 W/mK, and with the thermal conductivity of eicosane in the range of 0.1-0.4 W/mK, the TPS instrument justified its applicability in this project. Another advantage of this instrument would be its low

uncertainty, as reported to be at maximum 5% by the manufacturer. A benchmark test was done to verify the accuracy and credibility of that statement. The samples in use were stainless steel disks provided by the manufacturer. The test was carried out under room temperature and a total of 10 runs were performed. The experimental result, a thermal conductivity value of 14.04 W/mK, was in great agreement with the actual value of 14.2 W/mK provided by the company, a difference of just 1.4%. Before getting in depth with measurements of the thermal conductivity and analysis of data, a description of the Hot Disk Analyzer system and the experimental setup are presented.

Based on the theory of the Transient Plane Source technique (recognized in ISO Standard 22007-2:2008), the TPS method utilizes a sensor element in the shape of a double spiral. The TPS sensor serves a dual purpose: it functions as a planar heat source for increasing the sample's temperature and it serves simultaneously as a resistance thermometer for recording the transient temperature rise versus heating time. Two sensor elements, with different outer radii, were available, and for this study the sensor with the smaller radius of 3.189 mm was used in the measurements. The choice of the sensor element with a smaller radius is due to the dimensions of the NePCM samples and their expected low thermal conductivity value. The sensor of choice is made of a 10 μm thick Nickel-metal double spiral, and is coated with the polyimide "Kapton" to provide protection of the sensor's shape, to give it mechanical strength and to keep it electrically insulated. Since the Ag/eicosane samples are in the solid phase, the encapsulated Ni-spiral sensor is to be sandwiched between two identical samples. An assumption of the theory governing the operation of the TPS technique is that the sensor is located in an infinite material, which in practice means that the transient recording's total time is limited by the presence of the outside boundaries of the sample. In other words, the thermal wave generated by the sensor must

not be allowed to reach the outside boundaries of the samples. As a result, great care must be taken in defining the "thermal probing depth", thus making sure the wave does not exceed the size of the samples during the transient recording. After setting the measurement time of the experiment, 200 temperature data points are recorded at equal time intervals, and from these recordings, the relation between the sample temperature and time is established. Parameters such as the applied heating power to increase the temperature of the spiral, the measurement time for recording the 200 temperature data and the choice of the sensor's size that affect the measurement were carefully selected to optimize the settings of the measurements and obtain more accurate results. In choosing the right sensor, the thickness of the sample must not exceed the radius of the sensor; so the parameter that needs to be satisfied is that of the "Total to Characteristic Time (TCT)", which is defined as $r^2/\alpha$, where $r$ is the radius of the sensor in mm and $\alpha$ is the thermal diffusivity of the sample in mm$^2$/s. The instruction manual (Hot Disk, 2009) recommends a range of 0.33 and 1 s for a measurement and if that range is not satisfied, the sensor and/or test time must be changed. Another criterion resides in the probing depth of the thermal wave; this is typically the shortest distance from the tip of the sensor to the outer boundary of the sample; in other words, it refers to the thickness of the sample. The theory behind the TPS technique assumes an infinite material with no boundaries, but since experimentally this is not practical, one must make sure that the available probing depth is always greater than the measured probing depth. If that is not the case, then the test time must be either shortened or extended depending on the value of TCT. Other important criteria, related to the choice of the heating power, are the temperature increase between the first and last point used in the data analysis (must be between 0.4 and 4 K) and the mean deviation of the points (a deviation with a magnitude of $10^{-4}$ K is typical). If the results did not fall in those ranges, then a

new heating power must be chosen. Finally, the reader might be interested in conducting measurements in the liquid state instead of the solid state. In that case, more restrictions apply and one important parameter that must not be overlooked is the onset of natural convection, which was analyzed and examined by Warzoha and Fleischer (2014a) using numerical modeling. The second part of the study by Warzoha and Fleischer (2014b) investigated the accuracy of the conventional method of measuring thermal conductivity of the liquids using the transient plane source technique, while also introducing a novel method for determination of the thermal conductivity of liquids using the TPS.

### *3.3.2 Experiment Details*

As for the experimental setup, two aluminum cold plates (LYTRON Co., Woburn, MA, Model CP20G01) that served as means of controlling the reported measurement temperature were utilized. A pair of identical Ag/eicosane composites was placed on the two cold plates, with the TPS sensor sandwiched in between the two disks and perfectly centered. To assure thermal contact between the cold plates and the samples, green-colored 3 mm thick layers of Gap Pad$^{®}$ 300S30 (The Bergquist Company, Minnesota, USA) with a thermal conductivity of 5 W/mK were placed between the NePCM and the cold plates. Also, to reduce heat loss to the environment, Styrofoam$^{®}$ was used to insulate the experimental setup from the ambient temperature. Two adjustable side screws and a circular metal plate were also used to keep the sensor at a horizontal position between the two samples. Another screw at the top of the setup was used to compress the two plates together to impose uniform pressure on the entire assembly.

The liquid flow passageways of the aluminum cold plates were connected to the ports of a programmable bath circulator. The bath (TP-502P, Brookfield, Middleboro, MA) with a temperature stability of 0.01 ℃ and a pumping rate varying from 0.006 to 0.015 m$^3$/min was used to control the temperature of the working fluid. The working fluid, a distilled water/ethylene glycol 1:1 mixture with a freezing point of about -34 ℃, was employed in order to attain the bath temperature below ice point (0 ℃). Due to the internally-crisscrossed finned structure of the aluminum cold plates that promotes great mixing, the temperatures of the two plates can be adjusted quickly to the temperature of the working fluid. In addition to the internal temperature sensor of the bath, an external 2-wire thermistor (GE, Model A733F-CSP60BT103M, St. Marys, PA, accuracy of 0.01 ℃) was also used to monitor the bath temperature and that of the samples. The thermistor was placed between the two samples in the middle of the two cold plates, and a waiting time period of 60 minutes elapsed in order to establish thermal equilibrium at each measured temperature. The temperature reading of the thermistor served as the measurement temperature that is reported in this investigation.  A schematic diagram giving details of the sample holding apparatus was provided in Figure 3.9 of Nabil's thesis (Nabil, 2013).  The measurement temperature was increased in increments of 5 ℃ for the 10-30 ℃ range. After that, the temperature was raised by 1 ℃ at a time to further resolve the measurement temperature near the melting point of the respective sample.  The TPS500 was operated with a heating power of 0.1 W for duration of 5 or 10 seconds, and as the temperature of the samples increased, the applied power was decreased to 0.03 W, while the measurement time reached a maximum of 10 seconds. As for the probing depth, it was measured to be about 3 mm, never exceeding the available probing depth (5 mm) of the solid disks.  These settings

proved to be the most accurate and provided the best reproducibility of the 200 data points collected for each run.

### 3.3.3 Effect of the Contact Resistance on TPS Measurements

The uniform pressure applied by the top screw on the upper cold plate holding the samples plays a major role in recording the correct values of thermal conductivity of the composites. The screw needs to be positioned tightly to the plate to ensure no air is trapped between the samples and the sandwiched heater/sensor (note that air might even circulate). However, by ensuring a very tight grip of the plates and the sensor, the sensor might be damaged. As a result, a low thermal contact resistance is desirable and a middle ground must be attained. Nabil (2013) performed thermal conductivity measurements on pure eicosane prepared under ambient temperature for three different temperatures (10, 20 and 30 $^{o}$C), while changing the pressure applied by adjusting the top screw. The first configuration was obtained once the tip of the adjustable screw was in contact with the plate, followed by step size increments of 0.25 turns up to 1.25 turns. Experimental data showed that for a number of turns equal to or greater than 0.5 turns, thermal conductivity data showed an asymptotic behavior and was independent of the number of turns of the screw. The measured thermal conductivity values of this test are given in Table 3.4. Consequently, all the measurements in this project were recorded at exactly 1 full turn of the screw.

**3.4 Latent Heat and Melting Point Measurements**

In addition to thermal conductivity measurements, the latent heat (heat of fusion) and the melting point of the eicosane-based NePCM samples containing silver nanoparticles have been investigated, utilizing differential scanning calorimetry (DSC). DSC is a form of calorimetry where a temperature range of interest is scanned for a specimen. In addition to the sample, a base reference specimen is exposed to the same temperature program. The reference in use is employed to determine the heat stored in the sample by the difference in the signal of the sample compared to that of the base reference. The benefit of this strategy is a higher precision of the determination of the heat flow into the sample (Mehling and Cabeza, 2008). DSC equipment is based on two principles of operation, i.e. power compensating calorimeters or heat exchanging calorimeters. The former type of DSC is uncommon and uses electrical heaters to compensate the temperature difference between the sample and a reference when a temperature range is scanned. On the other hand, heat exchanging calorimeters are widely used, where the difference in the heat exchanged between the ambient and the sample and between the ambient and a reference is determined via a thermal resistance $R_{th}$.

*3.4.1 Instrumentation and Experiment Details*

Differential thermal analysis was carried out on the FP90 Central Processor/FP99 Software in the temperature range of $-100$ to $600\ ^oC$. The FP90 (Mettler-Toledo International

Inc., Columbus, Ohio) serves as the control unit and communication system of the thermal system. After attachment of the measuring cell FP84HT to the control unit FP90, several thermophysical properties can be measured such as the heat of fusion $(\Delta H)$, specific heat capacity $(C_p)$, and melting point of the material $(T_m)$. The FP84HT Hot Stage simultaneously allows visual observation of the sample and measurement of the heat flows following the DSC principle. Some of the specifications of the hot stage are that it can be utilized in the range of -60 to 375 $^o$C with an accuracy of ±0.6 $^o$C.  The instrument was calibrated using Indium (99.999%) as suggested by the manufacturer. The tested NePCM samples weighed in the range of 4-8 mg, and were subjected to four (4) cooling and heating cycles at a ramping rate of 5 $^o$C/min; starting at 10 $^o$C and ending at 60 $^o$C, lasting a period of 10 minutes. The characteristics of the TPS and the DSC instruments are tabulated in Table 3.5.

## 3.5. Results and Discussion

For all the NePCM samples of different mass fractions of silver nanoparticles, 3 runs were conducted at each measurement temperature and the average of the three runs was reported. The standard deviation was on average 1.33% for all the samples regardless of the solidification method. For all reported figures, except for Figure 3.12, the values of the measured thermal conductivity near the respective melting temperature are excluded so as to maintain clarity of the presented data and graphics. A detailed analysis of the results is discussed below.

As mentioned previously, Differential Scanning Calorimetry (DSC) was used to measure the heat of fusion and the melting point of the NePCM composites. The reported results were the average of three runs and obtained from the third heating cycle, with a reproducibility of ±5%. The DSC data for samples prepared following the room temperature approach are tabulated in Table 3.6. The experimental and theoretically-predicated values of the phase change temperature of the pure eicosane and the Ag/eicosane NePCM samples prepared following the room temperature approach are plotted in Figure 3.6. Also, the DSC curves of pure eicosane, 1, 2 and 3.5 wt% Ag/eicosane samples, and the DSC curves of 5, 6.5, 8 and 10 wt% Ag/eicosane composites are plotted in Figures 3.7 and 3.8, respectively. For all these date, a ramping rate of 5 $^{o}$C/min was used.  For the experimental results, the transition temperature marking the transition between the solid and liquid states was measured at the inception of the peak of the DSC curves, while the latent heat was measured as the integrated area under the curve.

Results showed that the latent heat and the melting point of the NePCM samples are inversely proportional to the concentration of the additives. As the particles' loading increased, the melting point of the NePCM decreased slightly. A consequence of the variation of the melting point of the composites is the need to conduct the thermal conductivity measurements for a different applicable range of temperature when getting close to the respective melting point of the specific sample. As depicted in Table 3.6, the experimental results for the melting temperature are in great agreement with the values based on theoretical predictions. Equation

(3.1), given by Noggle (1989), was used to calculate the theoretical values of the melting temperature:

$$T_m = T_m^\circ - K_f m \tag{3.1}$$

where $T_m$, $T_m^\circ$, $K_f$, and $m$ denote the melting temperature of the Ag/eicosane composite (ºC), the literature value of the phase change temperature of the pure solvent (melting point of pure eicosane is 36.4 ºC according to Freund et al., (1982)), the molal freezing-point-depression constant of eicosane (3.23 kgK/mol), and the molality of the composite, respectively. Molality is the ratio of the number of moles of the solute to the mass of the solvent ($m = \frac{n_{silver\ nanoparticles}}{m_{eicosane}}$). But before application of Eq. (3.1), one must determine the molal freezing-point-depression constant of eicosane. Due to the absence of literature data on the specific constant for eicosane, the following equation, also introduced by Noggle (1989) was used in determining the parameter:

$$K_f = 0.1 R T_m^{\circ\ 2}/\Delta H^o \tag{3.2}$$

where $R$ stands for the universal gas constant (8.314 J/molK) and $\Delta H^o$ stands for the latent heat of fusion of the pure sample (247.5 J/g). Once the constant was calculated, it was substituted in the previous equation along with the molality of the respective sample to determine its melting temperature. The explanation behind the decrease in the melting point resides in the colligative properties of the composites; as the concentration of the nanoparticles increase within the

composites, the number of molecules of the solvent to undergo phase change transition decreases, leading to a lower melting temperature.

As for the theoretical heat of fusion data, great care must be taken in converting the experimental values of the mass fraction ($\emptyset_{wt}$) of the Ag nanoparticles to the volume fraction ($\emptyset_{vol}$) of the fillers in the colloids used exclusively in theoretical models. Although the weight fraction of the nano-additives doesn't change during solidification of the samples, the volume fraction of the liquid and solid samples are different since the base PCM shrinks during the phase change because of the higher density of eicosane in the solid phase ($\rho_s$= 840 kg/m³ and $\rho_l$= 789 kg/m³). Assuming a two-component system, Equation (3.3) was used to convert the mass fraction of the nanoparticles within the prepared liquid samples to the volume fraction of the samples in solid phase:

$$\emptyset_{vol} = \frac{\emptyset_{wt}\rho_c}{\emptyset_{wt}\rho_c + (1-\emptyset_{wt})\rho_d} \tag{3.3}$$

where $\rho$ stands for the density of the discrete (subscript $d$, i.e. Ag nanoadditives) and the continuous (subscript $c$, i.e. eicosane) phases, and $\phi_{wt}$ stands for the weight fraction of the additives. In using the above formula, the density of the base PCM eicosane in the solid phase must be used. Then, Equation (3.4) was used to determine the theoretical values of the latent heat according to a simple mixture rule (Khodadadi and Hosseinizadeh, 2007):

$$\Delta H = (1 - \emptyset_{vol})\frac{\rho_c}{\rho_{eff}}\Delta H^o \tag{3.4}$$

where $\rho_{eff}$ , the effective density of the Ag/eicosane composites, is given by:

$$\rho_{eff} = (1 - \emptyset_{vol})\rho_c + \emptyset_{vol}\rho_d \tag{3.5}$$

114

where $\Delta H$ stands for the heat of fusion of the Ag/eicosane composites (J/g) for each loading of silver nanoparticles. The predicted values of the heat of fusion of Ag/eicosane composites are given in Table 3.6. Unlike the melting point data, a discrepancy is observed between the experimental and theoretical values of the latent heat. As can be seen from Figures 3.7 and 3.8, a noticeable drop occurs in the experimental heat of fusion values reaching a value as low as 78.3 J/g for a mass loading of 10 wt%. It must be noted that Eq. (3.4) is an approximation of the theoretical latent values due to the absence of a complete definition of heat of fusion of colloids in the literature. Similar to the decrease of the melting temperature, the decrease in the latent heat of fusion of the samples is due to the colligative properties; a component with less solvent and more solute will lose its ability to store thermal energy and therefore exhibits a low value for latent heat of fusion.

Experimental thermograms of the melting and crystallization of pure eicosane of this study prepared following the room temperature solidification protocol and that of Kolesnikov and Syunyaev (1985) who used a ramping rate of 1 $^{\circ}$C/min are presented in Figure 3.9a-b. The present DSC results suggest that as the temperature of the sample was raised, melting of eicosane was characterized by one exothermic peak, whereas the endothermic reaction upon cooling is marked by two distinctly separated peaks. When comparing our results to a study investigating the phase transformation of both eicosane ($C_{20}H_{42}$) and octadecane ($C_{18}H_{38}$) (Kolesnikov and Syunyaev, 1985), a disagreement is observed in the heating segment of the cycle. These authors reported two neighboring peaks (shown as an inset in Fig. 3.9b), where the first peak was ascribed to a solid-solid phase transition and the second peak corresponded to a solid-liquid phase change, analogous of the melting of eicosane. In our research, only one peak was observed when eicosane was being heated during melting of the paraffin. For the endothermic reaction, the

DSC figures agreed with the result of Kolesnikov and Syunyaev (1985). The authors claimed that the first of the two peaks observed during the cooling portion of the cycle corresponds to crystallization, while the second peak corresponds to a structure modification (transition from the triclinic structure to the hexagonal structure shown in Figure 3.9c. Paraffins, at temperatures below their melting point, are always crystalline whether they exist as solitary chemical compounds or in mixtures (Freund, 1982). As noted by Nyburg and Potworowski (1973), the n-alkanes, $C_nH_{2n+2}$ for $n \geq 6$, crystallize in four ways depending on the purity and parity of *n*:

1. triclinic, for *n* (even) $\leq$ 26 (Muller and Lonsdale, 1948),

2. monoclinic, if the paraffin is pure, for $26 \leq n$ (even) $\leq 36$ (Broadhurst, 1962),

3. orthorhombic, if the paraffin is not pure, for $26 \leq n$ (even) $\leq 36$ (Broadhurst, 1962),

4. orthorhombic, $11 \leq n$ (odd) $\leq 39$ (Piper and Malkin, 1930).

Moreover, crystallization takes place from either the melt or from the solution, with the latter case forming well-defined crystals. Information developed on crystallography of n-alkanes has been very limited over the years, due to the inability of growing large single crystals with sufficient size, high quality, and suitable purity for the traditional structural analysis using X-ray diffraction methods (Craig et al., 1994). Still, Nyburg and Gerson (1992) investigated the crystallography of eicosane, $C_{20}H_{42}$. Although, patterns of the pure eicosane were not investigated by Nyburg and Gerson (1992), the study presented the atomic fractional coordinates, equivalent isotropic temperature factors, and the C-C bond lengths and angles for eicosane. More significantly, the authors reiterated the triclinic structure of the eicosane, as mentioned before, and compared its structure to other n-alkanes such as $C_{18}H_{38}$, $C_{36}H_{74}$ and $C_{38}H_{78}$.

In order to verify the presence of crystalline structures in our Ag/eicosane samples, X-ray diffraction (XRD) patterns were collected using the Bruker D-8 Discover system housed at Wilmore Laboratory in the Materials Engineering Department at Auburn University (http://eng.auburn.edu/programs/matl/index.html). This instrument is a two-circle goniometer with an angular precision of $\pm 0.0001^o$ and an angle measuring accuracy of $0.005^o$. The X-ray diffraction patterns were recorded using $\theta/2\theta$ geometry with $2\theta$ ranging from $5^o$ to $90^o$ in steps of $5^o$. Diffraction scans were recorded for a stationary solid sample prepared following the room temperature freezing scheme, and all measurements were carried out under ambient conditions. X-ray diffraction patterns of pure eicosane, 1 and 10 wt% Ag/eicosane NePCM composites at room temperature, along with an inset of the XRD pattern of silver are plotted in Figure 3.10. The X-ray Diffraction pattern for silver nanoparticles shown as an inset in Figure 3.10 was obtained upon preparation of Ag in PEG (polyethylene glycol) samples, measured by Hossain and Mills (2015) of the Chemistry Department at Auburn University, using the Ultima IV X-ray Diffractometer (Rigaku, Texas, USA). The sharp and intense peaks in Figure 3.10 are an indication of the crystalline structure of the paraffin, proving the formation of crystals during the preparation of the NePCM. As for the presence of silver nanoparticles, the X-ray diffraction machine was not able to precisely identify the peaks attributed to silver for all four lattice planes, possibly due to the their small size (~ 5.5 nm) and their low concentration in the NePCM composites. However, in Figure 3.10, at 10 wt% loading of Ag nanoparticles, a broad range of x-ray diffraction could be observed at $38^o$; an indication of the presence of silver nanoparticles indexed to the dominant (111) lattice plane.

_3.5.2 Ice-Water Bath Solidification_

The measured thermal conductivity of solid pure eicosane and Ag/eicosane composites that were prepared following the ice-water bath route are tabulated in Table 3.7 and plotted in Figure 3.11. As shown in the figure, the thermal conductivity of the NePCM generally increased as the temperature of the samples increased. This result differed from the findings of Nabil and Khodadadi (2013) who reported that the thermal conductivity measurements of CuO/eicosane composites were independent of temperature. Parallel to Fan (2011) and Nabil (2013) who worked with CuO/eicosane composites, a sharp rise in the thermal conductivity value was recorded when the samples' temperature was close to the respective melting point of the samples. A clear explanation to the occurrence of this jump hasn't been found yet, but efforts are presently being made to explain this behavior. This temperature range, where the sample has not yet completely melted, is a non-equilibrium state. If studies or efforts are made to keep the sample in that state, the utility of the NePCM in relation to charging of the medium would be very desirable for thermal energy storage applications. Furthermore, a rise in thermal conductivity is observed as the mass fraction of the nanoparticles increases for all measured temperatures up to the 2 wt% loading. For higher values of particle loadings, a non-monotonic relation existed between the loading of the NePCM and its thermal conductivity regardless of the temperature. In effect, values of thermal conductivity for the 3.5 and 5 wt% samples were consistently lower than the values at a loading of 2 wt%. Then at 6.5 wt% and beyond, thermal conductivity starts increasing again reaching its greatest value for a mass fraction of 10 wt% (0.5481 W/mK corresponding to 35.27% enhancement compared to pure eicosane).

In addition to the trends discussed above, the ice-water bath solidification method consistently exhibited the lowest values of thermal conductivity when compared to the values obtained for samples prepared under room temperature and oven solidification routes as illustrated in Figure 3.12 (10 wt% samples and melting temperature of 33.5 $^{\circ}$C for the room temperature sample). As for the remaining NePCM composites with different loadings of silver nanoparticles, the reader is directed to Appendix A. A possible explanation behind this phenomenon is the presence of air pockets trapped inside the sample during its freezing. The samples solidified under room temperature and in an ice-water bath are susceptible to greater retention of air pockets (voids) which will alter the sample and decrease the thermal conductivity of the NePCM. And since the ice-water bath technique is the quickest among the three methods, a lower thermal conductivity value was expected.

*3.5.3 Oven Solidification*

The measured thermal conductivity of the solid pure eicosane and Ag/eicosane composites that were prepared following the oven solidification method are tabulated in Table 3.8 and presented in Figure 3.13. As in the case with the ice-water bath samples, the oven solidification scheme samples exhibited a relation between the temperature and the thermal conductivity; as the temperature of the sample increased so did the thermal conductivity regardless of the mass fraction of the nanoparticles. In addition to that, for the temperature range of 30-35 $^{\circ}$C, the thermal conductivity rise is steep and that slope becomes more marked as the sample's temperature gets close to the respective phase change temperature. At that point, an

119

abrupt rise in thermal conductivity is exhibited that is commensurate with findings for samples prepared using the previous method of freezing, and as also found by Fan (2011) and Nabil (2013) for their CuO/eicosane composites. Furthermore, a monotonic rise of thermal conductivity occurs up to the 2 wt% loading of Ag nanoparticles. Beyond that loading, a decreasing trend is detected up to 6.5 wt% followed by an augmentation of thermal conductivity values up to 10 wt%. The highest value of thermal conductivity was achieved for this loading of nanofillers (0.5862 W/mK, i.e. an enhancement of 28.95% compared to pure eicosane).

As for the 10 wt% loading of Ag nanostructures, thermal conductivity data measured for samples prepared following the oven solidification method showed the highest values when compared to the other two methods (Figure 3.12). Another potential explanation resides in the change of the microstructure of the NePCM and the time duration of the solidification process. A longer phase change time period would lead to formation of bigger micro-scale grains; therefore reducing thermal resistance layers leading to an increase of thermal conductivity.  And as mentioned before, the absence of trapped gases and air voids in the samples solidified in the oven could also lead to the high values of thermal conductivity of NePCM.

*3.5.4 Room Temperature Solidification*

The measured thermal conductivity of the solid pure eicosane and Ag/eicosane composites that were prepared following the room temperature method are tabulated in Table 3.9 and illustrated in Figure 3.14. Similar to what was mentioned above, thermal conductivities of these samples were dependent on the temperature of the samples, and when close to the specific

melting point of each sample, a jump in thermal conductivity was obtained. In addition to the jump in thermal conductivity, values of thermal conductivity of the samples prepared following the room temperature route were higher than the ice-water bath samples but still lower than the samples prepared in the oven for most measurement temperatures (Figure 3.12). Focusing at one specific measurement temperature, there is an increasing trend up to 2 wt%. Above this loading, a non-monotonic relationship exists between the thermal conductivity of the sample and the particles loading, regardless of the temperature range studied, with the highest loading recorded at 10 wt%. The thermal conductivity value for the sample prepared using the ice-water bath scheme for the 10 wt% loading was 0.8319 W/mK, while the value, at the same loading, recorded for the room temperature freezing sample was 0.8534 W/mK, and the greatest thermal conductivity of all samples was 0.8754 W/mK measured following the oven solidification route.

The ratio of the thermal conductivity of the Ag/eicosane composites ($k_{eff}$) to the thermal conductivity of pure eicosane (relative thermal conductivity), prepared under the room temperature protocol, and the theoretical values based on the Maxwell's model (1873), have been calculated and illustrated in Figure 3.15. Maxwell's relation is given in Equation (3.5) (Das et al., 2008):

$$k_{eff} = k_c \left[ \frac{k_d + 2k_c - 2\emptyset_{vol}(k_c - k_d)}{k_d + 2k_c + \emptyset_{vol}(k_c - k_d)} \right]$$
(3.5)

where subscripts *eff, c, d* and $\emptyset_{vol}$ denote effective, continuous (base PCM eicosane), discrete (Ag nanoparticles), and the volume fraction of the nano-additive materials, respectively. It should be noted that the volume fraction of the solid samples were obtained using relation 3.3. There is no value in the literature for the thermal conductivity of the silver neodecanoate, the

precursor of the silver nanoparticles, so a thermal conductivity of 429 W/mK is adopted for $k_d$ (Yaws, 2009). As discussed earlier, the experimental data clearly exhibit the non-monotonic dependence of the thermal conductivity on mass fraction, regardless of the measurement temperature. However, the predicted values of the relative thermal conductivity, given by the Maxwell model exhibit a monotonic relation, which are consistently below the measured values. This suggests that in our NePCM samples, the colloids were not ideally well-dispersed in the solution as modeled by Maxwell and agglomeration of nanoadditives were present thus establishing a more effective thermally conductive network. In addition to the Maxwell's model, the figure of merit that quantifies the value and importance of the Ag nanoparticles and CuO nanoparticles (Nabil, 2013) as a function of the volume fraction of the nano-structures, is illustrated in Figure 3.16. Ideally, for highly conductive nanofillers ($k_d \rightarrow \infty$) and small volume fractions, the limit of the figure of merit based on the Maxwell's model is equal to 3. In this study, the figure of merit reached a value as high as 83, while the CuO nanoparticles exhibited a maximum value of 23, at 2 wt% loading of nanofillers, thus showing that silver metallic nanoparticles are a better choice for thermal energy storage applications. Furthermore, even though the figure of merit decreases as the volume fraction of the nanostructures increases, the minimum value of about 19 in this research remains well above the Maxwell's model limit of 3. Focusing on a specific measurement temperature, e.g. $T= 31$ $^{\mathrm{o}}$C, a non-monotonic relation, also observed for the other two methods of solidification, exists between the thermal conductivity and the mass fraction (Figure 3.15). Also, a dependence of the thermal conductivity on the measurement temperature was observed for any specific mass fraction and all the experimental data were greater than the Maxwell's prediction. In addition to that, the plot exhibits the steep thermal conductivity rise when the sample reaches a temperature in the range of 30-35 $^{\mathrm{o}}$C.

It should be noted that whereas the uncertainty associated with the TPS thermal conductivity data was estimated to be 5% of the measured value, there are uncertainties associated with using the Maxwell relation. Uncertainty analysis was conducted for equations (3.3) and (3.5) in order to determine the dependency of these relations on the following parameters: density, thermal conductivity, mass fraction and volume fraction. A method to estimate the uncertainty in experimental results was presented by Kline and McClintock (1953), a model that was followed by many researchers in estimating the uncertainty in their experimental data. This method is described in detail along with the results of its application to the two aforementioned equations in Appendix B.

## 3.6 Summary

To sum up this work, eicosane-based NePCM containing suspensions of Ag nanoparticles of different weight fractions (0, 1, 2, 3.5, 5, 6.5, 8 and 10 wt%) were prepared following three different solidification schemes. The NePCM colloids showed no precipitation for all Ag loadings, and the samples were found to be stable for a long period of time. The Transient Plane Source (TPS) technique, along with a controllable bath/circulator to adjust the measurement temperature of the samples, was used to measure the thermal conductivity of the NePCM of different loadings at different temperatures below and near their respective melting temperatures. Results generally showed an increase in the value of thermal conductivity as the temperature of the solid sample increased regardless of the preparation route and the particles loading.

Furthermore, when the measurement temperature was close to melting point, a sharp rise in thermal conductivity was observed for all NePCM samples. As for the different solidification protocols, the samples prepared utilizing the oven solidification route exhibited the highest values of thermal conductivity, while NePCM samples prepared following the ice-water bath scheme showed the lowest values because of the change in the microstructure of the samples and the possibility of presence of air voids. In addition to that, a non-monotonic relationship between the thermal conductivity and the mass fraction of the Ag nanoparticles was observed above a loading of 2 wt%. Finally, DSC was used to measure other thermal properties such as the heat of fusion and the melting point of the NePCM. Experimental and theoretical data showed a decrease in the aforementioned properties as the additives' loading increased leading to the decrease in the number of molecules of the solvent eicosane in the samples. Due to the decreasing phase change temperature, the choice of the amount of silver nanoparticles to be added to the PCM depends on the type of application of the thermal energy storage material.

Table 3.1    Thermal conductivity data of pure eicosane in the solid state as measured by the authors of the published journal papers

| | Griggs and Yarbrough (1978) | Yarbrough and Kuan (1981) | Stryker and Sparrow (1990) | Fan (2011) | Nabil (2013) | Fang et al. (2013) | Velez et al. (2014) | Al Ghossein (2015) |
|---|---|---|---|---|---|---|---|---|
| Instrument | SS[1] | SS | SS | TPS[2] | TPS | TPS | THW[3] | TPS |
| Temperature (°C) | k (W/mK) | k (W/mK) | k (W/mK) | k (W/mK) | k (W/mK) | k (W/mK) | k (W/mK) | k (W/mK) |
| 2 | | 0.413 | | | | | | |
| 6 | | 0.393 | | | | | | |
| 10 | | 0.392 | 0.4229 | | 0.4212 | 0.4137 | 0.438 | 0.4212 |
| 13 | | 0.355 | | | | | | |
| 15 | | 0.344 | 0.4241 | | 0.423 | 0.4031 | 0.425 | 0.4236 |
| 20 | | 0.341 | 0.4235 | 0.4236 | 0.4223 | 0.3956 | 0.388 | 0.4245 |
| 25 | 0.3569 | | 0.4224 | | 0.4241 | 0.3869 | 0.364 | 0.4233 |
| 30 | 0.3375 | | 0.4182 | 0.3866 | 0.4244 | 0.4077 | 0.328 | 0.4241 |
| 31 | | | | | | 0.4382 | | 0.4266 |
| 32 | | | 0.4190 | | 0.4267 | | | 0.4227 |
| 33 | | | | | 0.4229 | 0.7120 | 0.295 | 0.4488 |
| 34 | 0.3104 | | 0.4131 | | 0.4513 | 1.0051 | | 0.4526 |
| 35 | | | | 0.6608 | 0.5503 | 1.407 | | 0.5467 |

[1] SS denotes the steady-state methods.
[2] TPS denotes the transient plane source technique.
[3] THW denotes the transient hot-wire method.

Table 3.2    Thermal conductivity data of pure eicosane in the liquid state as measured by the authors of the published journal papers

| | Rastorguev et al. (1974) | Yaws and Gabulla (2003) | Fan (2011) | Velez et al. (2014) |
|---|---|---|---|---|
| *Instrument* | $HFM^1$ | $(k=A+BT+CT^2)^2$ | $TPS^3$ | $THW^4$ |
| *Temperature ($^oC$)* | k (W/mK) | k (W/mK) | k (W/mK) | k (W/mK) |
| *40* | | 0.1469 | 0.1485 | 0.1543 |
| *45* | | 0.1459 | | 0.1510 |
| *50* | | 0.1450 | 0.1473 | 0.1510 |
| *55* | 0.1442 | 0.1441 | | 0.1494 |
| *60* | | 0.1432 | 0.1432 | 0.1477 |
| *65* | | 0.1423 | | 0.1469 |
| *70* | | 0.1413 | | 0.1461 |
| *75* | | 0.1404 | | 0.1453 |
| *80* | 0.1389 | | | |
| *100* | 0.1341 | | | |
| *120* | 0.1296 | | | |
| *140* | 0.1251 | | | |
| *160* | 0.1208 | | | |
| *180* | 0.1167 | | | |
| *200* | 0.1128 | | | |

[1] HFM denotes the heat filament method.

[2] *A, B* and *C* are the regression coefficients for the chemical compound. In the case of eicosane, *A, B* and *C* are equal to 0.2068, -1.999x10^-4 and 2.6667x10^-8, respectively. *T* denotes temperature in Kelvins.

[3] TPS denotes the transient plane source technique.

[4] THW denotes the transient hot-wire method.

Table 3.3    Thermal conductivity data of silver nanostructure-enhanced phase change materials in the solid state as measured by the authors of the published journal papers

| Zeng et al. (2010) | | Parameshwaran, Jayavel and Kalaiselvam (2013) | | Parameshwaran, Dhamodharan, and Kalaiselvam (2013) | | Parameshwaran et al. (2014) | |
|---|---|---|---|---|---|---|---|
| Instrument | TPS | Instrument | LFA[1] | Instrument | LFA | Instrument | LFA |
| Ag NW[2] wt% | k (W/mK) | Ag NP[3] wt% | k (W/mK) | $AgTiO_2$ wt% | K (W/mK) | $AgTiO_2$ wt% | k (W/mK) |
| 0 | 0.3193 | 0 | 0.257 | 0 | 0.3633 | 0 | 0.2543 |
| 0.0909 | 0.393 | 0.1 | 0.284 | 0.08 | 0.3844 | 0.1 | 0.2830 |
| 0.2308 | 0.392 | 0.5 | 0.335 | 0.15 | 0.4071 | 0.5 | 0.3466 |
| 0.3758 | 0.355 | 1 | 0.447 | 0.3 | 0.4857 | 0.8 | 0.4214 |
| 0.4608 | 0.344 | 2 | 0.596 | 0.7 | 0.6235 | 1 | 0.4913 |
| 0.6273 | 0.341 | 5 | 0.765 | 1 | 0.8617 | 1.5 | 0.5379 |

[1] LFA denotes laser flash analyzer.
[2] NW denotes nanowires.
[3] NP denotes nanoparticles.

Table 3.4    Thermal conductivity (W/mK) data of the solid pure eicosane disks prepared following the ambient temperature solidification route versus the number of turns of the adjustable screw on top of the support set up; Reported values are the average of three measurements (maximum standard deviation of 1.5%) (Nabil, 2013)

| Number of Turns of the Screw | $T$=10 °C | $T$=20 °C | $T$=30 °C |
|---|---|---|---|
| 0 | 0.3641 | 0.3732 | 0.3605 |
| 0.25 | 0.4134 | 0.4112 | 0.4128 |
| 0.5 | 0.4215 | 0.4228 | 0.4237 |
| 0.75 | 0.4216 | 0.4224 | 0.4234 |
| 1 | 0.4217 | 0.4228 | 0.4235 |
| 1.25 | 0.4216 | 0.4229 | 0.4226 |

Table 3.5    Specifications, range of applicability and accuracy of the TPS500 and the

FP84HT instruments

| Transient Plane Source Apparatus TPS500 | | Differential Scanning Calorimetry Apparatus FP84HT | |
|---|---|---|---|
| Materials | Solids, medium- to high-viscosity liquids, and small particles/powders | Temperature range (normal operation): | RT ... 375 °C |
| Thermal Conductivity (W/mK) | 0.005 ... 500 | Temperature range (with cooling): | -60 ... 375 °C |
| Thermal Diffusivity (mm²/sec) | 0.02 ... 40 | Accuracy of hot stage temperature (-60 ... -20 °C): | ± 0.8 °C |
| Specific Heat (MJ/m³K) | 0.1 ... 4.5 | Accuracy of hot stage temperature (-20 ... 100 °C): | ± 0.4 °C |
| Measurement Time (sec) | 2.5 ... 640 | Accuracy of hot stage temperature (100 ... 200 °C): | ± 0.6 °C |
| Reproducibility | Thermal Conductivity ±2% Thermal Diffusivity ±5% Specific Heat ±7% | Accuracy of hot stage temperature (200 ... 300 °C): | ± 0.8 °C |

Table 3.6    Experimental and theoretical heat of fusion and melting point data of the solid pure eicosane and Ag/eicosane composites, prepared at room temperature, obtained by Differential Scanning Calorimetry (DSC) using the ramping rate of 5 $^{o}$C/min (densities of eicosane and silver used were   840   and 10,500 kg/m$^3$, respectively)

| Ag (wt%) (vol%) | Effective Densities of PCM Composites (kg/m$^3$), Eq. (3.5) | Theoretical Heat of Fusion (J/g), Eq. (3.4) | Experimental Heat of Fusion (J/g) | Theoretical Melting Point ($^o$C), Noggle (1989) | Experimental Melting Point ($^o$C) |
|---|---|---|---|---|---|
| 0 wt% 0 vol% | 840 | 247.5 | 241 | 36.4 | 37 |
| 1 wt% 0.081 vol% | 847.8 | 245 | 229 | 35.9 | 36.8 |
| 2 wt% 0.163 vol% | 855.7 | 242.6 | 208 | 35.66 | 36.5 |
| 3.5 wt% 0.289 vol% | 867.9 | 238.8 | 192 | 35.1 | 35.9 |
| 5 wt% 0.419 vol% | 880.5 | 235.1 | 177 | 34.54 | 35.5 |
| 6.5 wt% 0.553 vol% | 893.4 | 231.4 | 147 | 33.98 | 35.1 |
| 8 wt% 0.691 vol% | 906.7 | 227.7 | 134 | 33.42 | 34.5 |
| 10 wt% 0.881 vol% | 925.11 | 222.8 | 78.3 | 32.68 | 33.5 |

Table 3.7    Thermal conductivity (W/mK) data of the solid pure eicosane and Ag/eicosane composites prepared following the ice-water bath solidification route; Reported values are the average of three measurements (maximum standard deviation of 1.3%)

| Temperature (°C) | Pure | 1 wt% 0.081 vol% | 2 wt% 0.163 vol% | 3.5 wt% 0.289 vol% | 5 wt% 0.419 vol% | 6.5 wt% 0.553 vol% | 8 wt% 0.691 vol% | 10 wt% 0.881 vol% |
|---|---|---|---|---|---|---|---|---|
| 10 | 0.4069 | 0.4155 | 0.4417 | 0.4227 | 0.4194 | 0.4264 | 0.4554 | 0.4606 |
| 15 | 0.4025 | 0.4159 | 0.4374 | 0.4214 | 0.4136 | 0.4273 | 0.4578 | 0.4726 |
| 20 | 0.4011 | 0.4160 | 0.4342 | 0.4281 | 0.4162 | 0.4324 | 0.4583 | 0.4777 |
| 25 | 0.4041 | 0.4258 | 0.4442 | 0.4324 | 0.4259 | 0.4496 | 0.4691 | 0.4794 |
| 30 | 0.4007 | 0.4396 | 0.4951 | 0.4798 | 0.4365 | 0.4601 | 0.5057 | 0.5152 |
| 31 | 0.4052 | 0.4851 | 0.5183 | 0.4829 | 0.4681 | 0.4906 | 0.5361 | 0.5481 |
| 32 | 0.4068 | 0.4813 | 0.54 | 0.5023 | 0.4877 | 0.5154 | 0.8219 | 0.8319 |
| 33 | 0.4198 | 0.5039 | 0.5535 | 0.8017 | 0.7801 | 0.8072 | N/A | N/A |
| 34 | 0.4213 | 0.5176 | 0.8192 | N/A | N/A | N/A | N/A | N/A |
| 35 | 0.5789 | 0.7732 | N/A | N/A | N/A | N/A | N/A | N/A |

Table 3.8    Thermal conductivity (W/mK) data of the solid pure eicosane and Ag/eicosane composites prepared following the oven solidification route; Reported values are the average of three measurements (maximum standard deviation of 1.3%)

| Temperature (°C) | Pure | 1 wt% 0.081 vol% | 2 wt% 0.163 vol% | 3.5 wt% 0.289 vol% | 5 wt% 0.419 vol% | 6.5 wt% 0.553 vol% | 8 wt% 0.691 vol% | 10 wt% 0.881 vol% |
|---|---|---|---|---|---|---|---|---|
| 10 | 0.4502 | 0.4551 | 0.4788 | 0.471 | 0.4554 | 0.4629 | 0.4834 | 0.5032 |
| 15 | 0.4546 | 0.4596 | 0.4795 | 0.4754 | 0.4641 | 0.4756 | 0.4919 | 0.5111 |
| 20 | 0.4554 | 0.4717 | 0.4854 | 0.4741 | 0.4693 | 0.4731 | 0.5001 | 0.5246 |
| 25 | 0.4522 | 0.4777 | 0.5092 | 0.4969 | 0.4873 | 0.4968 | 0.5129 | 0.534 |
| 30 | 0.4533 | 0.493 | 0.5357 | 0.5317 | 0.5274 | 0.5287 | 0.5466 | 0.5539 |
| 31 | 0.4546 | 0.4984 | 0.5503 | 0.5429 | 0.5252 | 0.5306 | 0.5732 | 0.5862 |
| 32 | 0.4522 | 0.5322 | 0.5639 | 0.5654 | 0.5567 | 0.5538 | 0.8671 | 0.8754 |
| 33 | 0.4551 | 0.5449 | 0.5751 | 0.8132 | 0.8124 | 0.816 | N/A | N/A |
| 34 | 0.4789 | 0.5652 | 0.8392 | N/A | N/A | N/A | N/A | N/A |
| 35 | 0.6228 | 0.7965 | N/A | N/A | N/A | N/A | N/A | N/A |

Table 3.9    Thermal conductivity (W/mK) data of the solid pure eicosane and Ag/eicosane composites prepared following the room temperature solidification route; Reported values are the average of three measurements (maximum standard deviation of 1.4%)

| Temperature (°C) | Pure | 1 wt% 0.081 vol% | 2 wt% 0.163 vol% | 3.5 wt% 0.289 vol% | 5 wt% 0.419 vol% | 6.5 wt% 0.553 vol% | 8 wt% 0.691 vol% | 10 wt% 0.881 vol% |
|---|---|---|---|---|---|---|---|---|
| 10 | 0.4223 | 0.4518 | 0.4718 | 0.4694 | 0.4523 | 0.4494 | 0.4723 | 0.4872 |
| 15 | 0.4236 | 0.4474 | 0.4785 | 0.4667 | 0.4552 | 0.4516 | 0.4821 | 0.4903 |
| 20 | 0.4245 | 0.4521 | 0.4816 | 0.4727 | 0.4638 | 0.4601 | 0.4852 | 0.4968 |
| 25 | 0.4233 | 0.4883 | 0.4965 | 0.4928 | 0.4750 | 0.4703 | 0.5021 | 0.5107 |
| 30 | 0.4241 | 0.4981 | 0.5324 | 0.5297 | 0.5008 | 0.4968 | 0.5353 | 0.5487 |
| 31 | 0.4266 | 0.4969 | 0.5457 | 0.5366 | 0.5086 | 0.5091 | 0.5504 | 0.5674 |
| 32 | 0.4227 | 0.4971 | 0.5440 | 0.5405 | 0.5191 | 0.5182 | 0.8445 | 0.8534 |
| 33 | 0.4488 | 0.4992 | 0.5472 | 0.8094 | 0.7877 | 0.7746 | N/A | N/A |
| 34 | 0.4526 | 0.5249 | 0.8250 | N/A | N/A | N/A | N/A | N/A |
| 35 | 0.5467 | 0.7795 | N/A | N/A | N/A | N/A | N/A | N/A |

Figure 3.1    Thermal conductivity values of pure eicosane samples in both liquid (right scale)

and solid (left scale) states taken from published journal papers
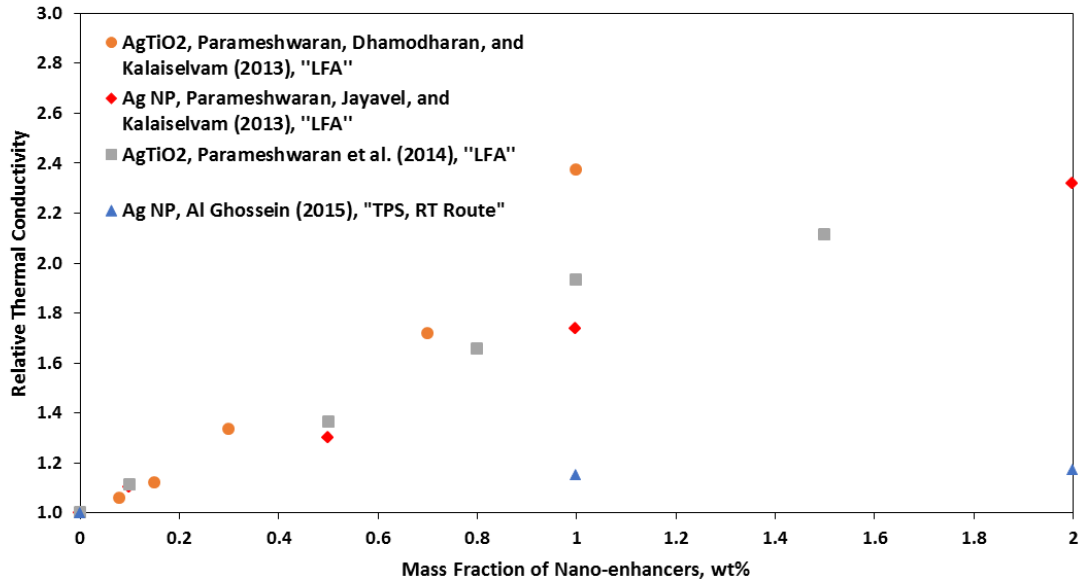
Figure 3.2    Thermal conductivity ratios of different types of silver-based nano-enhanced

phase change materials (NePCM) in solid state as a function of the mass fraction

of the silver nanostructures at room temperature
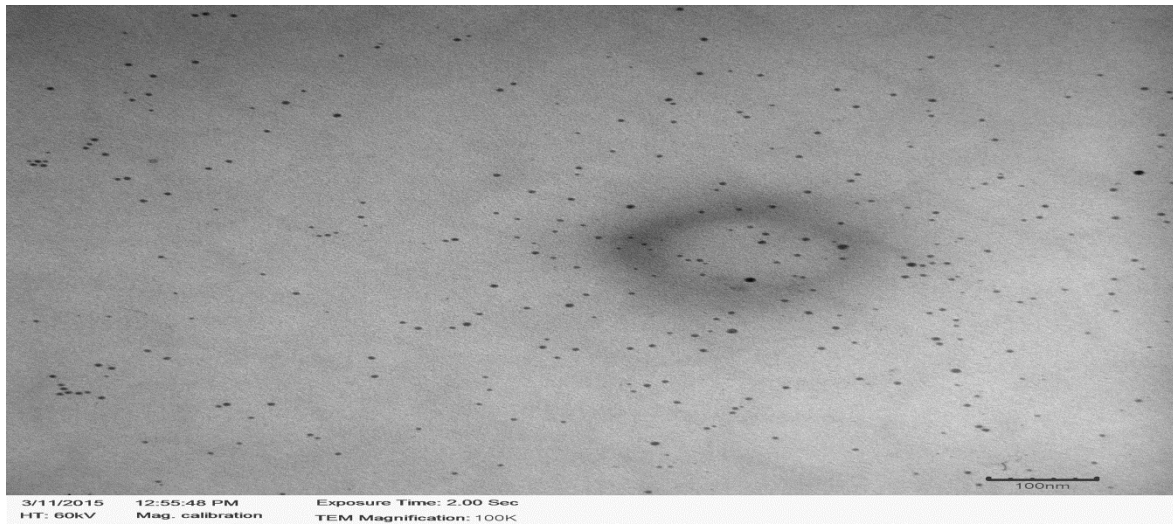
Figure 3.3    TEM image of the Ag nanoparticles (Hossain and Mills, 2015)
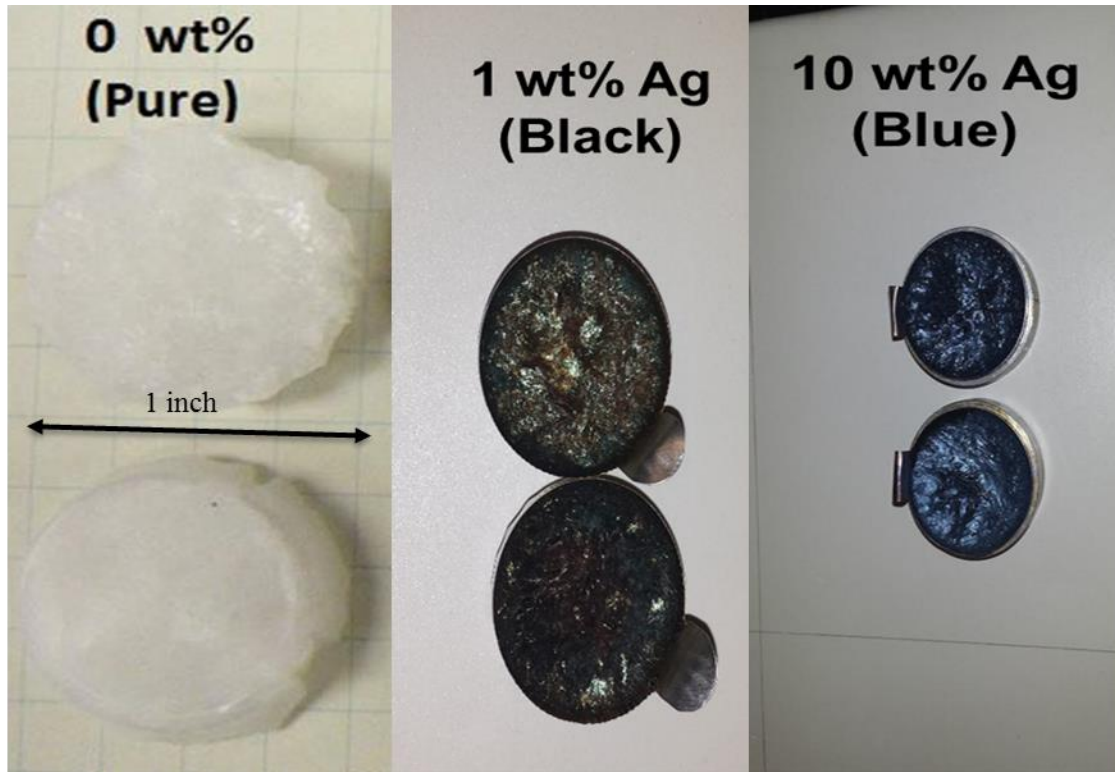
Figure 3.4    Photographs of pure eicosane (removed from the mold), 1 and 10 wt% of Ag/eicosane composites prepared following the room temperature solidification scheme
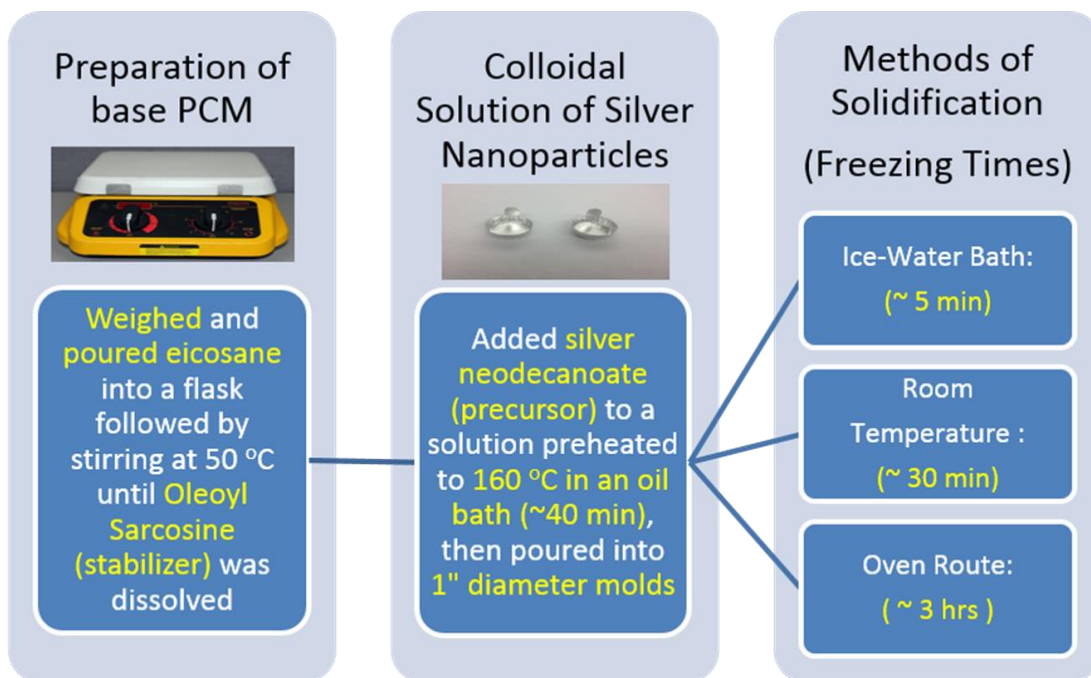
Figure 3.5    Overview diagram of the NePCM preparation protocols and three distinct solidification routes (Oleoyl Sarcosine and Silver Neodeconoate are $C_{21}H_{39}NO_3$ and $C_{10}H_{19}AgO_2$, respectively)
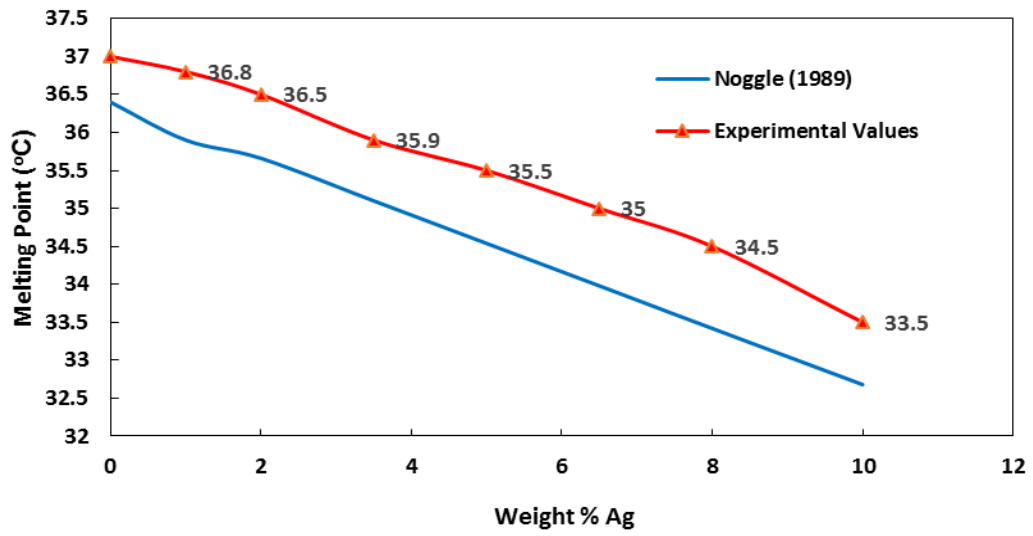
Figure 3.6    DSC-based and theoretical data (Noggle, 1989) of the phase change temperature of the pure eicosane and Ag/eicosane composites prepared following the room temperature solidification method (DSC ramping rate of 5 $^o$C/min)
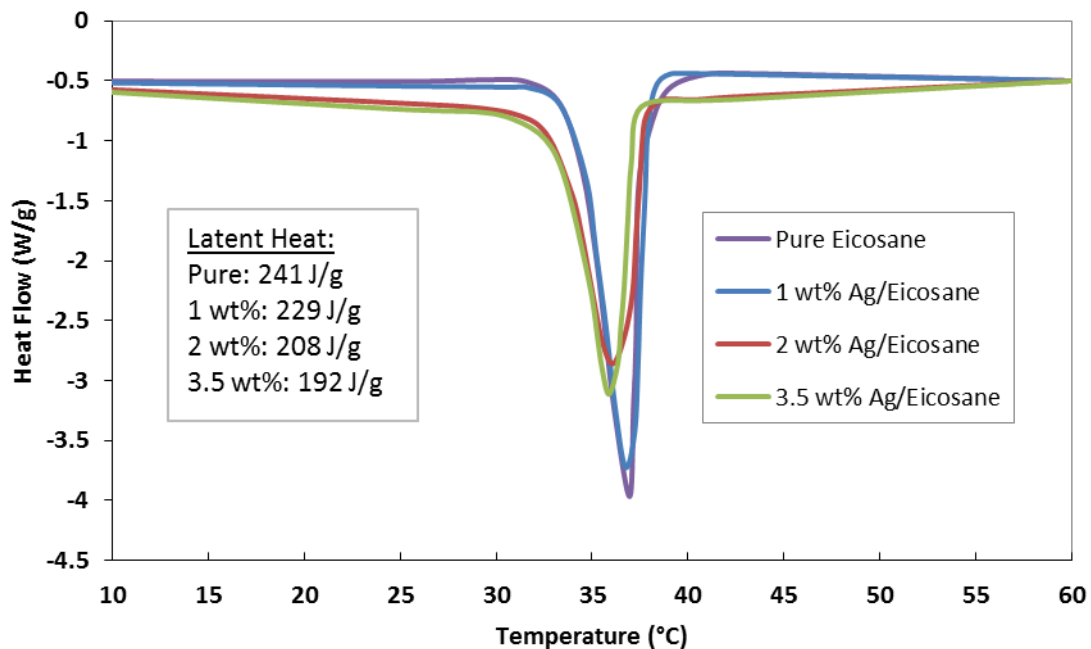
Figure 3.7    DSC curves of the exothermic reactions of pure eicosane and Ag/eicosane samples of 1, 2 and 3.5 wt% prepared following the room temperature solidification approach along with their respective heat of fusion values (DSC ramping rate of 5 $^{\circ}$C/min)
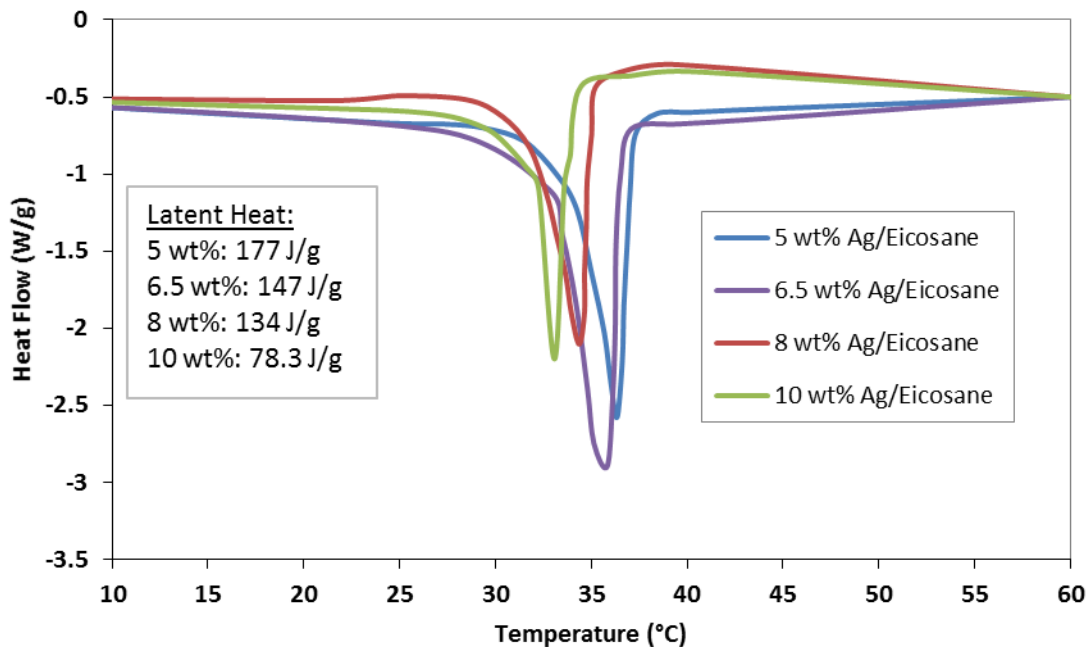
Figure 3.8      DSC curves of the exothermic reactions of 5, 6.5, 8 and 10 wt% Ag/eicosane samples prepared following the room temperature solidification method along with their respective heat of fusion values (DSC ramping rate of 5 $^o$C/min)

(a)



(c)



$$\alpha, \beta, \gamma \neq 90°$$

Triclinic Structure

$$\gamma = 120°$$

Hexagonal Structure
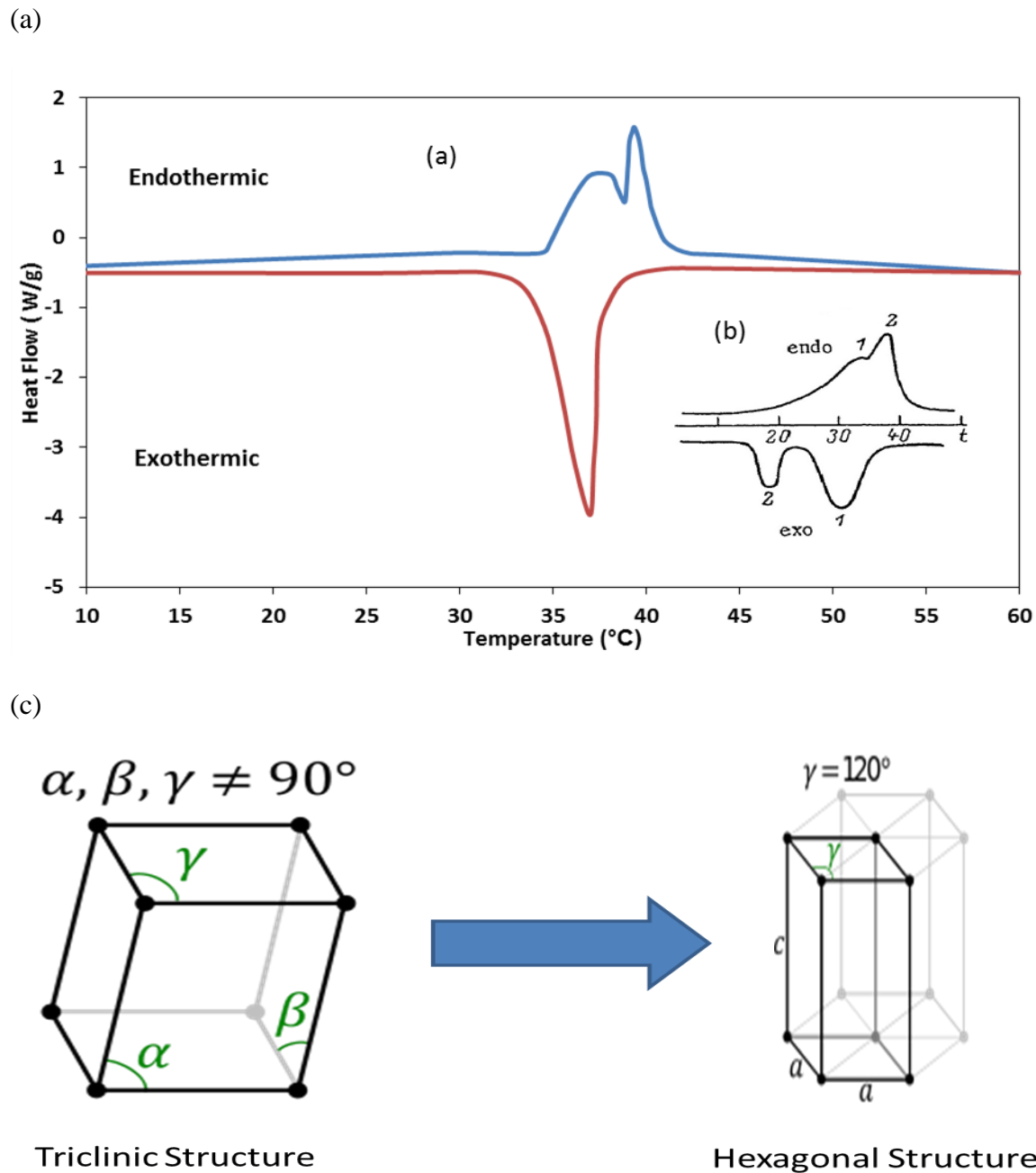
Figure 3.9    (a) DSC curves of the exothermic and endothermic reactions of pure eicosane of the present study prepared following the room temperature solidification route (DSC ramping rate of 5 °C/min) along with (b) an inset of the DSC curve from Kolesnikov and Syunyaev (1985) (DSC ramping rate of 1 °C/min) and (c) transition from triclinic to hexagonal structure (Kolesnikov and Syunyaev, 1985)
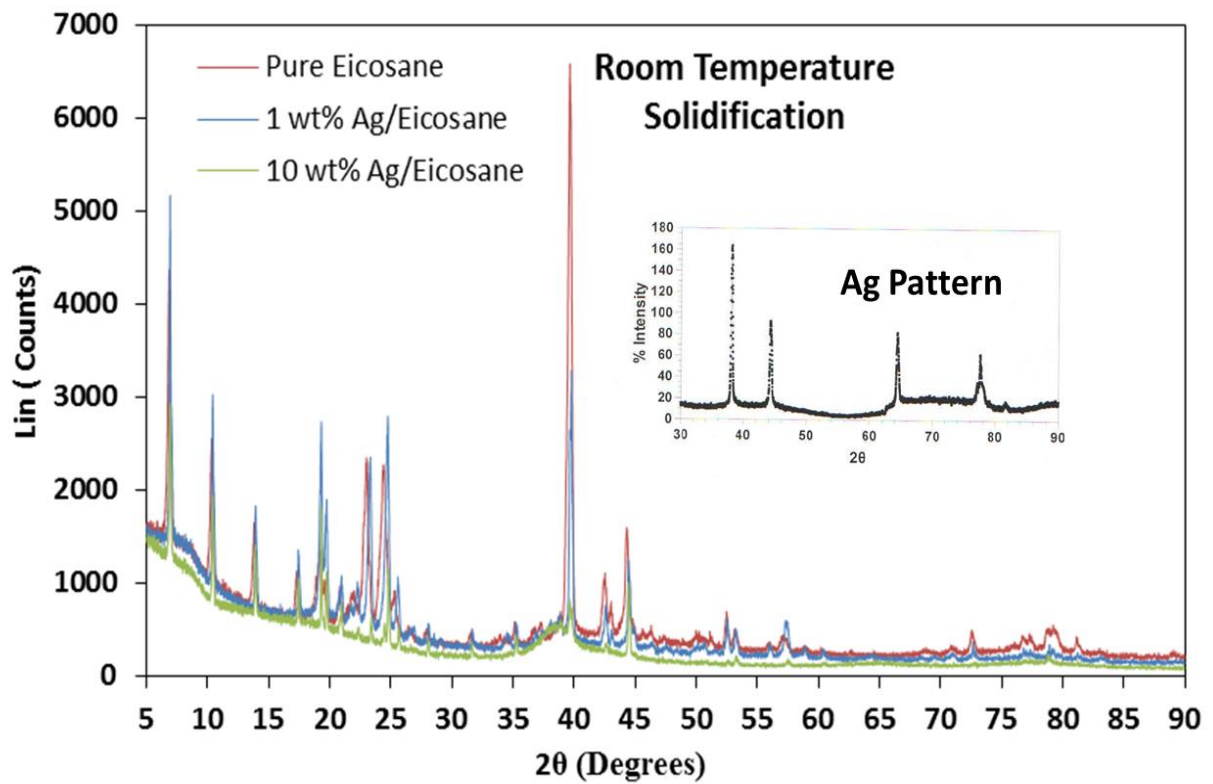
Figure 3.10    XRD patterns of pure eicosane, 1 and 10 wt% Ag/eicosane NePCM composites

prepared following the room temperature solidification route, along with an inset

of the XRD pattern of silver nanoparticles as prepared by Hossain and Mills

(2015)
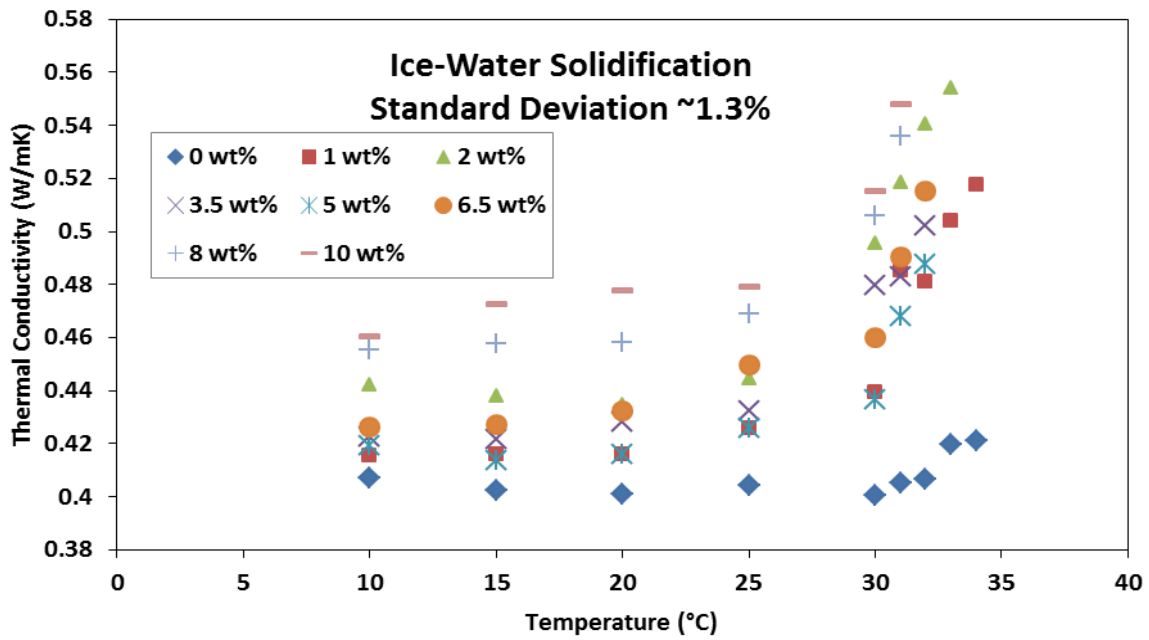
Figure 3.11    Thermal conductivity of the solid pure eicosane and Ag/eicosane samples prepared following the ice-water bath solidification route, excluding data close to the respective melting point of each NePCM
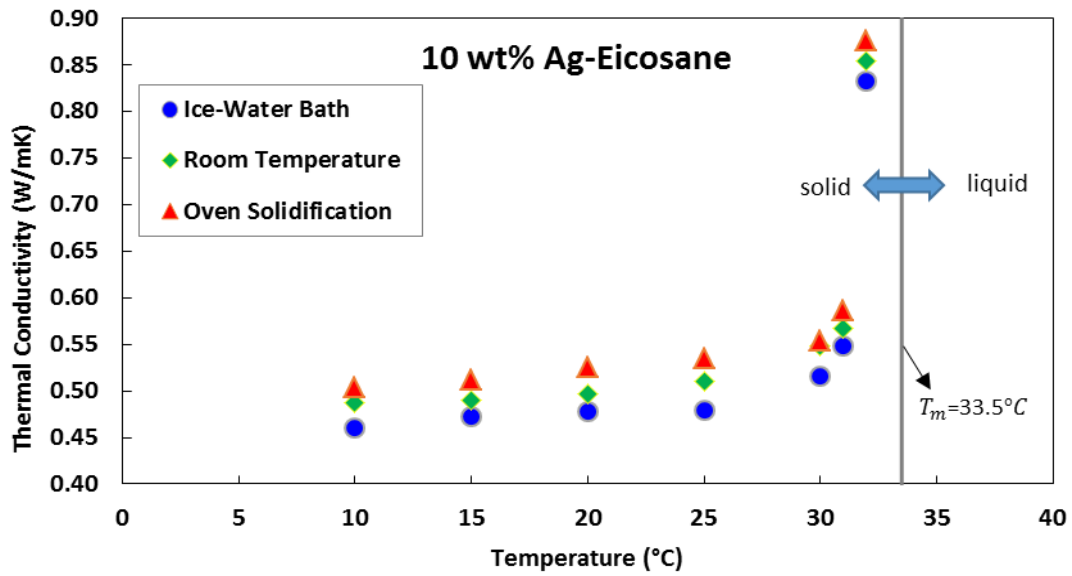
Figure 3.12    Comparison of the thermal conductivity of the 10 wt% Ag/eicosane samples prepared using three different solidification schemes (the stated melting temperature corresponds to the sample prepared following the room temperature route, Figure 3.6)
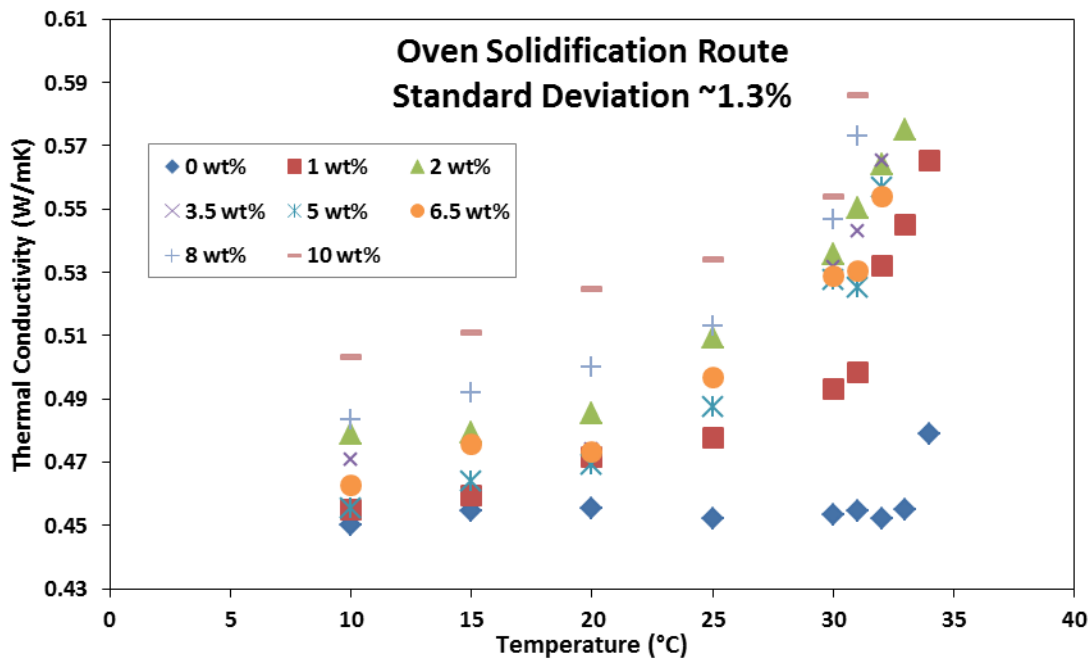
Figure 3.13    Thermal conductivity of the solid pure eicosane and Ag/eicosane samples prepared following the oven solidification route, excluding data close to the respective melting point of each NePCM
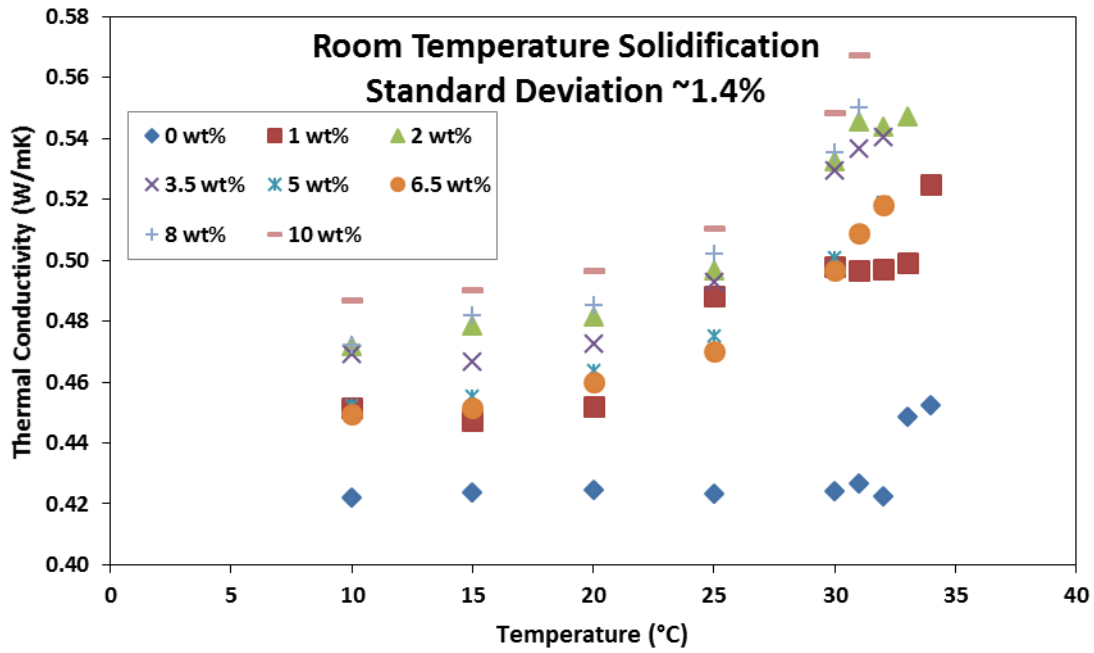
Figure 3.14    Thermal conductivity of the solid pure eicosane and Ag/eicosane samples prepared following the ambient temperature solidification route, excluding data close to the respective melting point of each NePCM
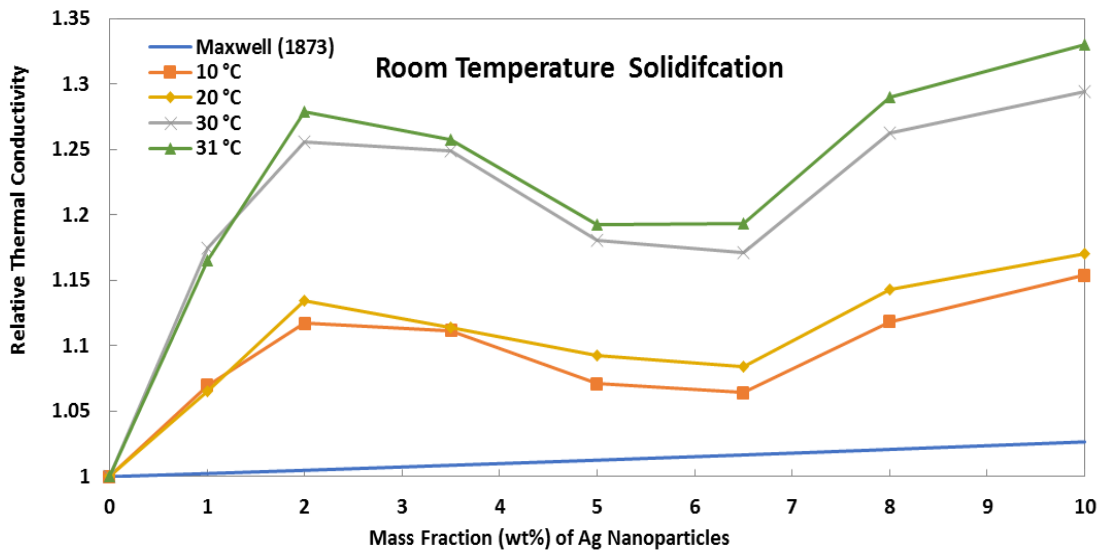
Figure 3.15    Relative thermal conductivity of the Ag/eicosane NePCM samples obtained following the room temperature solidification method along with the predictions of Maxwell's equation (1873)
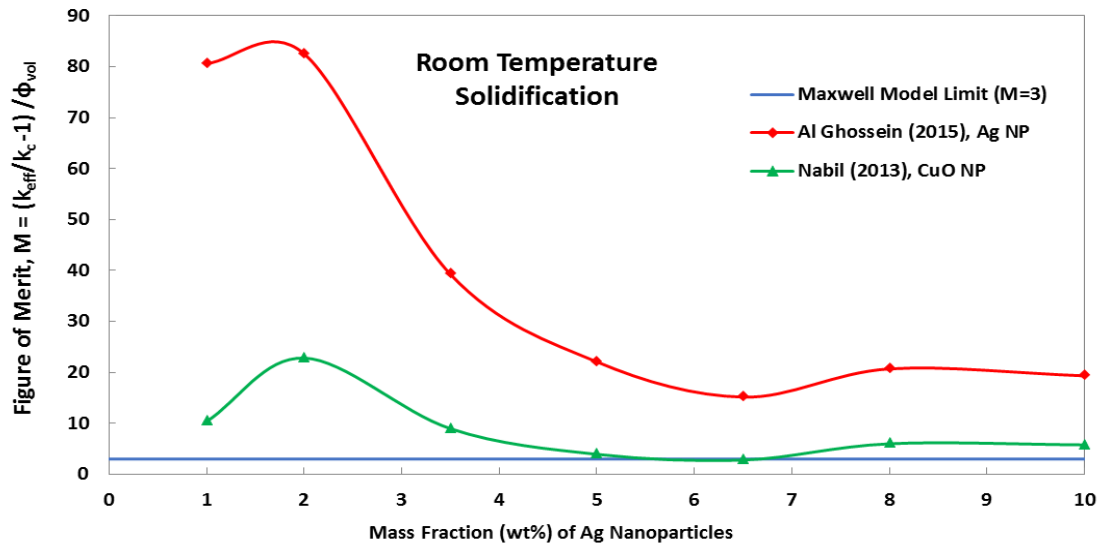
Figure 3.16    Comparison of the figure of merit between the present study (Ag nanofillers) and that of CuO nanoadditives of Nabil (2013) for NePCM composites prepared following the room temperature solidification route along with the limit of the Maxwell's Model (1873)

Chapter 4 Conclusions

Chapter 4 outlines the summary of this work pertinent to the previous three chapters and addresses recommendations for further progress of this research. The relevant conclusions are presented in numerical order as the following:

1)      Due to its high latent heat capacity, phase change materials (PCM), in this study paraffin, represents an adequate and widely-adopted choice for thermal energy storage applications. However, a low thermal conductivity of paraffin limits the ability and possibility to extract the stored latent heat within the PCM.

2)      Eicosane-based silver nanostructure-enhanced phase change materials (NePCM) colloids were prepared using silver (Ag) nanoparticles (5.5 nm in diameter) stabilized by Oleoyl Sarcosine ($C_{21}H_{39}NO_3$) for eight different weight fractions of nanoparticles (0, 1, 2, 3.5, 5, 6.5, 8 and 10 wt%). Desirable long-term stability of NePCM samples was achieved, and the liquid NePCM composites underwent three various methods of freezing: ice-water bath, room temperature and oven route.

3)      The Transient Plane Source (TPS) technique was utilized to measure the thermal conductivity of NePCM Ag/eicosane composites at different range of temperature, and results showed an increase in thermal conductivity as the temperature of the composites was raised.

4)      For all three methods of solidification, the highest thermal conductivity was measured at a loading of 10 wt% of silver nanoparticles. And when close to the melting point, a

sudden rise in thermal conductivity was observed for all NePCM samples, irrespective of the method of preparation.

5)      NePCM colloids prepared following the oven solidification method exhibited the highest thermal conductivity among the different routes, with the ice-water protocol consistently exhibiting the lowest thermal conductivity.

6)      Independent of the solidification routes and the samples' temperature, above a 2 wt% loading of nanostructures, a non-monotonic relation was observed between the weight fractions of the silver nanoparticles and the thermal conductivity of the NePCM composites.

7)      Differential Scanning Calorimetry (DSC) results showed a decrease in the latent heat capacity and phase change temperature, as the mass fractions of silver nanoparticles increased, due to the colligative properties of the composite.

8)      X-ray Diffraction (XRD) was also used to investigate the microstructure of the paraffin, and results illustrated the crystalline structure of eicosane.

Moving forward with this research, recommendations for interested researchers to examine and to verify the occurrence of some results are presented below:

1) Attempts could be carried out to investigate the marked rise in thermal conductivity close to melting point.

2) X-ray Diffraction tests at different temperature range of the NePCM samples could illustrate the change in crystal structure, which may have an effect on the thermal conductivity.

References

Abhat, A., 1983, "Low temperature latent heat thermal energy storage: heat storage materials," *Solar Energy*, 30, pp. 313-332.

Beck, A., 1957, "A steady state method for the rapid measurement of the thermal conductivity of rocks," *Journal of Scientific Instruments*, 34, pp. 186.

Bondi, A. A., 1962, "Thermal conductivity of nonassociated liquids," *American Institute of Chemical Engineers Journal,* 8, pp. 610.

Broadhurst, M. G., 1962, "An analysis of the solid phase behavior of the normal paraffins," *Journal of Research of the National Bureau of Standards Section A: Physics and Chemistry*, 66, pp. 241-249.

Cabeza, L. F. (Editor), 2014, *Advances in Thermal Energy Storage Systems: Methods and Applications (Woodhead Publishing Series in Energy)*, Woodhead Publishing, 612 pages.

Chen, Y. J., Nguyen, D. D., Shen, M. Y., Yip, M. C., and Tai, N. H., 2013, "Thermal characterizations of the graphite nanosheets reinforced paraffin phase-change composites," *Composites Part A: Applied Science and Manufacturing*, 44, pp. 40-46.

Chen, L., Zou, R., Xia, W., Liu, Z., Shang, Y., Zhu, J., Wang, Y., Lin, J., Xia, D. and Cao, A., 2012, "Electro-and photodriven phase change composites based on wax-infiltrated carbon nanotube sponges," *ACS nano*, 6, pp. 10884-10892.

Chintakrinda, K., Weinstein, R. D., and Fleischer, A. S., 2011, "A direct comparison of three different material enhancement methods on the transient thermal response of paraffin

phase change material exposed to high heat fluxes," *International Journal of Thermal Sciences*, 50, pp. 1639-1647.

Craig, S. R., Hastie, G. P., Roberts, K. J., and Sherwood, J. N., 1994, "Investigation into the structures of some normal alkanes within the homologous series $C_{13}H_{28}$ to $C_{60}H_{122}$ using high-resolution synchrotron X-ray powder diffraction," *Journal of Material Chemistry,* 4, pp. 977-981.

Darvin, J. R., Nabil, M., Uertz, J., and Mills, G., 2015, "Concentrated Ag colloids in dodecane relevant to nanostructure-enhanced PCM," *Submitted for publication to Chemistry of Materials*.

Das, S. K., Choi, S. U. S., Yu, W. and Pradeep, R., 2008, *Nanofluids: Science and Technology*, John Wiley & Sons, Inc., Hoboken, New Jersey.

Ehid, R., and Fleischer, A. S., 2012, "Development and characterization of paraffin-based shape stabilized energy storage materials," *Energy Conversion and Management*, 53, pp. 84-91.

Ehid, R., Weinstein, R. D., and Fleischer, A. S., 2012, "The shape stabilization of paraffin phase change material to reduce graphite nanofiber settling during the phase change process," *Energy Conversion and Management*, 57, pp. 60-67.

Fan, Liwu, 2011, Enhanced thermal conductivity and expedited freezing of nanoparticle suspensions utilized as novel phase change materials, PhD Thesis, Mechanical Engineering Department, Auburn University, Auburn, Alabama, USA, http://etd.auburn.edu/etd/bitstream/handle/10415/2707/Dissertation_Fan_0717.pdf?sequence=2.

Fan, L. W., Fang, X., Wang, X., Zeng, Y., Xiao, Y. Q., Yu, Z. T., Xu, X., Hu, Y. C., and Cen, K. F., 2013, "Effects of various carbon nanofillers on the thermal conductivity and energy

storage properties of paraffin-based nanocomposite phase change materials," *Applied Energy*, 110, pp. 163-172.

Fan, Liwu and Khodadadi, J. M., 2011, "Thermal conductivity enhancement of phase change materials for thermal energy storage: a review," *Renewable and Sustainable Energy Reviews*, 15, pp. 24-46.

Fang, X., Fan, L. W., Ding, Q., Wang, X., Yao, X. L., Hou, J. F., Yu, Z. T., Cheng, G. H., Hu, Y. C., and Cen, K. F., 2013, "Increased thermal conductivity of eicosane-based composite phase change materials in the presence of graphene nanoplatelets," *Energy & Fuels*, 27, pp. 4041-4047.

Fox, D. B., Sutter, D., and Tester, J. W., 2011, "The thermal spectrum of low-temperature energy use in the United States," *Energy & Environmental Science*, 4, pp. 3731-3740.

Frankfurt School – UNEP Collaborating Centre for Climate & Sustainable Energy Finance, 2015, "Global trends in renewable energy investment," http://www.fs-unep-centre.org (Frankfurt am Main).

Freund, M., Csikos, R., Keszthelyi, S. and Mozes, GY., 1982, *Paraffin Products: Properties, technologies, applications,* ed. GY. Mozes, Elsevier Scientific Publishing Company, Amsterdam-Oxford-New York, Chapters 1 and 3.

Griggs, E. I., and Yarbrough, D. W., 1978, "Thermal conductivity of solid unbranched alkanes from n-hexadecane to n-eicosane," in *Proceedings of the Southeastern Seminar on Thermal Sciences,* North Carolina State University, Raleigh, pp. 256-257.

Gur, I., Sawyer, K., and Prasher, R., 2012, "Searching for a better thermal battery," *Science*, 335, pp. 1454-1455.

Harikrishnan, S., Magesh, S., and Kalaiselvam, S., 2013, "Preparation and thermal energy storage behaviour of stearic acid–$TiO_2$ nanofluids as a phase change material for solar heating systems," *Thermochimica Acta*, 565, pp. 137-145.

He, Q., Wang, S., Tong, M., and Liu, Y., 2012, "Experimental study on thermophysical properties of nanofluids as phase-change material (PCM) in low temperature cool storage," *Energy Conversion and Management*, 64, pp. 199-205.

Ho, C. J., and Gao, J. Y., 2013, "An experimental study on melting heat transfer of paraffin dispersed with $Al_2O_3$ nanoparticles in a vertical enclosure," *International Journal of Heat and Mass Transfer*, 62, pp. 2-8.

Hossain, M. S., and Mills, G., 2015, *Department of Chemistry, Auburn University*, Private Communication.

Hot Disk, 2009, "Instruction Manual Hot Disk 6.0," *ThermTest Incorporation*, Fredericton, New Brunswick, CANADA, Chapters 6 & 9.

Ji, P., Sun, H., Zhong, Y., and Feng, W., 2012, "Improvement of the thermal conductivity of a phase change material by the functionalized carbon nanotubes," *Chemical Engineering Science*, 81, pp. 140-145.

Jia, L., Chen, Y., and Mo, S., 2013, "Solid–liquid phase transition of nanofluids," *International Journal of Heat and Mass Transfer*, 59, pp. 29-34.

Ju, S. P., Haung, T. J., Liao, C. H., and Chang, J. W., 2013, "Investigation of thermal conductivity of graphite flake/poly (p-phenylene sulfide) composite by experimental measurement and non-equilibrium molecular dynamics simulation," *Polymer*, 54, pp. 4702-4709.

Karunamurthy, K., Murugumohankumar, K., and Suresh, S., 2012, "Use of CuO nano-material for the improvement of thermal conductivity and performance of low temperature energy storage system of solar pond," *Digest Journal of Nanomaterials and Biostructures,* 7, pp. 1833-1841.

Khodadadi, J. M., Fan, Liwu, and Babaei, H., 2013, "Thermal conductivity enhancement of nanostructure-based colloidal suspensions utilized as phase change materials for thermal energy storage: A Review," *Renewable and Sustainable Energy Reviews*, 24, pp. 418-444.

Khodadadi, J. M. and Hosseinizadeh, S. F., 2007, "Nanoparticle-enhanced phase change materials (NEPCM) with great potential for improved thermal energy storage," *International Communications in Heat and Mass Transfer*, 34, pp. 534-543.

Kline, S. J., and McClintock, F., 1953, "Describing uncertainties in single-sample experiments", *Mechanical Engineering*, 75, pp. 3-8.

Kolesnikov, S. I. and Syunyaev, Z. I., 1985, "Phase transitions in the melting and crystallization of n-$C_{18}H_{38}$ and n-$C_{20}H_{42}$," *Journal of Applied Chemistry of the USSR,* 58, 10, pp. 2097-2101.

Li, H., Jiang, M., Li, Q., Li, D., Chen, Z., Hu, W., Huang, J., Xu, X., Dong, L., Xie, H. and Xiong, C., 2013, "Aqueous preparation of polyethylene glycol/sulfonated graphene phase change composite with enhanced thermal performance," *Energy Conversion and Management*, 75, pp. 482-487.

Li, M., 2013, "A nano-graphite/paraffin phase change material with high thermal conductivity," *Applied Energy*, 106, pp. 25-30.

Lide, D., 2005, CRC Handbook of Chemistry and Physics, Internet Version 2005, <http://www.hbcpnetbase.com>, CRC Press, Boca Raton, FL, pp. 12.219-12.220.

Lin, W., Zhang, R., and Wong, C. P., 2010, "Modeling of thermal conductivity of graphite nanosheet composites," *Journal of Electronic Materials,* 39, pp. 268−272.

Liu, Z., Zou, R., Lin, Z., Gui, X., Chen, R., Lin, J., Shang, Y., and Cao, A., 2013, "Tailoring carbon nanotube density for modulating electro-to-heat conversion in phase change composites," *Nano Letters*, 13, pp. 4028-4035.

Ma, B., Li, J., Peng, Z., and Ding, Yi, 2012, "Paraffin based composite phase change materials for thermal energy storage: thermal conductivity enhancement," (in Chinese), *Energy Storage Science and Technology,* 1, pp. 131-138.

Mehling, H. and Cabeza, L. F., 2008, *Heat and Cold Storage with PCM: An up to date introduction into basics and applications (Heat and Mass Transfer)*, Springer, Berlin, Chapter 3.

Mei, D., Zhang, B., Liu, R., Zhang, Y., and Liu, J., 2011, "Preparation of capric acid/halloysite nanotube composite as form-stable phase change material for thermal energy storage," *Solar Energy Materials and Solar Cells*, 95, pp. 2772-2777.

Meng, X., Zhang, H., Sun, L., Xu, F., Jiao, Q., Zhao, Z., Zhang, J., Zhou, H., Sawada, Y., and Liu, Y., 2013, "Preparation and thermal properties of fatty acids/CNTs composite as shape-stabilized phase change materials," *Journal of Thermal Analysis and Calorimetry*, 111, pp. 377-384.

Müller, A., and Lonsdale, K., 1948, "The low-temperature form of $C_{18}H_{38}$," *Acta Crystallographica*, 1, pp. 129-131.

Murshed, S. M. S., Leong, K. C., and Yang, C., 2005, "Enhanced thermal conductivity of $TiO_2$ water based nanofluids," *International Journal of Thermal Sciences*, 44, pp. 367-373.

Nabil, M., 2013, Thermal conductivity of nanostructure-enhanced phase change materials: measurements for solid eicosane-based copper oxide and carbon nanotube colloids and numerical modeling of anomalous measurements near phase transition, M.Sc. Thesis, Mechanical Engineering Department, Auburn University, Alabama, USA, http://etd.auburn.edu/etd/handle/10415/3672.

Nabil, M. and Khodadadi, J. M., 2013, "Experimental determination of temperature-dependent thermal conductivity of solid eicosane-based nanostructure-enhanced phase change materials," *International Journal of Heat and Mass Transfer*, 67, pp. 301-310.

Nagasa, Y. and Nagashima, A., 1981, "Absolute measurement of the thermal conductivity of electrically conducting liquids by the transient hot-wire method*," Journal of Physics E: Scientific Instruments,* 14, pp. 1435.

Noggle, J. H., 1989, *Physical Chemistry*, second ed., Harper Collins, United States of America, Chapter 7.

Nyburg, S. C., and Gerson, A. R., 1992, "Crystallography of the even n-alkanes: structure of $C_{20}H_{42}$," *Acta Crystallographica. Section B: Structural Crystallography and Crystal Chemistry*, 48, pp. 103-106.

Nyburg, S. C., and Potworowski, J. A., 1973, "Prediction of unit cells and atomic coordinates for the n-alkanes," *Acta Crystallographica Section B: Structural Crystallography and Crystal Chemistry*, 29, pp. 347-352.

Parameshwaran, R., Deepak, K., Saravanan, R., and Kalaiselvam, S., 2014, "Preparation, thermal and rheological properties of hybrid nanocomposite phase change material for thermal energy storage," *Applied Energy*, 115, pp. 320-330.

Parameshwaran, R., Dhamodharan, P., and Kalaiselvam, S., 2013, "Study on thermal storage properties of hybrid nanocomposite-dibasic ester as phase change material," *Thermochimica Acta*, 573, pp. 106-120.

Parameshwaran, R., Jayavel, R., and Kalaiselvam, S., 2013, "Study on thermal properties of organic ester phase-change material embedded with silver nanoparticles," *Journal of Thermal Analysis and Calorimetry*, 114, pp. 845-858.

Parameshwaran, R., and Kalaiselvam, S., 2013, "Energy efficient hybrid nanocomposite-based cool thermal storage air conditioning system for sustainable buildings," *Energy*, 59, pp. 194-214.

Parker, W. J., Jenkins, R. J., Butler, C. P., and Abbott, G. L., 1961, "Flash method of determining thermal diffusivity, heat capacity, and thermal conductivity," *Journal of Applied Physics*, 32, pp. 1679-1684.

Pielichowska, K., and Pielichowski, K., 2014, "Phase change materials for thermal energy storage," *Progress in Materials Science*, 65, pp. 67-123.

Piper, S. H., and Malkin, T., 1930, "Crystal structure of normal paraffins," *Nature*, 126, pp. 278.

Rastorguev, Y. L., Bogatov, G. F., and Grigor'ev, B. A., 1974, "Thermal conductivity of higher n-alkanes," *Chemistry and Technology of Fuels and Oils*, 10, pp. 728-732.

Rathod, M. K. and Banerjee J., 2013, "Thermal stability of phase change materials use in latent heat energy storage systems: A review," *Renewable and Sustainable Energy Reviews,* 18, pp. 246-258.

Rohatgi, A., 2015, Web Plot Digitizer: HTML5 based online tool to extract numerical data from plot images, Version 3.8,  http:// arohatgi.info/WebPlotDigitizer/app/

Sanusi, O., Fleischer, A., and Weinstein, R., 2010, "An investigation into the solidification of nano-enhanced phase change material for transient thermal management of electronics," *Thermal and Thermomechanical Phenomena in Electronic Systems (ITherm), 2010 12th IEEE Intersociety Conference,* pp. 1-6.

Stryker, P. C., and Sparrow, E. M., 1990, "Application of a spherical thermal conductivity cell to solid n-eicosane paraffin," *International Journal of Heat and Mass Transfer*, 33, pp. 1781-1793.

U.S. Energy Information Administration, *Monthly Energy Review*, Tables 1.3 and 10.1 (March 2015), preliminary data.

Vélez, C., Khayet, M., and de Zárate, J. O., 2015, "Temperature-dependent thermal properties of solid/liquid phase change even-numbered n-alkanes: n-hexadecane, n-octadecane and n-eicosane," *Applied Energy*, 143, pp. 383-394.

Wakeham, W. A., and Assael, M. J., 1999, "Thermal Conductivity Measurement," in *Mechanical Variables Measurement - Solid, Fluid, and Thermal,* edited by Webster, J. G., CRC Press, Chapter 14.

Wang, Y., Tang, B., and Zhang, S., 2013, "Single-walled carbon nanotube/phase change material composites: Sunlight-driven, reversible, form-stable phase transitions for solar thermal energy storage," *Advanced Functional Materials*, 23, pp. 4354-4360.

Warzoha, R. J., and Fleischer, A. S., 2014a, "Determining the thermal conductivity of liquids using the transient hot disk method. Part I: Establishing transient thermal-fluid constraints," *International Journal of Heat and Mass Transfer*, 71, pp. 779-789.

Warzoha, R. J., and Fleischer, A. S., 2014b, "Determining the thermal conductivity of liquids using the transient hot disk method. Part II: Establishing an accurate and repeatable experimental methodology," *International Journal of Heat and Mass Transfer*, 71, pp. 790-807.

Yarbrough, D. W., and Kuan, C. N., 1981, "The thermal conductivity of solid n-eicosane, n-octadecane, n-heptadecane, n-pentadecane, and n-tetradecane," in *Proceeding of the 17th International Thermal Conductivity Conference*, pp. 15-19.

Yaws, C. L., 2009, *Transport Properties of Chemicals and Hydrocarbons,* William Andrew, Norwich, New York, USA.

Ye, F., Ge, Z., Ding, Y., and Yang, J., 2014, "Multi-walled carbon nanotubes added to $Na_2CO_3$/MgO composites for thermal energy storage," *Particuology*, 15, pp. 56-60.

Zeng, J. L., Cao, Z., Yang, D. W., Sun, L. X., and Zhang, L, 2010, "Thermal conductivity enhancement of Ag nanowires on an organic phase change material," *Journal of Thermal Analysis and Calorimetry,* 101, pp. 385-389.

Zeng, Y., Fan, L. W., Xiao, Y. Q., Yu, Z. T., and Cen, K. F., 2013, "An experimental investigation of melting of nanoparticle-enhanced phase change materials (NePCMs) in a bottom-heated vertical cylindrical cavity," *International Journal of Heat and Mass Transfer*, 66, pp. 111-117.

Zhang, Q., and Liu, J., 2013, "Nano liquid metal as an emerging functional material in energy management, conversion and storage," *Nano Energy*, 2, pp. 863-872.

Zhang, L., Zhu, J., Zhou, W., Wang, J., and Wang, Y., 2012, "Thermal and electrical conductivity enhancement of graphite nanoplatelets on form-stable polyethylene

glycol/polymethyl methacrylate composite phase change materials," *Energy*, 39, pp. 294-302.

Zhong, Y., Zhou, M., Huang, F., Lin, T., and Wan, D., 2013, "Effect of graphene aerogel on thermal behavior of phase change materials for thermal management," *Solar Energy Materials and Solar Cells*, 113, pp. 195-200.

Zhou, M., Lin, T., Huang, F., Zhong, Y., Wang, Z., Tang, Y., Bi, H., Wan, D., and Lin, J., 2013, "Highly conductive porous graphene/ceramic composites for heat transfer and thermal energy storage," *Advanced Functional Materials*, 23, pp. 2263-2269.

Appendix A: Comparison of the Three Different Solidification Schemes


In Chapter 3, a comparison among the various methods of solidification (ice-water bath, room temperature, and oven solidification routes) for the 10 wt% loading of Ag silver nanoparticles in the NePCM composite was investigated and analyzed. In this appendix, the remaining figures for the other mass loadings of silver nanoparticles (0, 1, 2, 3.5, 5, 6.5 and 8 wt%) are presented (Figures A1-A7). Similar to Figure 3.12, the samples prepared following the oven solidification scheme exhibited the highest thermal conductivity values, while the ice-water bath samples exhibited the lowest values of thermal conductivity.
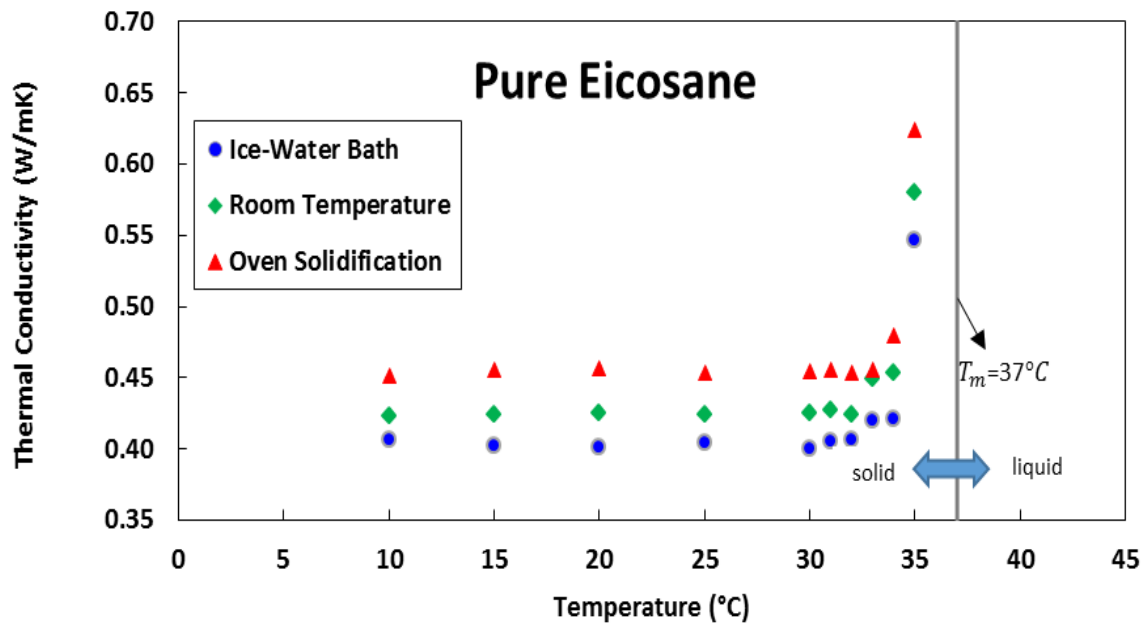
Figure A.1     Comparison of the thermal conductivity of the 0 wt% Ag/eicosane samples prepared using three different solidification schemes (the stated melting temperature corresponds to the sample prepared following the room temperature route, Figure 3.6)
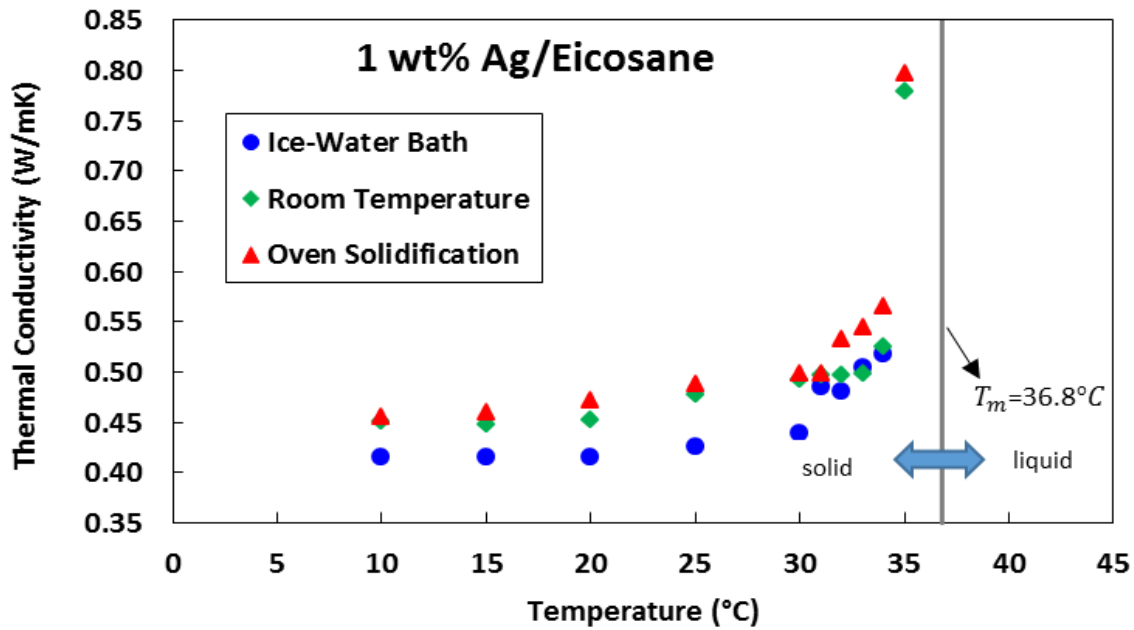
Figure A.2    Comparison of the thermal conductivity of the 1 wt% Ag/eicosane samples prepared using three different solidification schemes (the stated melting temperature corresponds to the sample prepared following the room temperature route, Figure 3.6)
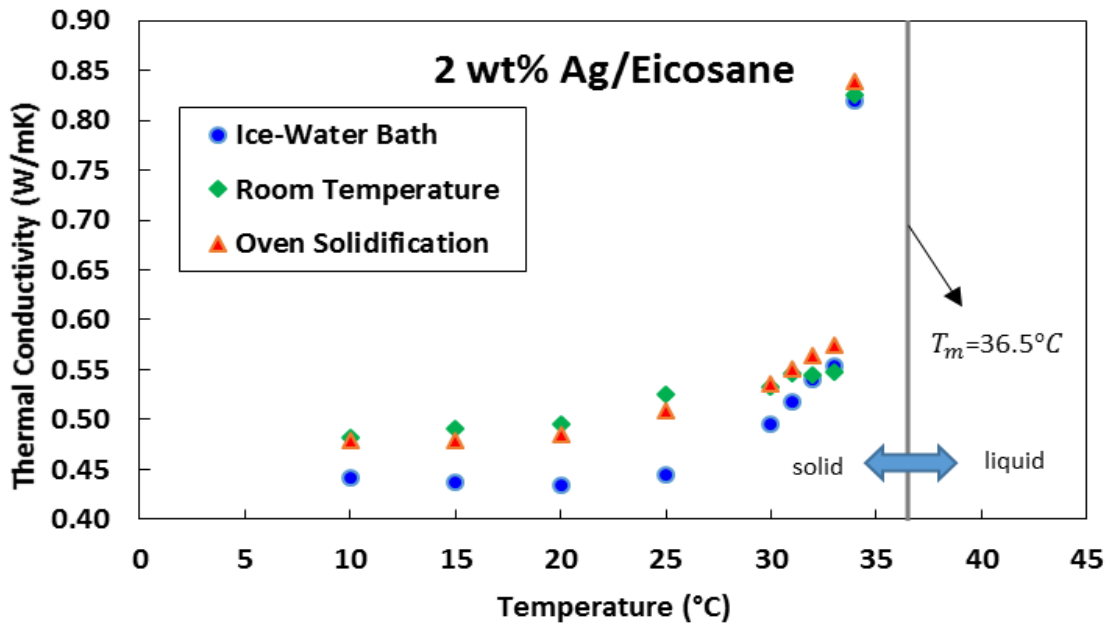
Figure A.3    Comparison of the thermal conductivity of the 2 wt% Ag/eicosane samples prepared using three different solidification schemes (the stated melting temperature corresponds to the sample prepared following the room temperature route, Figure 3.6)
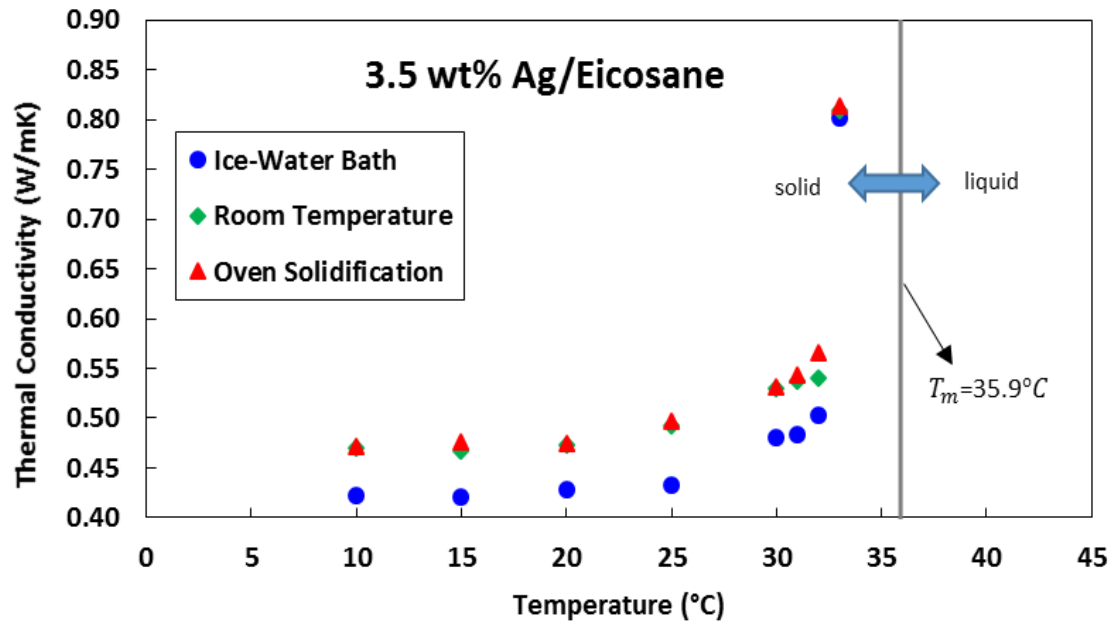
Figure A.4    Comparison of the thermal conductivity of the 3.5 wt% Ag/eicosane samples prepared using three different solidification schemes (the stated melting temperature corresponds to the sample prepared following the room temperature route, Figure 3.6)
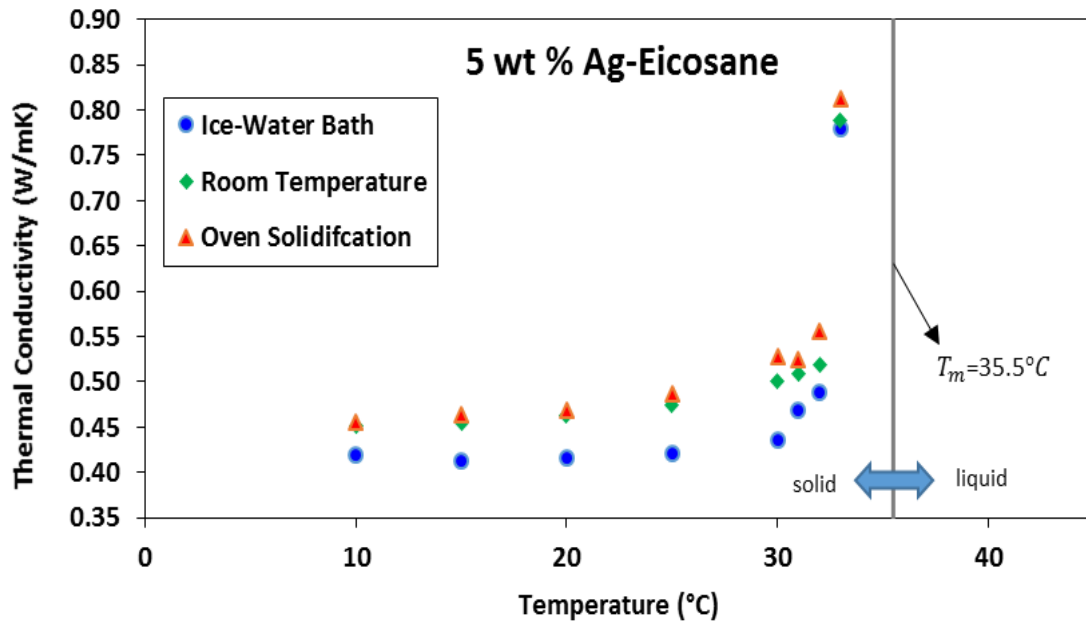
Figure A.5    Comparison of the thermal conductivity of the 5 wt% Ag/eicosane samples prepared using three different solidification schemes (the stated melting temperature corresponds to the sample prepared following the room temperature route, Figure 3.6)
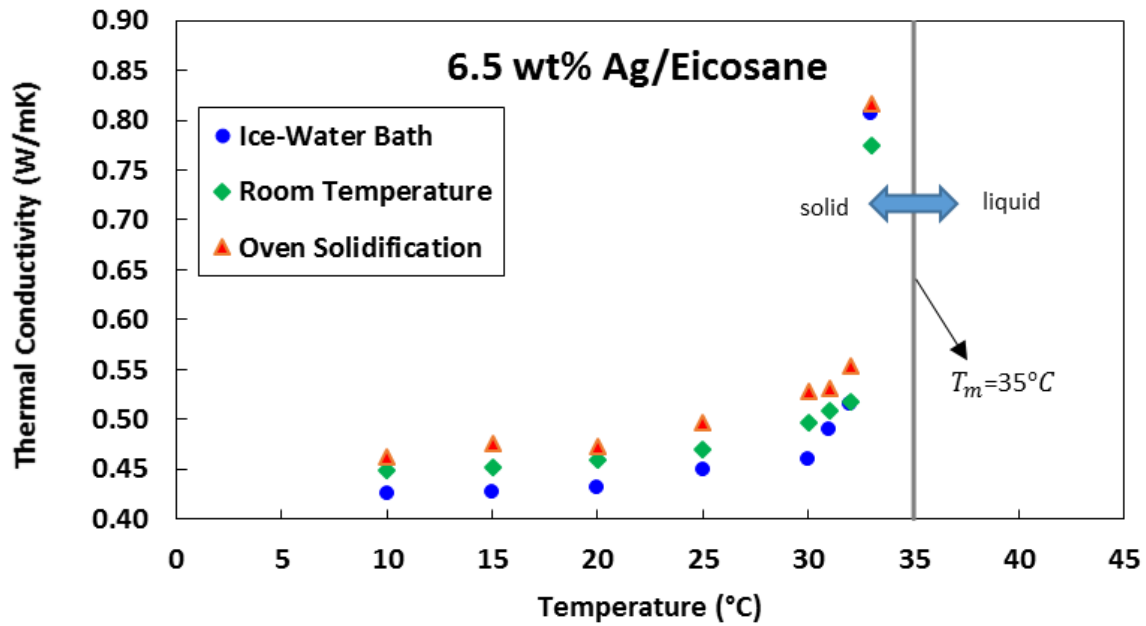
Figure A.6    Comparison of the thermal conductivity of the 6.5 wt% Ag/eicosane samples prepared using three different solidification schemes (the stated melting temperature corresponds to the sample prepared following the room temperature route, Figure 3.6)
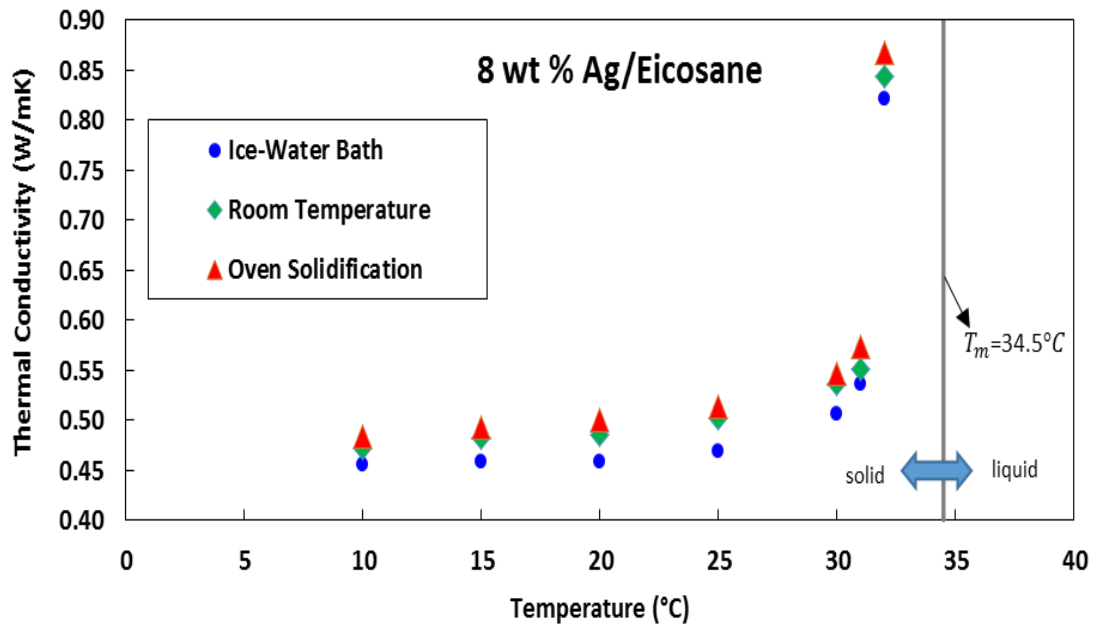
Figure A.7    Comparison of the thermal conductivity of the 8 wt% Ag/eicosane samples prepared using three different solidification schemes (the stated melting temperature corresponds to the sample prepared following the room temperature route, Figure 3.6)

Appendix B: Uncertainty Estimations of the Maxwell Model

In this appendix, the Maxwell model (1873) will be evaluated to determine the uncertainty of its predictions of thermal conductivity of composites by utilizing the Kline-McClintock method (1953). The aforementioned method has been widely used by researchers to determine the uncertainties associated with experimental measurements and will be discussed below.

## B.1 Kline-McClintock method (1953):

The equation of interest is that of equation (3.5), $k_{eff} = k_c \left[ \frac{k_d + 2k_c - 2\emptyset_{vol}(k_c - k_d)}{k_d + 2k_c + \emptyset_{vol}(k_c - k_d)} \right]$, where *eff, c, d*, and $\emptyset_{vol}$ stand for effective, continuous phase (eicosane), discrete phase (silver nanoadditives) and volume fraction of the silver nanoparticles, respectively. The quantity *k* stands for thermal conductivity (W/mK). The uncertainty of the continuous phase measurement was obtained from the manufacturer of the TPS instrument, which was 5% of the measured value, and is used throughout the estimations of this section. However, before applying the Kline-McClintock method to equation (3.5), the uncertainty of the volume fraction must be determined first. Equation (3.3), $\emptyset_{vol} = \frac{\emptyset_{wt}\rho_c}{\emptyset_{wt}\rho_c + (1 - \emptyset_{wt})\rho_d}$, was used to determine the uncertainty

of the volume fraction associated with uncertainty of the weight fraction of the nanoparticles. The uncertainty for the mass of the silver nanoparticles, which were measured using an Ohaus Pioneer Balance (Ohaus, New Jersey, USA) was $\pm0.0005$ g, and the densities of the materials utilized in this relation were assumed to be well-defined in the literature. Mathematically, the uncertainty of a quantity $R$ that depends on $n$ variables ($R = R(X_1, X_2, \ldots, X_n)$) is given by the Kline-McClintock equation:

$$\delta R = \left( \sum_{i=1}^{n} \left( \left( \frac{\partial R}{\partial X_i} \right)^2 (\delta X_i)^2 \right) \right)^{1/2} \tag{B.1}$$

Assuming zero uncertainties for densities of eicosane and silver, the uncertainties of the volume fraction (Equation 3.3) and the predicted effective thermal conductivity using the Maxwell model (Equation 3.5) are:

$$\delta\varnothing_{vol} = \left( \frac{\partial\varnothing_{vol}}{\partial\varnothing_{wt}} \right) (\delta\varnothing_{wt}) \tag{B.2}$$

$$\delta k_{eff} = \left[ \left( \frac{\partial k_{eff}}{\partial\varnothing_{vol}} * \delta\varnothing_{vol} \right)^2 + \left( \frac{\partial k_{eff}}{\partial k_c} * \delta k_c \right)^2 + \left( \frac{\partial k_{eff}}{\partial k_d} * \delta k_d \right)^2 \right]^{1/2} \tag{B.3}$$

Several cases of different uncertainties of thermal conductivity of the silver nanoparticles ($\delta k_d$) were investigated to determine its effect on the value of predicted thermal conductivity. Case 1 corresponds to an uncertainty of 0% ($\delta k_d = 0$), case 2 corresponds to an uncertainty of 1% ($\delta k_d = 0.01k_d$), and case 3 corresponds to an uncertainty of 5% ($\delta k_d = 0.05k_d$). It must be noted that the uncertainties of thermal conductivity of eicosane and volume fraction ($\delta k_c$ and $\delta\varnothing_{vol}$) were kept unchanged in all three cases. The partial derivatives and the equations were calculated using Wolfram Alpha (Standard Wolfram Alpha, http://www.wolframalpha.com/), and also verified independently. The results of the effective thermal conductivity (with and without uncertainty) for the various cases are tabulated in Table B.1, and are plotted in Figure B.1.

Results of equation (B.1) revealed an uncertainty of 5.0642% for the volume fraction, and as the mass fraction increased the uncertainty of the volume fraction decreased because of the inversely proportional relation between the mass fraction and the partial derivative $\left(\frac{\partial \emptyset_{vol}}{\partial \emptyset_{wt}}\right)$. As for the effective thermal conductivity, results showed an uncertainty of 5% for all the effective thermal conductivities (B.3) for case 1, which is also illustrated in the Figure B.1. The plot exhibits a linear increase in thermal conductivity as expected, with a variation of only 5%. The goal behind this case was to determine which of the two uncertainties ($\delta\emptyset_{wt}$ or $\delta k_c$) had the greater effect on the uncertainty of the effective thermal conductivity. When $\delta k_c$ was set to 0, results showed insignificant change in thermal conductivity values, a change of only 0.01219%, however, assuming perfect weighing accuracy of the silver nanoparticles, the change in effective thermal conductivity was, as expected, calculated to be 5%. As a result, more care should be taken in measuring the right thermal conductivity for the continuous phase. As for cases 2 and 3, the uncertainty of the value of the thermal conductivity of the silver nanoparticles has been introduced, 0.01 and 0.05, respectively. For case 2, results showed an additional 1.28% difference from case 1, a total of 6.28% variation from the ideal Maxwell model results. And, when the uncertainty was raised to 5%, a 19.62% difference was calculated for the third case, showing the importance of using the right value for thermal conductivity of silver nanoparticles and the effect it would have on the effective thermal conductivity of the NePCM composite.

Table B.1    Predicted effective and relative thermal conductivity values of pure eicosane and Ag/eicosane NePCM samples following the Maxwell model (1873) and the Kline-McClintock (1953) uncertainty method for three cases [Uncertainties of the densities are zero, whereas the uncertainty of thermal conductivity of eicosane is 5%; uncertainties of the thermal conductivity of silver nanoparticles are assumed to be 0, 1 and 5% for cases 1, 2 and 3, respectively].

| Ag (wt%) | Pure | 1 wt% | 2 wt% | 3.5 wt% | 5 wt% | 6.5 wt% | 8 wt% | 10 wt% |
|---|---|---|---|---|---|---|---|---|
| Volume Fraction (vol%) | | | | | | | | |
| Ideal | 0 | 0.0808 | 0.1631 | 0.2896 | 0.4197 | 0.5536 | 0.6915 | 0.8819 |
| Uncertainty Included | 0 | 0.0849 | 0.1673 | 0.2939 | 0.4241 | 0.5581 | 0.6962 | 0.8867 |
| Effective Thermal Conductivity (W/mK) | | | | | | | | |
| $k_{ideal}$ | 0.4233 | 0.4243 | 0.4254 | 0.4270 | 0.4286 | 0.4303 | 0.4321 | 0.4346 |
| Case 1 | 0.4445 | 0.4455 | 0.4466 | 0.4483 | 0.4501 | 0.4519 | 0.4537 | 0.4563 |
| Case 2 | 0.4445 | 0.451 | 0.4521 | 0.4538 | 0.4555 | 0.4573 | 0.4592 | 0.4618 |
| Case 3 | 0.445 | 0.5075 | 0.5087 | 0.5105 | 0.5124 | 0.5144 | 0.5164 | 0.5191 |
| Relative Thermal Conductivity | | | | | | | | |
| $k_{ideal}$ | 1 | 1.0024 | 1.0049 | 1.0087 | 1.0126 | 1.0167 | 1.0208 | 1.0266 |
| Case 1 | 1.05 | 1.0525 | 1.0551 | 1.0591 | 1.0632 | 1.0675 | 1.0719 | 1.0779 |
| Case 2 | 1.05 | 1.0654 | 1.0679 | 1.0719 | 1.0761 | 1.0803 | 1.0847 | 1.0908 |
| Case 3 | 1.05 | 1.1990 | 1.2018 | 1.2061 | 1.2105 | 1.2151 | 1.2199 | 1.2264 |
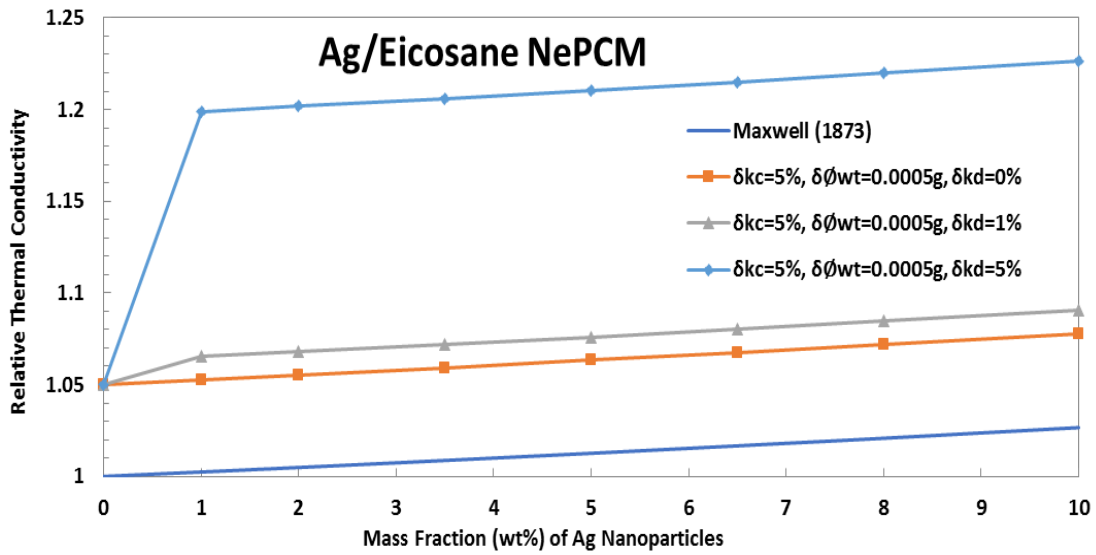
Figure B.1    Predicted relative thermal conductivity of the Ag/eicosane NePCM samples using the Maxwell's equation (1873) and the Kline-McClintock (1953) uncertainty method for three cases [Uncertainties of the densities are zero, whereas the uncertainty of thermal conductivity of eicosane is 5%; uncertainties of the thermal conductivity of silver nanoparticles are assumed to be 0, 1 and 5 for cases 1, 2 and 3, respectively].